Demonstration of Dense Mesoscopic Atomic Clouds in a Holographic Atom Trap

by

Jennifer S. Sebby

A dissertation submitted in partial fulfillment

of the requirements for the degree of

Doctor of Philosophy

(Physics)

at the

UNIVERSITY OF WISCONSIN-MADISON

2004

0.1 Abstract

This dissertation describes experiments involving the Holographic Atom Trap (HAT) (Newell *et al.*, 2003). The HAT is a novel far-off resonant optical trap formed by the interference of five Nd:YAG laser beams. At the intersection of the five beams a lattice of microtraps is formed; each mictrotrap is 10μm x 10μm x 100 μm in size. Three primary experiments will be discussed. The purpose of this work is the development of high density, mesoscopic atomic samples for use in studying Rydberg physics.

The first experiment described in this dissertation uses the HAT to attain high phase space densities approaching the quantum phase transition into a Bose Einstein Condensate. The phase space density is increased by preforming forced evaporation in the HAT. A model has been developed to understand the evaporation dynamics. Using the model as a guide for how to efficiently lower the trap depth, phase space densities of 1.1 are demonstrated. During evaporation, the number of atoms in the HAT are measured with either a calibrated absorption imaging system or Spatial Heterodyne imaging (Kadlecek *et al.*, 2001).

The second experiment uses the HAT to attain high density atomic samples (Sebby-Strabley *et al.*, 2004). Atoms are evaporated from the HAT until the phase space density approaches unity. Then the trap depth is rapidly increased to compress the atom cloud. The result is atomic densities in excess of 1×10^{15} atoms/cm^3, the highest atom densities attained in incoherent ultracold matter. We have verified these densities three ways: measuring the number of atoms, the temperature, and the oscillation frequency of the atoms in the cloud; measuring the 3-body recombination rate; and measuring the spatial profile of the dense atomic clouds.

In an extension of the second experiment which produced the high density sam-

ples, we have produced and observed mesoscopic atom samples (Sebby-Strabley *et al.*, 2004) which contain 2000 atoms and are 5.6 μm in the longest direction. Creation of these samples represents an important step towards the first observation of a complete dipole blockade and eventually the realization of using Rydberg atoms for quantum computation (Lukin *et al.*, 2001). A further extension of this work is to generate one Rydberg atom in a HAT microtrap, and this will blockade further Rydberg excitation. By exciting one Rydberg atom to n=95, we estimate the probability of a second excited atom in a single compressed microtrap is $< .001$.

The final experiment described in this dissertation is a prelude to the Rydberg experiments in the HAT: the creation of 46d and 48s Rydberg atoms in a Magneto-optical trap (MOT), and the investigation of suppression of Rydberg excitation from Rydberg-Rydberg interactions. The Rydberg atoms created in this experiment have a range of influence much less than the size of the atomic cloud. In this case the excitation is suppressed, not blockaded. The Rydberg atoms were excited by either a single photon excitation from the $5P_{3/2}$ to nl state or by a two photon excitation from the $5S_{1/2}$ to the nl Rydberg state. This work is the first demonstration of a two photon excitation of Rydberg atoms in a MOT. This work also presents the first measurements of the absolute loss rate of atoms from the MOT due to Rydberg excitation. The fundamental lower limit on the loss rate of Rydberg atoms from the MOT is given by the black body ionization rate. Given this, the measured loss rates are approximately 25/sec, over a factor of 3 lower than expected. A model describes the loss rates due to Rydberg excitation. Built into the model is the suppression of excitation to the Rydberg state from Rydberg-Rydberg interactions. The fit to the model suggests that excitation to the Rydberg state is suppressed.

0.2 Acknowledgements

First off, I would like to thank my thesis advisor, Thad Walker. It is fun to work with someone who loves their job as much as Thad does. Even though I worked really hard and often I complained about how hard I was working, I did so because Thad made it fun. Because of his enthusiasm, there were days when I did not even have time to eat breakfast because I was so excited to get into the lab and get to work. Needless to say, a learned a lot from Thad, and I am very grateful that he was my advisor. My hope is that in the near future Thad breaks down a buys a really slick, fast rode bike and then stops complaining that his graduate students have nicer bikes than he does.

Another person that deserves a lot of recognition is Ray Newell. Ray was an ideal lab partner. Ray fostered an excellent environment to discuss new ideas, re-examine old ideas, or sometimes just try to figure out why nothing was working. Furthermore, Ray is a good friend. It was great to work with someone who always had time for a laugh and was willing to talk about more than just physics. I wish Ray a lot of luck at Los Alamos and whatever comes after that.

Next on my list is Matthew Marcus. I really got to know Matthew while studying for the qualifying exam, and it is largely to his credit that I passed. I will miss our 6 pm "stupid-question meetings" in his office (as well as the *occasional* pitcher of beer). Matthew has taught me a lot about physics and has helped me look at atomic physics problems in a more general way so that I always left his office with a clearer picture of the problem at hand.

I would also like to thank fellow Atom Trainers for their support, help, and friendship. I have had the privilege of working directly with Steve Kadlecek, Jason Day, and Erik Brekke. Other Atom Trainers who have been a great influence on me

included Ian Nelson, Bien Chann, and Earl Babcock. It has been great to have such a talented network of people with such a wide base of expertise to ask questions of. I could not have imagined a better group of people to work with.

I have also benefited a great deal from discussions and friendships with people outside my research group. The expertise of the QC group including Pasad Kulatunga, Deniz Yarvuz, Todd Johnson, and Erik Urban has been instrumental in the completion of this work. I have also been lucky to have many good friends including Olivia Castellini, Christian Ast, Erik Spence, and Jessica McChesney who have made this place a better place to be. Aside from graduate students and postdoc's, I have had the pleasure of working with a number of talented people within the physics department, most notably Mike Murray and Ed Slotten. Mike has provided a wealth of knowledge, not all of it pertaining to electronics. Ed's service to the department is extraordinary, but more importantly, Ed is also a good friend

My brother, Dave, and sister, Joanne, have also been of great support and always a ton of fun to visit when time allowed. I know my parents, Joel and Carol, silently questioned my judgement when I decided to go into physics instead of accounting. But like they had done my entire life, they supported me and believed in me. I really appreciate this, and besides, they knew that I would have made a lousy accountant. My parents raised all three of their kids to believe that hard work can get any job done. That is the number one quality that has gotten me here today.

And lastly, I owe a great deal of gratitude to my husband, Bob. To put it mildly, being apart for you has really been a bummer. But thank you for understanding why this was important to me and for never asking me to leave. Thanks for all the flowers. They made us being apart more toleratble. I cannot wait to start our new jobs together in Maryland. It is along time coming and will be worth every minute of it.

Contents

List of Figures

List of Tables

Chapter 1

Introduction

1.1 Background and Motivation

Two of the most exciting areas in atomic physics involve recent developments in quantum computing and quantum manipulation, and the studies of Rydberg atoms in cold atomic clouds. Typically Rydberg experiments with cold atoms are done in Magneto-optical traps (MOTs) which tend to have large spatial scales ($\approx$ 1 mm) and contain many atoms (N $> 10^6$). Thus, experiments with Rydberg atoms have been limited to densities found in MOTs ($10^{10} - 10^{12}$ atoms/cm^3). Conversely, the majority of atomic physics experiments in quantum computation and manipulation have been done using only a few atoms or even a single atom stored in an tightly confined optical trap or high finesse cavity (Sauer *et al.*, 2004) (McKeever *et al.*, 2004) . Relatively few experiments have been done at an intermediate length scale with a large ensemble of atoms. While the fields of quantum manipulation and Rydberg atoms have generated much recent interest and made profound forward progress, there is a need in both of these fields for small and/or dense atomic samples. The primary result of this dissertaion is a robust demonstration of high density ($> 10^{15}$ atoms/cm^3) mesoscopic (5 - 10 μm) atom samples which are ideal for quantum manipulation and computation

involving Rydberg atoms.

Experiments with Rydberg atoms date back to 1885 when Rydberg atoms were detected in the Balmer series of Hydrogen. More recently Rydberg atoms have been generated in Magneto-optical traps. The first generation of Rydberg atoms in a cold atomic sample was in 1998 (Anderson *et al.*, 1998). Since then Rydberg physics using cold atom samples has revealed many new phenomenon. For instance, several groups have used Rydberg atoms to create cold plasmas (Roberts *et al.*, 2004) (Gallagher *et al.*, 2003) (Walz-Flannigan *et al.*, 2004) (Simien *et al.*,2004). Ion formation and dynamics of the resulting plasma are becoming well understood. However, this work has been limited to atomic densities attainable in a Magneto-optical trap. Generating Rydberg plasmas in the samples presented here, which have orders of magnitude higher densities than MOTs, promises to reveal more new and interesting phenomenon. Furthermore, new proposals (Greene *et al.*, 2000) (Boisseau *etal.*, 2002) (Farooqi *et al.*, 2003) predict the existance of novel ultralong range Rydberg molecular states. The formation of these Rydberg molecules require extremely high densities to attain significant production rates. These molecules have been called "trilobite" molecules because the molecular wave function resembles a trilobite (a hard-shelled segmented prehistoric creature that existed in the Earth's ocean 300 million years ago). Greene (Greene *et al.*, 2000) suggests that in dense atomic samples, on the order of 10^{15}atoms/cm^3, trilobite molecules should be observable.

Other topics that could be addressed with Rydberg atom production in high densities atomic samples are line broadening and spectral shifts. Line broadening occurs when collisions change the atomic phase during absorption or emission of a photon. This results in greater variance of the frequencies emitted or absorbed and thus broadens the respective line. Line broadening is important to understand as it is a probable source of decoherence in quantum computing. Similarly, spectral shifts are

also a result of collisions but can come from two sources: collisions involving the highly excited electron or collisions involving the Rb ion. Spectral shifts were first calculated by Fermi and have been measured in the presence of buffer gases, but no measurements have been made in a cold atomic gas at densities in excess of 10^{14} atoms/cm^3.

While high density samples have many applications, experiments at the frontier of atomic physics also require small atomic clouds (5-10 μm in the largest dimension). Recently, Lukin *et al.* (Lukin *et al.*, 2001) proposed using Rydberg atoms to perform quantum logic. They predicted that a long range dipole-dipole interaction produced by a Rydberg atom would block the excitation of other Rydberg atoms. Evidence for suppression of Rydberg excitation has been seen in MOTs where the blockade range is much smaller than the sample size (Singer *et al.*, 2004) (Tong *et al.*, 2004). In theory this suppression could turn into a total blockade if the sample size was less than the blockade range. The atomic samples demonstrated in this dissertation have a radius of 5.7 μm. These samples fit the criteria that their spatial scales are less than the range of influence of a highly excited Rydberg atom, and these samples would be excellent candidates for the demonstration of dipole blockade.

In this disseration we report on using a Holographic Atom Trap (HAT) (Newell *et al.*, 2003) to form high density, mesoscopic atom samples (Sebby-Strabley *et al.*, 2004). The method involves performing forced evaporation in the HAT to high phase space densities followed by a recompression of the trap depth. This work represents significant advances in the field. No other experiment has demonstrated mesoscopic atom ensembles suitable for the demonstration of dipole blockade. The samples presented in this thesis are the first demonstration of atomic clouds well-suited to investigate high speed, high fidelity collective coherent quantum manipulations. Furthermore, the densities presented here are the highest densities demonstrated in ultracold incoherent matter. The ability to use a "classical" gas to do experiments, such as long range

molecule formation between Rydberg atoms, greatly simplifies the needed experimental resources and adds versatility to the experiment.

1.2 Summary of the Dissertation

This dissertation discusses experiments involving the Holographic Atom Trap (HAT) (Newell *et al.*, 2003). Three primary experiments will be discussed: force evaporation in the HAT to high phase space density, creation of high density mesoscopic samples in the HAT, and generation of Rydberg atoms in the MOT as a prelude to future work in the HAT. The overall purpose of the work described in this dissertation is the development of high density, mesoscopic atomic samples for use in studying Rydberg physics.

The dissertation begins with the description of the HAT. The HAT is a novel far-off resonant optical trap formed by the interference of five Nd:YAG laser beams. At the intersection of the five beams a lattice of microtraps is formed; each microtrap is 10μm x 10μm x 100 μm in size. Using an interference pattern to form the trap has two advantages: the resulting trap depth is 3 times larger than if the light was simply focused to form a single beam optical trap, and the rapid spatial variation in intensity tightly binds the atoms yielding high oscillation frequencies. The HAT is unique in that it enjoys high oscillation frequencies yet can store many atoms per site. These two features make the HAT an excellent candidate for rapidly achieving high atom densities and high phase space densities. We have developed an efficient loading procedure to transfer atoms from the Magneto-optical trap (MOT) into the HAT. Using this loading procedure we are able to load 36,000 atoms into each microtrap. After loading we have demonstrated phase space densities of 1/200 and atom densities in excess of 2×10^{14} atoms/cm^3. The discussion of the HAT is divided into two chapters. The first chapter will develop the theory of the HAT. The second chapter will discuss

the diagnostic methods for characterizing the HAT, loading the HAT from the MOT, and some results attained in the HAT.

Included in Chapter 3 is a discussion of imaging systems. Two imaging systems have been implemented in the development of the HAT: absorption imaging and spatial heterodyne imaging. Our implementation of absorption imaging is novel in that it is calibrated. Our imaging laser is stabilized to an optical transition which optically pumps atoms to a different hyperfine state after the atoms scatter two photons. Once optically pumped the atoms no longer interact with the imaging laser. Determining the number of atoms is trivial: the number of atoms is the number of photons absorbed from the probe beam divided by two. The second imaging system used in this experiment is Spatial Heterodyne imaging (Kadlecek *et al.*, 2001). Spatial Heterodyne imaging is a interferometric nondestructive imaging system which measures the phase shift imprinted on an off-resonant probe beam as it passes through the atom cloud. The probe beam is interfered on a CCD camera with a reference beam which does not go through the atoms, resulting in a set of straight line fringes warped at the location of the atom cloud. The information about the atoms is extracted in a method analogous to lock-in detection. Spatial Heterodyne is the most nondestructive imaging system ever used to image cold atoms, capable of imaging cold atoms with a signal to noise of 10 while only scattering 0.0004 photons/atom.

Chapter 4 of this dissertation describes an experiment which uses the HAT to attain high phase space densities approaching the quantum phase transition into a Bose Einstein Condensate. The method described in this experiment will serve as a fundamental piece in the development of the high density mesoscopic atomic clouds discussed in Chapter 5. The phase space density is increased by performing forced evaporation in the HAT. This is achieved by lowering the trap depth in such a way that the phase space density is maximized. A model has been developed to understand

the evaporation dynamics. The model describes evaporation as a two step sequence: lowering the potential followed by rethermalization. The two steps are repeated over and over, and the next step cannot start until the previous step has been completed. Using the model has a guide for how to efficiently lower the trap depth, phase space densities of 1.1 are demonstrated. During evaporation, the number of atoms in the HAT are measured with either absorption imaging or Spatial Heterodyne imaging, and the temperature of the atoms is measured via time-of-flight. The temperature agrees perfectly with the temperature predicted in the theoretical model, however, this work reports on a discrepancy between the number of atoms predicted by the theory and the number of atoms measured. This discrepancy is most likely caused by the presence of a heating mechanism.

Chapter 6 is devoted to the discussion of heating mechanisms. Heating mechanisms can be disguised as atom loss during evaporation: evaporation will always cause the temperature to decrease, but if a heating mechanism is present the evaporation process will cause excess atom loss. Two types of heating mechanism are discussed: heating from the confining laser and heating due to collisions with the background atoms. The heating rates from these sources were estimated and compared with theoretical rates which would account for the atom loss seen in the experiment. From our estimates we concluded that even after a factor of 5 improvement in the quality of the vacuum from previous work (Newell, 2003), at large trap depths the dominant heating mechanism is from quantum diffractive collisions with the thermal background Rubidium atoms. At lower trap depths heating from laser intensity noise and secondary collisions are important. In this chapter we discuss a new heating mechanism: torque heating, and derive equations for the heating rate. This work represents the first study of this type of heating. A complete derivation of the heating rates associated with torque heating is given in Appendix E.

Using a method discussed in Chapter 5, we have developed a way to measure heating rates. The measured heating rates are in good agreement with the quadrature sum of of the heating rates due to laser induced intensity noise, quantum diffractive collisions, and secondary background collisions. Heating due to quantum diffractive collisions and secondary background collisions have been included in the evaporation model. With the inclusion of these heating rates, the model does a better job of predicting the number loss and the ultimate phase space density. The remaining discrepancy between the theory and the experimental results is most likely due to intensity noise from the YAG laser which was not included in the evaporation model. With the inclusion of these heating rates, the model predicts that the phase transition to quantum degeneracy is not attainable given the current initial conditions.

Chapter 5 of this dissertation discusses a second experiment which uses the HAT to attain high density atomic samples (Sebby-Strabley *et al.*, 2004). Atoms are evaporated from the HAT by decreasing the trap depth until the phase space density approaches unity. Then the trap depth is rapidly increased to compress the atom cloud. The result is atomic densities in excess of 1×10^{15} atoms/cm^3, the highest densities attained for ultracold incoherent matter. This result represents one of the primary goals of this work. We have verified these densities three ways: measuring the number of atoms, the temperature, and the oscillation frequency of atoms in the trap; measuring the 3-body recombination rate; and measuring the spatial profile of the dense atomic clouds. The 3-body recombination rate is proportional to n^2. Our measurements of the 3-body recombination rates are in close agreement with previous measurements (Burt *et al.*,1997), a solid verification of our densities. To our knowledge, this work is the first work to measure 3 body recombination rates in a pure optical trap. The measurements were repeated in a bias magnetic field similar to a field typically found in a magnetic trap; we found this did not alter the measured rate.

Also discussed in Chapter 5 is the production of mesoscopic atom samples (Sebby-Strabley *et al.*, 2004). According to the Oxford English dictionary, the word mesoscopic refers to a length scale "between macroscopic and atomic (typically between 10^{-6} m and 10^{-8} m). Hence: influenced by or exhibiting both quantum and macroscopic phenomena." We have produced and observed atomic clouds containing 2000 atoms and are 5.6 μm in the longest direction. Creation of these samples represent an important step towards the first observation of a complete dipole blockade and eventually the realization of using Rydberg atoms for quantum computation [Lukin *et al.*, 2001]. In a Rydberg blockade one, and only one, atom is excited into the Rydberg state. For this to happen the length of the atomic sample must be less than the range, or radius, of influence for an excited Rydberg atom, and the minimum interaction between a pair of atoms must be sufficiently large to block the excitation of the pair of atoms. Evidence for suppression has been seen in MOTs where the range of influence of the excited Rydberg atom is less than the size of the atomic sample (Singer *et al.*, 2004) (Tong *et al.*, 2004). The ultimate goal of this work is to demonstrate atomic samples which have a radius less than the range of influence of an excited Rydberg atom, and then use these clouds to generate one Rydberg atom in the HAT and blockade further Rydberg excitation. In the absence of an external electric field, the interaction between the Rydberg atoms is the van der Waals interaction ($\sim 1/R^6$). By exciting a single Rydberg atom with a principal quantum number of n=95 in a HAT microtrap, the mean Rydberg-Rydberg blockade shift is predicted to be in excess of 20 MHz resulting in probabilities of exciting a second atom as low as .001. The calculation for estimating this probability is shown in Appendix B.

A stronger interaction between Rydberg atoms can be achieved by creating a static electric field and inducing a permanent dipole moment in the atoms. The atoms then interact in a $1/\mathrm{R}^3$ dipole-dipole potential. The drawback of this potential is that

at 54.7° the potential is zero, and at angles close to 54.7° the interaction is weak. This would cause an incomplete blockade if atom pairs were oriented at angles close to 54.7°. If one atom in the pair is excited to the Rydberg state, there would be no mechanisms for blocking the excitation of the atom pair. In the HAT, however, the trap geometry is so anisotropic that this effect is suppressed. For atom pairs with a weak dipole-dipole interaction there is still a strong van der Waals interaction to prevent the excitation of a pair of Rydberg atoms. We estimate a mean dipole-dipole blockade shift in excess of 400 MHz. Under these conditions the probability of exciting two atoms within a single microtrap is 10^{-7}. The small size and the anisotropic nature make the HAT well-suited to investigate coherent quantum manipulations.

The final experiment, described in chapter 7 of this dissertation, is a prelude to the Rydberg experiments in the HAT: the creation of 46d and 48s Rydberg atoms in the MOT and investigation of suppression of Rydberg excitation from Rydberg-Rydberg interactions. The Rydberg atoms created in this experiment have a range of influence much less than the size of the atomic cloud. In this case the excitation will be suppressed, not blockaded. The Rydberg atoms were excited by either a single photon excitation from the $5P_{3/2}$ to nl state or by a two photon excitation from the $5S_{1/2}$ to the nl Rydberg state. This work is the first demonstration of a two photon excitation of Rydberg atoms in a MOT. A two photon excitation is preferable for coherent quantum manipulations because the intermediate state is negligible. In the single photon excitation atoms can decay from the $5P_{3/2}$ to the $5S_{1/2}$ without being excited to the Rydberg state which is a source of decoherence. Furthermore, the two photon excitation will be necessary for exciting Rydberg atoms in the HAT. The use of resonant light in the one photon scheme will be a source of heat for atoms in the HAT and will limit the timescale for doing experiments to only tens of microseconds.

This work also presents the first measurements of the absolute loss rate of atoms

from the MOT due to Rydberg excitation. The loss rate is extracted from the MOT fluorescence signal. We measure a maximum loss rate of 25/sec. The fundamental lower limit on the loss rate of Rydberg atoms from the MOT is given by the black body ionization rate which has been calculated to be 290/sec at n=50. Given this, the measured loss rates are over a factor of 3 lower than expected. A model is presented which describes the loss rates in the MOT due to Rydberg excitation. Built into the model is the suppression of excitation to the Rydberg state from Rydberg-Rydberg interactions. The model describes the system as a four level system. The evolution of the populations in each of the levels is described by a set of rate equations. Our data is compared to the model under the conditions that no suppression is present. At low powers of the Rydberg excitation laser, the loss rates predicted by the no-suppression model agree quite well the the measured loss rates. At higher laser powers the measured loss rate saturates but at a lower power than the model loss rate saturates. The deviation of the data from the no-suppression model signifies the presence of Rydberg-Rydberg suppression. From the fit to the model, the extracted range of influence of the Rydberg atoms is approximately 5μm, approximately 50 times the classically calculated radius.

This is ongoing work. Current work is investigating the loss rates at a lower principle quantum number. The interaction between Rydberg atoms due to the van der Waals potential should scale as n^{11}; at lower principal quantum number no suppression is expected, at higher principal quantum number substantial suppression should be observed. The next step in this experiment is to create Rydberg atoms in the HAT and try to observe a complete Rydberg blockade.

The dissertation concludes with a summary of the work presented here and a discussion of the current and future work.

Chapter 2

Holographic Atom Trap

2.1 Introduction

In this chapter we will discuss a novel far-off resonant optical dipole trap, the Holographic Atom Trap (HAT) (Newell *et al.*, 2003). The goal for this work was to create a trapping potential that would readily lend itself to the formation of high density and high phase space density clouds. The HAT is formed by the interference of five Nd:YAG beams. The resulting interference pattern is a collection of small, cigar shaped traps. While the traps are small, 10 μm x 10 μm x 100 μm, we can load many atoms per site.

I will begin this chapter with a basic introduction to optical dipole traps. The interaction between the atoms and the confining laser can be minimized by using a far-off resonant optical trap (FORT). FORTs have been employed in many research groups, for instance, (Barrett *et al.*, 2001) (O'Hara *etal.*, 1999), because FORTs have demonstrated long storage time while having virtually no effect on the trapped atoms.

Next I will discuss the theory of the Holographic atom trap, primarily the geometry of the interference pattern. The oscillation frequencies of atoms in the HAT are measured with parametric excitation. The procedure for measuring the frequencies is

discussed, and we report the measurements of $\nu_x = \nu_y = 18.9$kHz and $\nu_z = 760$ Hz. These measurements are in good agreement with the calculated value for the oscillation frequencies. For future reference equations for density, phase space density, thermal radius, and elastic collision rate are given.

Finally I will discuss the apparatus. The apparatus has four primary components: the YAG laser, the optical train, the intensity stabilizer, and the Magneto-optical trap (MOT). The YAG laser is a CW multimode-mode flashlamp-pumped laser. Since the path length difference between the five beams which interfere to form the HAT is small, the coherence length can be short permiting the usage of a multimode laser. We have measured the coherence length to be 7.56 cm (Newell, 2003), and we have measured the M^2 to be 1.07. The primary components of the optical train are an AOM, the diffraction grating, and the transfer lenses which image the diffraction grating onto the atom cloud. The intensity stabilizer is used to remove intensity noise from the laser. It will be discussed in Chapter 6. A diagram for the intensity stabilizing feedback circuit is shown in Appendix C.

The last major component of our apparatus is the Magneto-optical trap (MOT). The HAT is loaded from the MOT. While the details of the loading procedure will be given in the following chapter, I will end this chapter with a discussion of the MOT utilized in this work. MOTs have become commonplace in many of today's atomic physics experiments. MOT technology is so well developed that it has become as much of a tool in atomic physics as an object of study. Many excellent references describe the fundamentals of MOTs (Metcalf and van der Straten, 1999), and for that reason, the physics behind a MOT will not be discussed here. I will focus on giving some details specific to our MOT. Typically we can trap and cool 1.56 x 10^8 Rubidium-87 atoms in a MOT cloud with a 1 mm radius giving a density of 3.7 x 10^{10} atoms/cm^3. We have measured the temperature of atoms in the MOT to be in good agreement

with the predictions of Gertz *et al.* (Gertz *et al.*, 1993). To attain higher densities we employ a dark SPOT MOT (Ketterle *et al.*, 1993). We have measured our densities with the technique of spatial heterodyne imaging, also discussed in the next chapter, to be 4×10^{11} atoms/cm^3, an order of magnitude larger than the density of our standard MOT.

2.2 Theory

2.2.1 Optical Dipole Traps

The essence of an optical dipole trap is to use a laser to induce an oscillating electric dipole moment on the atoms. If the laser field is inhomogeneous (focused), this interaction exerts a force on the atoms. Depending on the detuning of the laser relative to the atomic resonance, the force that the dipole traps exerts on the atom can be either attractive (detunings below the atomic resonance) or repulsive (detunings above the atomic resonance).

2.2.2 Far-off Resonant Traps

The simplest type of Far-off Resonant Trap (FORT) is one laser brought to a tight focus, w_0. The radial intensity pattern is given by

$$I(r) = I_0 e^{-r^2/w_0^2}. \tag{2.1}$$

If the laser is below the atomic resonance, a red detuned FORT, the ground state energy level of the atom is shifted downward with the largest shift at the point of highest intensity. Hence atoms are attracted to the high intensity regions. The opposite is true for a Blue detuned FORT. The force exerted on the atoms is

$$F = -\nabla U = -\frac{2\pi\alpha}{c}\nabla I \tag{2.2}$$

in other words, the tighter the focus, the stronger the confining force on the atoms. Experiments with FORTs have achieved higher densities than a standard MOT can achieve, for example in (Miller *et al.*, 1993) they report densities of 8 x $10^{11}/\text{cm}^3$.

2.3 Holographic Atom Trap

In this experiment we extend the idea of a single far-off resonant trapping beam to the use of five beams to form an interference pattern. An interference pattern is an easy way to form a rapid spatially varying potential. This rapid spatial variation yields high oscillation frequencies, yet the resulting potential has a large enough trapping volume that many atoms can be trapped per site. The combination of high oscillation frequencies and many atoms per site make the Holographic Atom Trap, HAT, a good choice for achieving high densities and phase space densities.

2.3.1 Geometry of Interference Pattern

In the HAT the trapping potential is formed by the interference of five beams derived from a diffraction grating as shown in figure 2.1. Four of the beams are first order diffracted beams; the fifth beam is the zeroth order beam. A cartoon of the collimated diffraction pattern is shown in Figure 2.2. Taking the z-direction to be the propagation axis for the laser and assuming that the intensities of the 1^{st} order diffracted beams are equal, the electric field at the intersection of the five beams can be written as

$$E = E_0 \left(1 + 2\beta e^{\frac{-ik\theta z}{2}} \left[\cos k\theta x + \cos k\theta y\right]\right) \tag{2.3}$$

where β is the ratio of the electric field of a single first-order beam to the electric field of the zeroth order beam and θ is the angle for the first order beams with respect to the zeroth order beam. By squaring equation (2.3), we can write the intensity at the

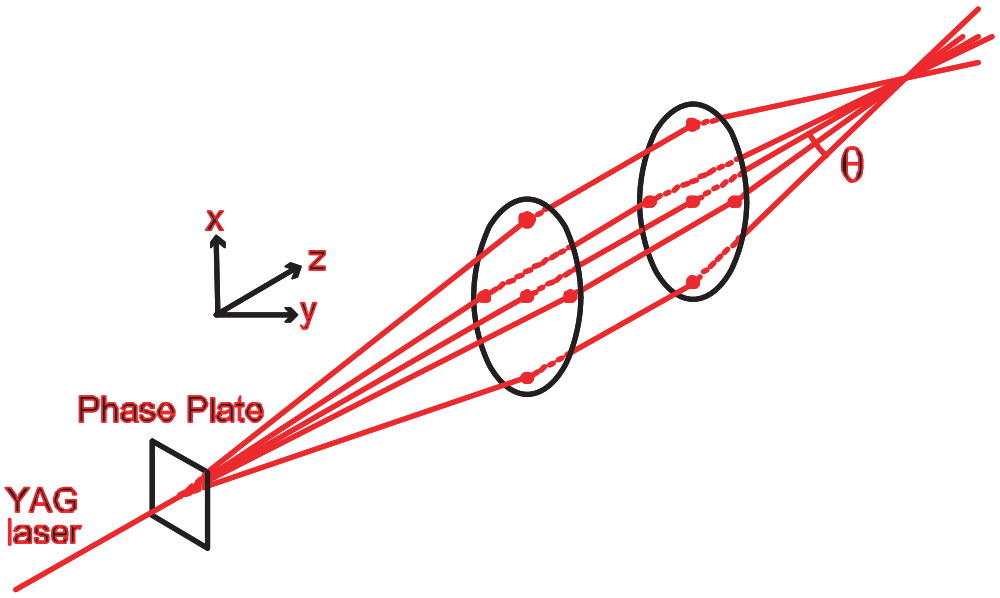

Fig. 2.1.— The Holographic Atom Trap

intersection region to be

$$I(x,y,z) = I_0\left[1 + 4\beta^2\left(\cos kx\theta + \cos ky\theta\right)^2 + 4\beta\cos\frac{kz\theta^2}{2}\left(\cos kx\theta + \cos ky\theta\right)\right] \quad (2.4)$$

where I_0 is the intensity of the zeroth order beam. The calculated intensity pattern is shown in figure 2.3.

At the center of the trap $x = y = z = 0$ the maximum intensity is

$$I_{max} = I_0\left(1 + 8\beta + 16\beta^2\right) \quad (2.5)$$

where I_0 is the intensity of the zeroth order beam. The term $(1 + 8\beta + 16\beta^2)$ is due to the interference pattern. By measuring the ratio of the first-order intensity to the zeroth-order intensity, we have measured the β for our phase plate to be $\beta = 0.46$. Prior to the phase plate, the YAG power is 16 Watts, whereas the power in the center beam is only 6 Watts. Formation of the interference pattern yields a factor of 3 enhancement

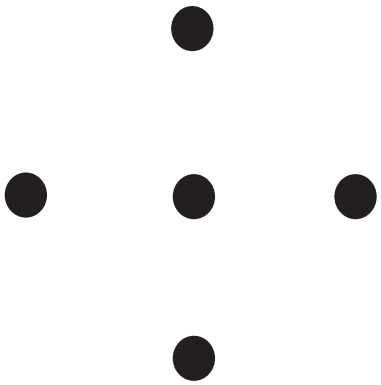

Fig. 2.2.— Far field diffraction pattern from the phase plate.

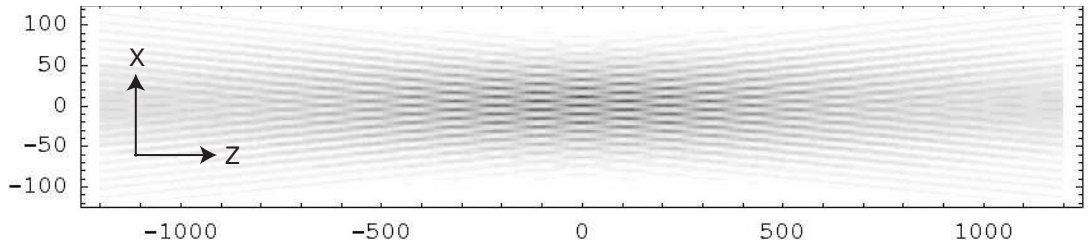

Fig. 2.3.— HAT intensity pattern.

in the trap depth as opposed to just using the 16 Watts focused to the same beam waist to form a standard FORT.

The trapping potential seen by an atom is given by

$$U(r) = -\alpha \mid E \mid^2 = -\frac{2\pi\alpha}{c} I(r) \tag{2.6}$$

where α is the static polarizability of the Rb-87 ground state at λ=1064 nm and $I(r)$ is given in equation (2.4). The polarizability was measured to be 114 $\pm$ 9 Å^3 (Kadar-Kallen *et al.*, 1992), which agrees with the calculated value of 98.8 Å^3. Along the light propagation direction (z-axis), interference fringes arise from the Talbot effect (Talbot,(1836)) (Boiron *et al.*, 1998). We call these Talbot fringes. The Talbot effect is formally defined as the periodic self-imaging of a diffraction grating, and appears here as a result of the phase variances between the first order diffracted beams leading to periodicity along the z-axis. Within each Talbot fringe there is a lattice of smaller traps, which we call microtraps. The resulting trapping potential of each microtrap gives strong confinement in the x and y-direction, but a weaker confinement in the z-direction. The center microtrap has the deepest trapping potential given by

$$U_{max} = -\frac{2\pi\alpha}{c} I_{max}. \tag{2.7}$$

In the limit that the microtrap spacing is much less than the beam waist, the trap depths of the other microtraps can be approximated by

$$U_{i,j} = U_0 e^{-\lambda^2 i/(\theta^2 w_x^2)} e^{-\lambda^2 j/(\theta^2 w_y^2)} \tag{2.8}$$

where w_x and w_y are the Gaussian beam waists in the x and y direction respectively and i,j count the microtraps (i,j=0 for the center trap; i,j=1 for the first outer well, etc.). In the x and y direction the size scale for the microtraps is given by $\frac{\lambda}{\theta}$ and in the z-direction the Talbot fringe spacing goes as $\frac{\lambda}{\theta^2}$. For a typical value of $\theta = .1$ radians

the microtrap dimensions are 10 μm x 10μm x 100μm. Typically $w_x = w_y = 92$ μm. Since 10 μm $\ll w_x$,w_y the approximation we made for equation (2.8) is valid.

The x, y, and z oscillation frequencies in the microtraps can be calculated by $\nu = \frac{1}{2\pi}\sqrt{\frac{\kappa}{m}}$ where κ is the spring constant given by $\kappa = -\frac{d^2U(r)}{dr^2}$. The explicit equation for the spring constants are

$$\kappa_x = \frac{16\pi^2\beta(1+4\beta)\theta^2}{\lambda^2(1+8\beta+16\beta^2)}U_{max}, \tag{2.9}$$

$$\kappa_y = \kappa_x, \tag{2.10}$$

$$\kappa_z = \frac{8\pi^2\beta\theta^4}{\lambda^2(1+8\beta+16\beta^2)}U_{max} \tag{2.11}$$

and likewise the oscillation frequencies are

$$\nu_x = \frac{2\,\theta}{\lambda}\left[\frac{\beta\,(1+4\beta)\,U_{max}}{(1+8\beta+16\beta^2)\,m}\right]^{1/2} \tag{2.12}$$

$$\nu_y = \nu_x \tag{2.13}$$

$$\nu_z = \frac{\theta^2}{\lambda}\left[\frac{2\,\beta\,U_{max}}{(1+8\beta+16\beta^2)\,m}\right]^{1/2}. \tag{2.14}$$

In the derivation of these equations I have ignored any effects owing to the Gaussian nature of the beam, which is especially negligible for the center mictrotrap.

The trap depth can be calculated from (2.7) and (2.5). The intensity of the zeroth order beam is simply $I = \frac{2P_0}{\pi w^2}$ where now I will use w to be the geometric mean beam waist, $w = (w_x w_y)^{1/2}$. We have measured the beam waist many different ways to conclude that at the atoms it is approximately 92 μm; the power in the zeroth order beam is 6 W. This gives an intensity of 42 kW/cm^2 and furthermore a well-depth of 600 μK.

The equations given for the oscillation frequencies (4.4) in the center microtrap for our typical parameters of $\theta = 0.1$ and $\lambda = 1064$ nm can be condensed into a convenient form

$$\nu_x = \nu_y = 18.9\ kHz\sqrt{\frac{U_{max}}{600\ \mu K}} \tag{2.15}$$

$$\nu_z = 0.760\ kHz \sqrt{\frac{U_{max}}{600\ \mu K}}. \quad (2.16)$$

We can measure these frequencies with parametric excitation [Friebel *et al.*, 1998]. When the intensity is modulated at twice the oscillation frequency the atoms should experience a heating resonance and will be ejected from the trap. Therefore by measuring the number of atoms in the HAT as a function of frequency, the resonant frequency can be determined. We use the AOM, discussed in (2.5.2), to intensity modulate the YAG light; the modulation is produced by a SRS DS345 digital function generator. We have found that a modulation depth of 20-30% provides a good signal but does not excessively broaden the curve. We have also found it useful to measure the oscillation frequencies at a trap depth lower than the maximum trap depth. There are two reasons for this. First, bandwidth limitations in the various electronic components limit the highest frequency which we can reliably generate. Second, decreasing the trap depth increases the fraction of atoms that occupy the center well. The presence of atoms in the outer wells artificially broadens our signal. This point will be discussed at length in Chapter 4. Our measurements are shown in figure 2.4. We fit the signals to a Gaussian to determine the center of the curve which is $2\nu_{x,z}$. This method is probably overly conservative as the highest frequency which results in atom loss is most likely the resonant frequency of the center well. Nonetheless, by fitting the data to a Gaussian and applying the appropriate scaling factors to account for the measurement being taken at a fraction of the maximum well depth, we measure the oscillation frequencies to be 18.4 ± 1.2 kHz and 735 ± 62 Hz in the x,y and z direction respectively at the maximum trap depth.

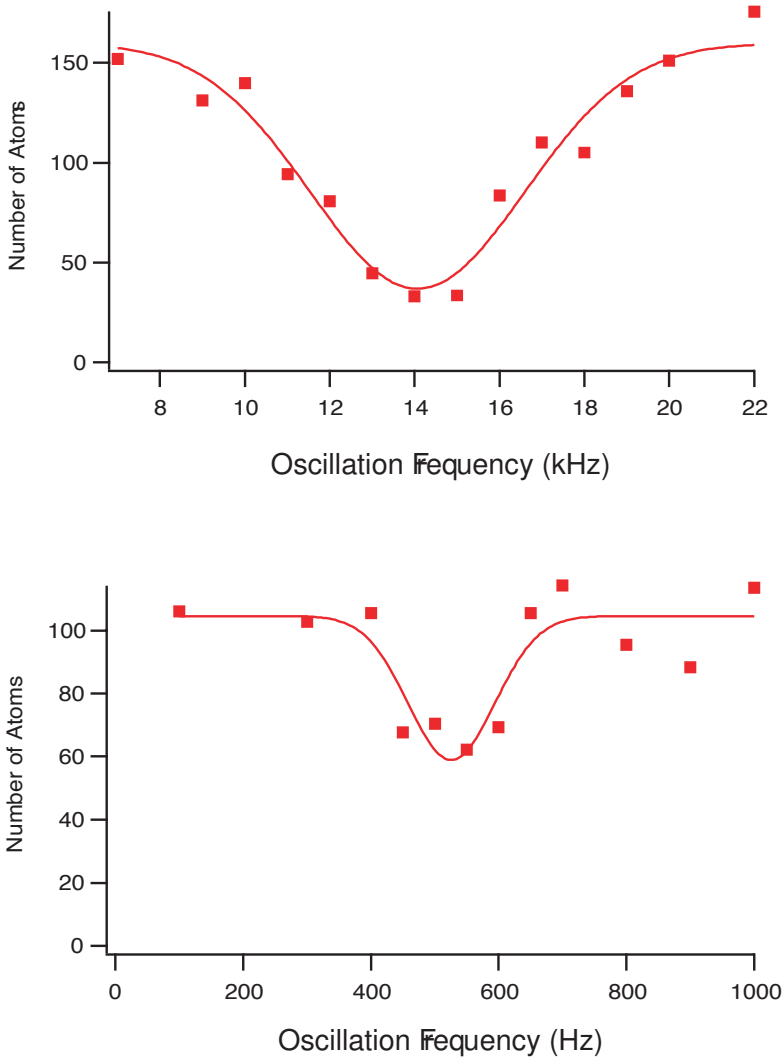

Fig. 2.4.— Parametric heating in the HAT. Figure a) shows heating resulting from excitation of the x-axis and b) shows heating from the z-axis. Both measurements were taken at $U_{max}/6$ then scaled appropriately to determine the oscillation frequencies at maximum trap depth.

2.4 Definition of Thermodynamic Variables

It is experimentally useful to define certain thermodynamic variables, namely number density, phase space density, thermal radius, and collision rate, in terms of HAT oscillation frequencies, temperatures, and number of atoms. In this section I will define these equations. They will be referred to throughout this dissertations.

We will first define the atomic density. We assume a Boltzman density distribution for atoms in the HAT, $n = n_0 e^{-U/kT}$. A convenient equation for the peak atomic density, n_0, can be derived by

$$\begin{aligned} N &= \int_{-\infty}^{\infty} n(x,y,z)\, dxdydz \\ &= n_0 \int_{-\infty}^{\infty} \left(e^{\frac{-m\omega_x^2 x^2}{2kT}}\right)^2 \left(e^{\frac{-m\omega_z^2 z^2}{2kT}}\right) d^2x dz \\ &= n_0 \left(\frac{kT}{2\pi\nu^2 M}\right)^{3/2} \\ n_0 &= \frac{N}{\left(\frac{kT}{2\pi\nu^2 m}\right)^{3/2}} \end{aligned} \tag{2.17}$$

where k is Boltzman's constant. Unless otherwise specified, the notation ν refers to the geometric mean of the x,y, and z oscillation frequencies, $\nu = (\nu_x \nu_y \nu_z)^{1/3}$.

The phase space density is the number of atoms per quantum state. A phase space density of 2.612 marks the Bose-Einsten phase transition. Most generally, phase space density is expressed as

$$\rho = n_0 \lambda_T^3 \tag{2.18}$$

where λ_T is the thermal de Broglie wavelength given by $\lambda_T = \frac{h}{\sqrt{2\pi M kT}}$. In a harmonic trap it is convenient to express the phase space density as

$$\rho = N \frac{(h\nu)^3}{(kT)^3} \tag{2.19}$$

Note in both equations (2.17) and (2.19) the strong dependence on ν. Since the HAT enjoys high oscillation frequencies, it is readily able to produce high density and high phase space density samples.

Above we have identified a size scale for the microtraps, but once the atoms are held in the microtraps they occupy a much smaller, temperature dependent volume which we call the thermal radius. The thermal radius along the ith dimension is , $\sigma_{T,i}$ is given by

$$\sigma_{T,i} = \sqrt{\frac{2kT}{m\omega_i^2}} \tag{2.20}$$

where in this case $\omega_i = 2\pi\nu_i$, the oscillation frequency for the ith component.

Lastly, the elastic collision rate, Γ, is given by

$$\Gamma = n\sigma_e v \tag{2.21}$$

where v is the velocity of atoms in the HAT and σ_e is the cross section for elastic collisions. At low temperature the elastic collisions are dominated by s-wave scattering. For identical bosons the cross section is given by

$$\sigma_e = \frac{8\pi a^2}{1 + k^2 a^2} \tag{2.22}$$

where $k = 2\pi/\lambda_T$. The scattering length, a, has been measured very precisely to be 90 $\pm$ 1a_0 (Roberts *et al.*, 1998). In the limit that $k^2a^2 \ll 1$, σ_e can be approximated as $\sigma_e = 8\pi a^2$. For the highest temperatures measured in the HAT, the k^2a^2 term gives a 25% correction factor. For lower temperatures it is completely negligible.

2.5 Apparatus

In this section I will detail the apparatus we used create our holographic atom trap. An overview of the apparatus is shown in figure 2.5. The primary components are the YAG laser, the holographic phase plate, and the AOM used to intensity stabilize the YAG laser.

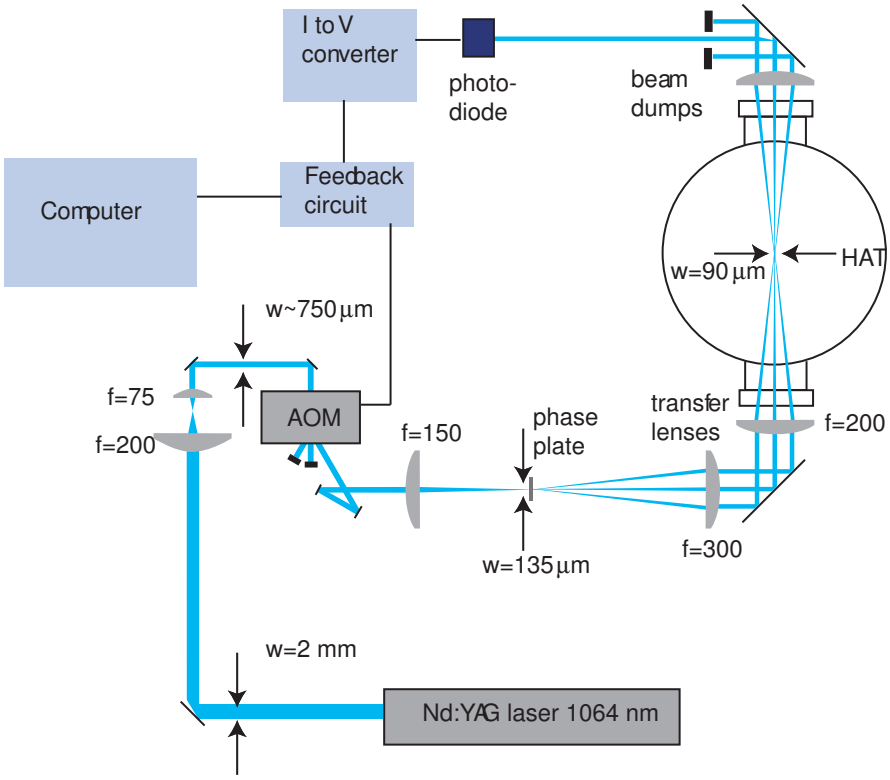

Fig. 2.5.— Optics train for the YAG (image modified with the permission of R. Newell).

2.5.1 YAG Laser

The laser used to make the trapping potential is a Lee Laser series 800 flashlamp pumped Nd:YAG laser with λ=1064 nm. The laser has excellent transverse mode quality with an $M^2 = 1.07$, but has multiple longitudinal modes. The frequency spectrum of the YAG was studied in detail (Newell, 2003) and was found to have a bandwidth of 890 MHz which corresponds to a coherence length of 7.56 cm. The HAT geometry lends itself to the use of a multimode laser. The short coherence length typical of a multimode laser is not a problem in the HAT because the path length difference for any of the five beams is very small ($\ll$ 7 cm). Typically we operate this laser at 18 W CW.

2.5.2 Optical Train

The optical train is shown in figure 2.5. The primary components of the optical train are the phase plate and acousto-optic modulator (AOM).

The AOM that we use is an IntraAction Corp. Model AOM-402AF4 which has a frequency of 40 MHz. This AOM features excellent diffraction efficiency of better than 86% and low insertion loss ($<$ 3%). To achieve these specifications the beam waist is reduced to w = 750 μm before entering the AOM. We have attained the best results using a collimated, rather than focused beam. The purpose of the AOM is three-fold: it provides a method to quickly extinguish the HAT, it allows for us to vary the YAG power and thus the trap depth in the HAT, and it serves as a mechanism for intensity stabilizing the laser. The drawback of the AOM is that it alters the beam quality and the beam shape. We have remeasured the M^2 values after the AOM to be M_x^2 =2.25 and M_y^2=3.17.

The phase plate is an off-the-shelf product of MEMS Optical, Inc. It serves as a transmission diffraction grating. The incident beam is diffracted into many orders, but the majority of the power is contained in the single zeroth order beam and the four first order beams. A mask is used to block all the higher order beams.

An f=150 mm lens prior to the phase plate focuses the beam to a waist of 135 μm at the phase plate. Two lenses after the phase plate, f=300 mm then f=200 mm, image the phase plate onto the MOT cloud with a magnification of 2/3. After passing through the chamber the zeroth order from the holographic grating is imaged onto a fast, battery powered photodiode for the feedback circuit discussed below.

2.5.3 Intensity Stabilization

The intensity stablization is achieved using an external feedback loop. The feedback loop adjusts the RF power going to the AOM so to maintain constant optical power in the AOM's first order beam. We monitor the zeroth order beam of the holographic phase plate and compare that to a Labview generated reference voltage. Reference (Newell, 2003) gives a discussion of the differential amplifier used to remove noise from the reference voltage. A slight modification to the differential amplifier circuit is shown in Appendix C. Though this point will be developed more fully in chapter 6, the importance of removing intensity noise from the laser cannot be stressed enough as intensity noise at certain frequencies can lead to high heating rates. While the feedback loop was discussed in (Newell, 2003), the work here presents two major advances in remedying the intensity noise problem: improved feedback circuit and monitoring the zeroth order beam from the holographic grating rather than a third order beam. The circuit diagram for the current feedback circuit is shown in Appendix C. The bandwidth of the circuit is 22 kHz. The requirements on bandwidth are dictated by the oscillation frequencies in the microtraps. This issue and relevant noise spectrum will be discussed

further in chapter 6.

2.5.4 Magneto Optical Trap (MOT)

We use the MOT as a tool for loading atoms in the HAT. Atoms are first cooled and confined to a small volume, $\approx$ 1mm in radius, using standard, well developed MOT technology. We then overlap the HAT with the MOT to load the HAT. Loading will be discussed in greater detail in Chapter 3, but here I will provide some details of our Magneto optical trap.

The primary components of our vapor cell Rubidium-87 MOT are the vacuum chamber, the confining laser for the MOT, a hyperfine repumping laser, and coils for providing the various magnetic fields. An energy level diagram of the Rubidium 5s and 5p states is given in figure 2.6 as an aid for understanding the roles played by the various lasers discussed below.

I will first describe our vacuum chamber. We use a UHV-grade stainless steel chamber with 10 ports for optical access. UHV vacuum was attained by pumping down from atmosphere with a roughing and turbo pump to 10^{-7} torr. At this point we used a Varian 8 L/s ion pump to further lower the pressure. The pressure inside the chamber was monitored by using the current generated from the ion pump. From this we can conclude that the pressure is less than 1×10^{-8} Torr. To further improve the vacuum we installed a Titanium sublimation pump which is run periodically (approximately 6 times per year).

Once we have achieved UHV we backfill the chamber with a small amount of Rubidium vapor. The Rubidium vapor is provided by heating an oven containing a 1 gram Rubidium ampule. The oven is connected via a valve to the main vacuum champber. The ampule contains both naturally occurring isotopes of Rubidium, Rb-85 and Rb-87, however only the Rb-87 atoms are of interest.

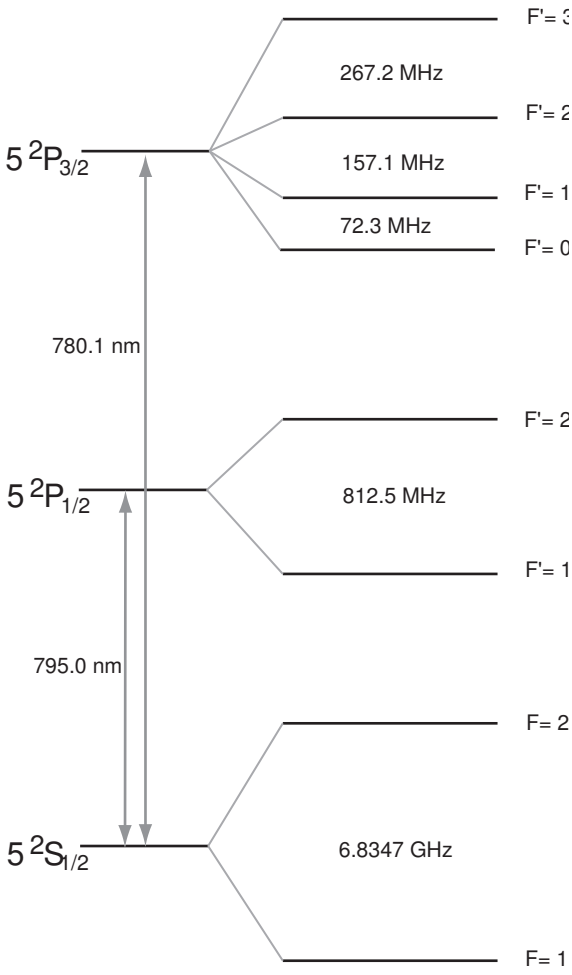

Fig. 2.6.— 5s state of Rubidium-87.

Rubidium atoms from the background vapor are trapped and cooled by 3 retro-reflected lasers in x, y, and z. The lasers are tuned a few natural linewidths (Γ=5.9 MHz) below the cycling transition, $^2S_{1/2}$ $F = 2$ to $^2P_{3/2}$ $F' = 3$. The trapping light is provided by a Schwartz Titanium:Sapphire laser pumped by a Coherent Innova-310 8 Watt Argon Ion laser. The laser is described in greater detail in (Williamson, 1997). The laser is frequency stabilized using Doppler-free FM-spectroscopy. A detailed description of the locking scheme is given in (Newell, 2003).

The laser is locked to the $^2P_{3/2}$ $F' = 1$ to $^2P_{3/2}$ $F' = 3$ crossover. A high efficiency

IntraAction Corp. AOM shifts the light to 18 MHz to the red of the $^2S_{1/2}$ $F = 2$ to $^2P_{3/2}$ $F' = 3$. We double pass the AOM to increase the attainable frequency range and to eliminate any steering effects caused by changing the AOM RF frequency. We can also intensity stabilize the trapping beams by monitoring the power in the trapping beams and feeding back to adjust the RF power driving the AOM. This also allows us to easily adjust the power in the trapping beams by changing the set-point in the stabilization circuit. After the AOM the trapping beam goes through a polarizing preserving Oz-Optics fiber and sent to the trapping table. While several beams are derived from the Ti:Sapph, the majority of the power is devoted to the generation of the trapping beams. Under typical conditions we get 80 mW of light out of the fiber for MOT use.

Once on the trapping table the light coming out of the fiber is collimated. The maximum intensity at this point is typically 90 mW/cm^2. The light is then divided equally into the three orthogonal MOT beams. The Gaussian beam waist of each MOT beam is approximately 1 cm.

Aside from the trapping lasers, a second laser is needed to operate a MOT. In a MOT atoms will scatter photons from the trapping laser until an atom undergoes a Raman transition and ends up in the $^2S_{1/2}$ $F = 1$ state. To return to the F=2 state, a hyperfine repumping laser is used. Our repumper is generated by a Toptica TA-100 external cavity diode laser and taper amplifier system. The Toptica is frequency stabilized by saturated absorption spectroscopy and is locked to the $F' = 1$ to $F' = 2$ crossover, and an AOM shifts the light slightly below (-4MHz) the $^2S_{1/2}$ $F = 1$ to $^2P_{3/2}$ $F' = 2$ transition. Since the branching ratio for emission to the F=2 state is 1/2, on average two photons will be scattered by the repumping before the atom is back in F=2.

The repumper is also fiber coupled for transport to the trapping table. After the

fiber a lens collimates the light; the Gaussian waist of the collimated beam is 6 mm. For optimum MOT loading we use 20 mW of repumper light.

While the viscous cooling force is provided by the trapping lasers and maintained with the aid of the repumper, a magnetic field with B=0 at the intersection of the trapping beams is needed to confine the atoms. This is supplied by a set of magnetic field coils which I will refer to as the MOT coils. Each coil contains 90 turns of 14 Gauge high temperature wire. The average radius of the coil is 4.25 cm. The coils are spaced 9.2 cm apart. Typically we power the coils with a steady-state current of 7 Amps, making a 15 G/cm magnetic field gradient at the trapping region. On short time scales we can increase the gradient to 30 G/cm without causing significant heating or damage to the coils. The coils can be rapidly turned off ($< 100\mu$s) as necessary. Three additional sets of coils, shim coils, in a Helmholtz configuration on orthogonal axes are used to null out the Earth's magnetic field and magnetic fields created by other experiments in the building. The current in each of the coils is independently adjusted (on a daily basis) so that when the MOT coils are extinguished, the MOT cloud uniformly spreads. If the coils do not compensate for the external fields, the MOT cloud will be pushed in a certain direction when the MOT coils are extinguished. Each of the shim coils are 20 turns of 14 Gauge wire which fit over the vacuum viewports.

The previously mentioned components are necessary for achieving a standard, "bright", Magneto-optical trap. While this is sufficient for many applications, the MOT described above has a fundamental density limit. This limit is given by radiation pressure or multiple photon scattering (Walker *et al.*, 1990) (Sesko *et al.*, 1991). Essentially, the MOT cloud will adjust its volume so that the optical density of the cloud is on order 1. This fundamentally limits the density to $\approx 10^{11}$ atoms/cm^3. Several widely used techniques can be used to circumvent this problem and achieve 1 - 2 orders of magnitude higher densities.

One such technique is a spatial dark SPOT MOT (dark spontanteous-force optical trap) (Ketterle *et al.*, 1993). In this method an opaque object is placed in the repumping beam and imaged onto the MOT cloud. This limits the amount of repumping light at the center of the trap where the atoms collect. It does not effect the loading process as atoms load at the edge of the MOT cloud. Using this method, Ketterle *et al.* report the trapping of 10^{10} Sodium atoms at a density of 1×10^{12} atoms/cm^3.

We implement the dark SPOT MOT by imaging a 3.5 mm diameter cross-section of a rubber O-ring onto the MOT cloud. The imaging is done in two dimensions to create a dark volume roughly the size of the MOT cloud. By decreasing the repumper power, the effect of the dark SPOT is increased but at the cost of a lower loading rate. We have found a compromise to occur at $P_{repumper}$=3.2 mW. Under these operating conditions the dark SPOT causes approximately 50% of the atoms into the F=1 state.

The effect of the dark SPOT can also be increased by adding a depumping laser which purposely removes atoms from the F=2 into F=1 (Ketterle *et al.*, 1993). The depumper is made to spatially overlap with the dark SPOT in both dimensions. Like the trapping beams, the depumper is derived from the Ti:Sapphire laser and fiber coupled onto the trapping table. The depumping laser is locked 54 MHz to the blue of the $^2S_{1/2}$ $F = 2$ to $^2P_{1/2}$ $F' = 2$ transition. Again, the fluorescence branching ratio for this transition is 1/2; on average after scattering two photons atoms in F=2 will be pumped into F=1. Typically we use 3 mW of depumping light collimated to a Gaussian waist of 1.2 mm. At this intentsity the depumper reduces the F=2 fraction by an additional factor of 2 making 75% of the atoms occupy F=1.

Other groups (see for instance,(Barrett *et al.*, 2001)) have implemented a dark SPOT in the temporal domain rather than the spatial domain. This is simply done by turning down, or turning off, the repumping laser. In theory this method has the benefits of enjoying large loading rates while still transferring large populations into

the dark state, and there are no alignment issues for overlapping the dark spot and the MOT cloud. In practice we were never able to have as much success with this method (the figure of merit being HAT loading) as with the spatial dark SPOT.

We measure and monitor the number of atoms in the MOT with fluorescence imaging. We collect fluorescing photons with a lens which images the photons onto a large-area photodiode. The current generated by the photodiode is converted to a voltage with a current amplifier. Given the quantum efficiency of the photodiode and of the optical train, the gain of the current amplifier, the solid angle subtended by the lens, the excited state lifetime, and the energy of the fluorescent photons, we can convert the measured voltage to atom number.

Typically for I=90 mW/cm^2 and $\Delta = -3\Gamma$, we measure a fluorescence signal which corresponds to 1.56×10^8 atoms in the MOT cloud.

The number of atoms in the MOT cloud as a function of time is given by

$$\frac{dN}{dt} = L - \Gamma_0 N \tag{2.23}$$

where L is the loading rate and Γ_0 is the loss rate. We measure the Γ_0 by measuring the time constant for loading the MOT. In the limit of high rubidium vapor pressure this time is dominated by background collisions and is independent of trapping laser power. In the limit of low rubidium vapor pressures, Γ_0 is dominated by light induced collisions (Sesko *et al.*, 1989). In this limit the loss rate changes as a function of the trapping laser power. The measured loss rate is given by

$$\Gamma_0 = \Gamma_{lightinduced} I + \Gamma_{bg} \tag{2.24}$$

The contribution to the loss rate due to background collisions, Γ_{bg}, can be determined by plotting loss rate as a function of laser power, as showing in figure 2.7, and extrapolating to zero power.

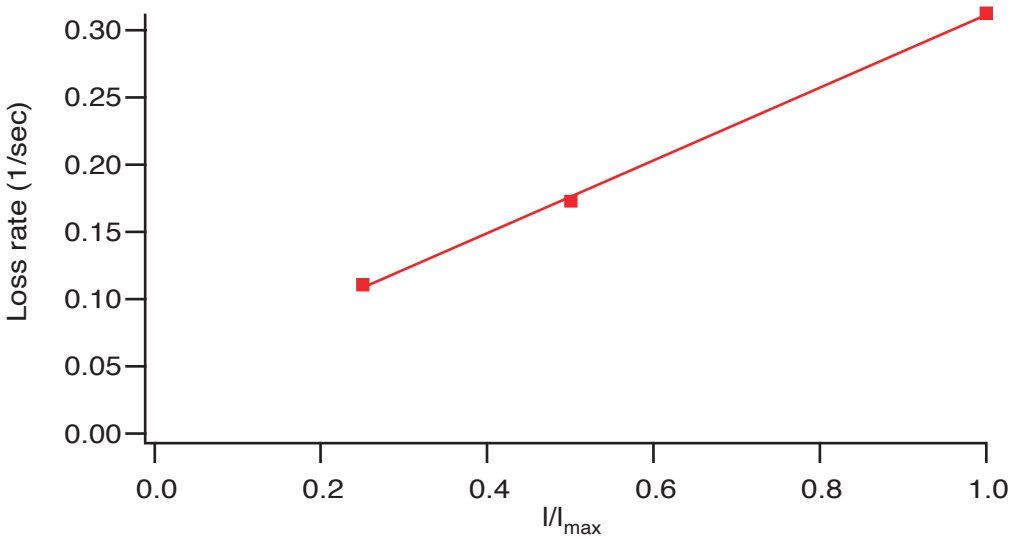

Fig. 2.7.— Loss rate in the MOT as a function of trapping intensity.

From this graph we determine a background loss rate of $\Gamma_{bg} = 0.0038/sec$, or in other words, a lifetime of 26 seconds. This is a factor of 9 improvement over our previous work (Newell, 2003), which is largely due to the installation of a Titanium sublimation pump.

The temperature of atoms in the MOT is determined using a time-of-flight method. A cloud of atoms is prepared 1 cm above a probe beam near resonant ($\Delta = -20MHz$) with the $^2S_{1/2}$ $F = 2$ to $^2P_{3/2}$ $F' = 3$ transition. The trapping lasers and magnetic field are extinguished and the cloud falls through the probe beam. As the atoms fall they ballistically expand at a rate governed by the molasses temperature. The atoms scatter photons from the probe beam; the fluorescence is collected by a lens and imaged onto a silicon photodiode. A typical signal is shown in figure 2.8. From the width of the fluorescence signal, the average temperature of the atoms can be extracted. A detailed explanation of the time-of-flight signal analysis is given in (Newell, 2003) and the references therein. An approximate expression for the molasses

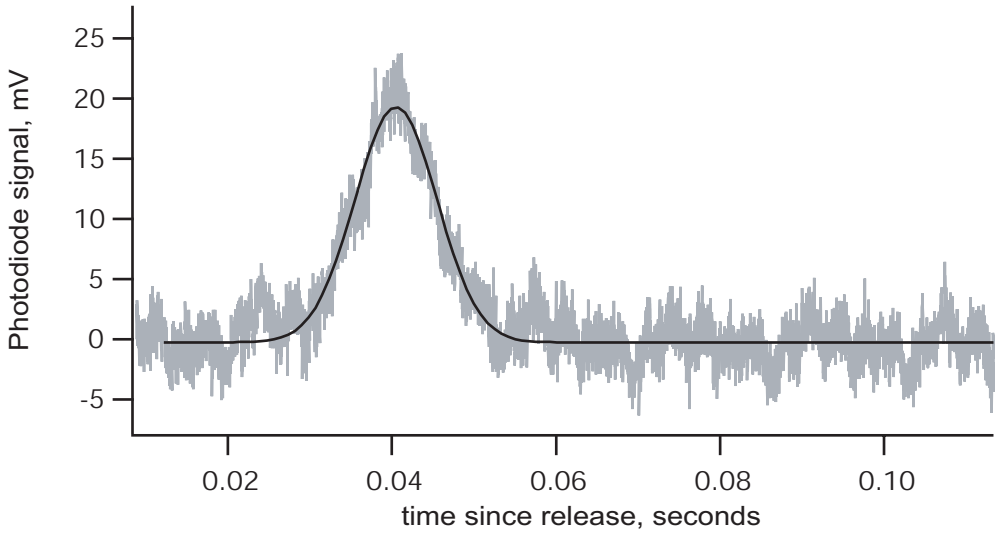

Fig. 2.8.— MOT time-of-flight signal.

temperature was derived by Gertz et al. (Gertz *et al.*, 1993),

$$T = \frac{\hbar\Gamma}{k_B}\left(c_\perp \frac{I}{I_{sat}}\frac{\Gamma}{\Delta}\right) + const. \tag{2.25}$$

where I is the per beam intensity of the trapping laser, Δ is the detuning of the trapping laser, and Γ has been previously defined as the natural linewidth of the trapping transition. The scaling factors of $c_\perp$ and *const* were determined experimentally by Gertz *et al.* to be 0.40 and 5 μK respectively. Our measured temperatures are in good agreement with equation (2.25).

As discussed in the next chapter, the density of atoms in the MOT has proven to be a key factor for successfully loading atoms into the HAT. The bright state density can be calculated by simply dividing the number (derived from fluorescence measurement) by the volume of the MOT cloud. We image the MOT cloud onto a CCD camera with a known magnification and measure a cloud radius of 1 mm. As stated above, we measure the number of atoms in the MOT cloud with fluorescence imaging to be 1.56×10^8 atoms. The resulting density is 3.7×10^{10} atoms/cm^3.

Measuring the dark state density is more difficult because the size is now not well defined. The best method for measuring the density is an absorptive measurement (see for instance (Ketterle *et al.*, 1993)). In this reference the authors probe the dark atom cloud with an off-resonant laser and measure the attenuation of the probe beam given by

$$I(z) = I_0 \times e^{-n\sigma z} \tag{2.26}$$

where σ is the off-resonant absorption cross section. In this paper, they report dark state densities of 1 x 10^{12} atoms/cm^3. An equivalent measurement would be to measure the phase shift induced in a wavefront after passing through the cold atoms. Spatial heterodyne is well suited for this measurement. More details about spatial heterodyne imaging will be given in Chapter 3, but it is important to note that the phase shift is given by

$$\phi = n\sigma l \frac{\Delta}{\Gamma}. \tag{2.27}$$

Both methods measure the column density, nl. To extract the density some estimate of the length along the integrated direction is still needed. With spatial heterodyne imaging we measure the density of atoms in our dark SPOT MOT to be 4×10^{11} atoms/cm^3.

Chapter 3

HAT Loading Results

3.1 Introduction

This chapter continues the discussion of the Holographic Atom Trap. The previous chapter focused on how the HAT works; this chapter focuses on methods for imaging the HAT, the loading procedure for transferring atoms from the MOT to the HAT, and the results obtained after loading the HAT.

Two imaging systems are used to characterize the HAT: Spatial Heterodyne imaging and absorption imaging. Spatial heterodyne, a nondestructive imaging system, was first demonstrated in our lab. Other non-destructive methods have been demonstrated: phase contrast imaging (Andrews *et al.*, 1997), dark-ground imaging (Andrews *et al.*, 1996), and off-resonant defocus-contrast imaging (Turner *et al.*, 2004). I will not be discussing the previously mentioned nondestructive techniques, but a good summary of these is given in (Newell, 2003) and (Ketterle *et al.*, 1999). In general, the benefit of a nondestructive imaging system is that the measured atom cloud is neither destroyed nor altered while taking the image. This allows for multiple pictures of the same cloud to be taken. Nondestructive imaging systems take advantage of the fact that when nonresonant light interacts with atoms, the resulting electric field has both absorption

and phase information. The absorption portion can be made small by detuning the imaging light thus decreasing the scattering cross section. For optically dense samples and for the appropriate detuning, the phase shift can be quite large (≈ 1 radian) and easily detectable. The goal of a nondestructive imaging system is to maximize the signal while scattering a minimum amount of imaging photons. To our knowledge, spatial heterodyne imaging holds the record for being the most nondestructive imaging system ever used to image cold atoms. We acquired an image with S/N = 10 while only scattering 0.0004 photons per atom (Kadlecek *et al.*, 2001). The resolution of our spatial heterodyne imaging system is better than 10 μm. This was demonstrated by resolving the microtraps in the HAT which are spaced 10 μm apart.

The other method of imaging utilized is absorption imaging. In some cases, such as imaging optically thin clouds or for time-of-flight diagnostics, absorption imaging has a superior signal-to-noise ratio. Absorption imaging is implemented by using a resonant probe beam of Gaussian beam waist several times larger than the atom cloud. The atoms cast a "shadow" in the resonant beam. This shadow is imaged on the camera. Our implementation of absorption imaging is calibrated. Assuming a high enough fluence, we can calculate the number of atoms in the sample by simply counting the "missing" photons and dividing by the fluorescence branching ratio. We have also developed a way to artificially increase the signal size with the use of an "Image Booster (IB) beam". A benefit of absorption imaging is improved resolution. By placing an iris in front of the imaging lenses, we have demonstrated a resolution of 5.6 μm.

The work presented in the following chapters makes use of our ability to load many atoms into the HAT. We have developed a loading procedure to optimize the number of atoms loaded into the HAT. Our optimum HAT loading method is similar to other schemes for loading FORTS, (O'Hara *et al.*, 2001b) (Kuppens *et al.*, 2000). After atoms are loaded into the HAT, the atoms collide and thermalize. During the

process the hottest atoms are ejected, leaving an overall cooler sample. This process is called free evaporation. Using the imaging systems discussed in this chapter, we have characterized the HAT during and after free evaporation. I will conclude the chapter by giving some results attained in the HAT after free evaporation. We have found the temperature of atoms in the HAT rapidly decreases to 1/10 the trap depth in less than 100 msec. In our case, the temperature rapidly approaches 60 μK. After free evaporation there are approximately 600,000 atoms in each Talbot fringe. The center microtrap contains 6% of the atoms or approximately 36,000 atoms. The large number of atoms in the tightly confined microtraps yields high initial densities, in excess of 2×10^{14} atoms/cm^3, and high initial phase space densities, approximately 1/200 (Newell *et al.*, 2003). These are excellent conditions for performing an efficient forced evaporation to further increase the phase space density. This will be the topic of the next chapter

3.2 Characterization of the HAT

I will now discuss the tools needed to probe and image the cold atomic samples. Imaging systems can basically be divided into two classes: nondestructive and destructive. Both kinds of imaging systems have been employed in our lab. The nondestructive technique, Spatial Heterodyne, is a novel interferometric method developed in our lab to measure the index of refraction of a cold atom cloud. The destructive technique, absorption imaging, uses the familiar method of measuring the number of photons absorbed from a resonant probe beam. In this section I will discuss these two imaging systems.

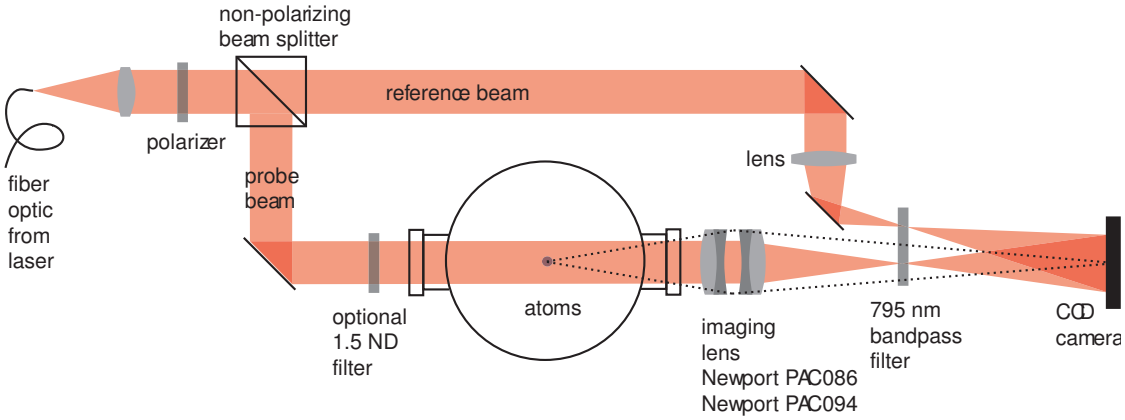

Fig. 3.1.— Spatial Heterodyne (image modified with the permission of R. Newell)

3.2.1 Spatial Heterodyne Imaging

Spatial heterodyne is unique in that it is implemented by interfering two beams on the a CCD camera. The two beams: the probe beam and the reference beam, are derived from the same diode laser. The first beam, the probe beam with intensity I_p, goes through the atoms. As the probe beam travels through the atoms a spatially dependent phase shift, ϕ, is imprinted on the probe beam. The integrated phase shift as seen on the camera is proportional to the the column density,

$$\phi(\mathbf{x}) \ = n\sigma l\frac{\Delta}{\Gamma}. \tag{3.1}$$

After the vacuum chamber a lens images the atoms onto the CCD camera. The probe beam is interfered on the camera with a second beam, a reference beam with intensity I_r, that does not go through the atom cloud. Figure 3.1 shows the optical train.

As long as the two beams have the same radius of curvature at the camera, the resulting interference fringes on the camera will be a series of straight lines. At the position of the image of the atom cloud, the straight fringes will be bent. The intensity

pattern as seen by the camera is:

$$I(\mathbf{x}) = I_r + I_p + 2\sqrt{I_r I_p}\ cos\left(\delta + 2\pi\theta\hat{k_\perp} \times \frac{\mathbf{x}}{\lambda} - \phi(\mathbf{x})\right) \tag{3.2}$$

where $\hat{k_\perp}$ is a unit vector pointing along the direction of the component of the reference wave vector $\mathbf{k}$ perpendicular to the direction of the probe beam. The first two terms represent the sum of the intensities of the individual lasers. The third term is the interference term; information about the atom cloud is contained in $\phi(\mathbf{x})$.

Two important factors contribute to good inteference fringes: the beams must have the same polarization and the path length difference for the two beams must be less than the coherence length of the laser. To address the first concern, a polarizer was inserted in the optical train prior to the separation of the two beams. The separation is done with a 50/50 nonpolarizng beam splitter cube. Typically for diode lasers the issue of coherence length is not a concern as typical coherence lengths are on the order of 1 km, a distance much greater than the path length difference. To avoid aliasing effects from the camera, the angle of interference between the two beams is purposely tilted an angle θ.

There are two possible modes for which spatial heterodyne can be implemented: $\theta \ll \delta/\lambda$ (parallel mode) and $\theta \gg \delta/\lambda$ (tilted mode), where δ is the resolution needed for the image. Parallel mode was not implemented in our lab for technical reasons and will not be discussed here. For a full description see references [Kadlecek et al., 2001] and [Newell, 2003].

The information about the atoms is contained in the factor $\phi(\mathbf{x})$. The method to extract this information proceeds in a manner analogous to lock-in detection and cartooned in figure 3.2. First we acquire an image of the interference pattern between the probe and reference beams (figure 3.2 a). Next, we take the 2-dimensional Fourier transform (figure 3.2 b). Examination of the FFT shows a large amount of information

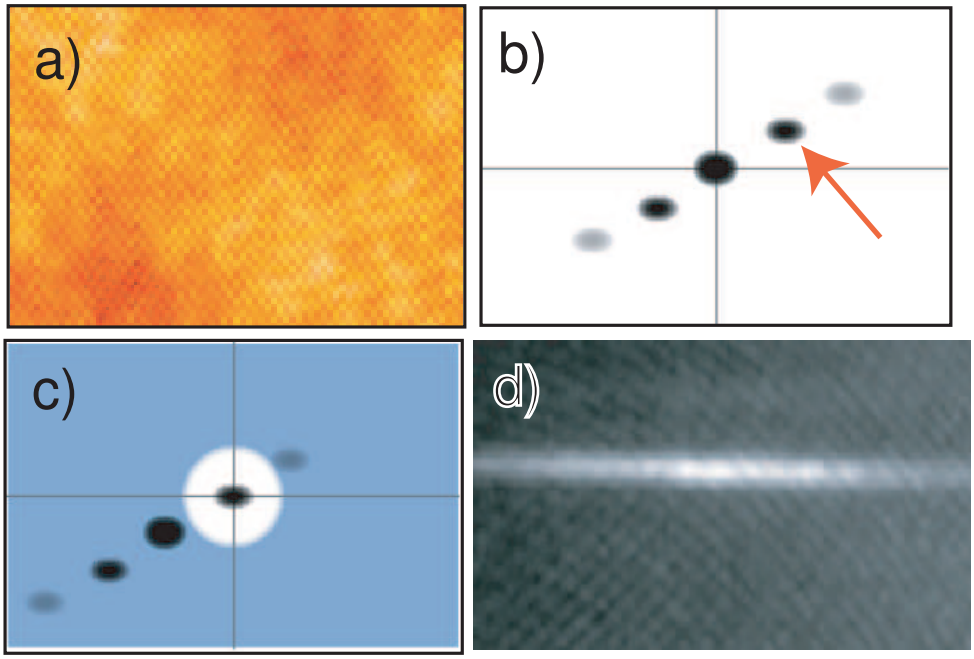

Fig. 3.2.— Processing of spatial heterodyne images. a) The interference pattern from the two beams. b) A cartoon of a typical FFT. The arrow points to the fringe pattern information. c) Filtering and shifting in the Fourier Plane. d) Inverse Fourier Transform to extract the phase information. In this image, bright pixels represent the largest phase shifts.

a low spatial frequency and information at the spatial frequency of the fringe pattern. The information about the atoms is at the frequency of the fringes. From the FFT the spatial frequency of the fringes, k_x and k_y, can be determined. Using these values we shift the fringe frequency to zero-spatial frequency. We then apply a low-pass-filter, typically Gaussian, about zero frequency (figure 3.2 c). Then we take the inverse Fourier transform; the phase is then calculated by $\phi(\mathbf{x}) = \tan^{-1} Im(I(x,y)/Re(I(x,y))$.

This represents the basic idea, but to actually get a map of phase shift as a function of frequency, a series of images must be taken and analyzed to account for the background and technical noise in the camera. The five picture sequence is acquired as follows. Picture 1 contains the MOT cloud, the reference beam, and the (attenuated) probe beam. Prior to picture 2 the MOT is turned off. Picture 2 contains the reference and probe beam. Picture 3 is just the reference beam. Picture 4 is the probe beam. Lastly, picture 5 is with all light blocked to capture the background. Pictures 3,4, and 5 are subtracted from pictures 1 and 2. This leaves only the interference term in equation (3.2). Pictures 1 and 2 are independently analyzed as detailed above. After processing, picture 2 is subtracted from picture 1. Figure 3.2 d) shows the final product, phase shift as a function of position for a dark-sheet trap formed with a 59 μm wire imaged in the hyperfine repumping beam.

In tilt mode the resolution of imaging system is set by the fringe spacing. As with all lock-in detection schemes, modulation must be applied at a higher frequency than the frequency of the signal. The same is true with spatial heterodyne: the fringe spatial frequency must be higher than the spatial frequencies we are trying to detect. On the other hand, it is necessary to have several pixels per fringe period to avoid aliasing problems. We have found that a good compromise is to have 4-5 pixels per fringe period. Given this constraint, we were still able to resolve 10 μm using a magnification factor of 4.8. Using spatial heterodyne we have been able to resolve the microtrap

in the HAT as shown in figure 3.3. Though not discussed here, diffraction limited performance can be achieved in parallel mode.

The implementation of spatial heterodyne requires a few primary components: the imaging laser, the optical train, and the detector. These are shown in figure 3.1. The imaging light is generated from a homemade external cavity diode laser in the Littrow configuration. The laser is locked to the D1 line ${}^2S_{1/2}$ $F = 1$ to ${}^2P_{1/2}$ $F' = 2$ in Rb-87 using standard saturated absorption spectroscopy. We use the D1 line so that a band pass filter can filter the D2 MOT fluorescence before the CCD camera. The detuning and shuttering is done with two Accousto-Optic Modulators (AOM). The first AOM is driven at a frequency δ_1; the second AO is driven at δ_2. The detuning from resonance is given by $\Delta = \delta_1 - \delta_2$. The laser is then coupled into a single-mode fiber for transport to the trapping chamber. The light coming out of the single-mode fiber is collimated at a Gaussian beam waist of 2.64 mm.

The atom cloud is imaged onto the CCD camera with a pair of Achromatic doublet lenses, f=150 mm (Newport PAC086) and f=750 mm (Newport PAC094). This set of lenses was chosen to minimize aberrations. With an 15 mm diameter iris in front of the lens pair, the aberration limited resolution is 5 μm. This will further be discussed in Chapter 5. The magnification of the imaging system is 4.8.

The CCD camera is a Hamamatsu ORCA-ER. The ORCA-ER's CCD chip has 1344 x 1024 6.45 μm square pixels. There are two modes of operation which effect the quantum efficiency of the camera. In "high" light mode the quantum efficiency, η, at 795 nm is 16%; in "low" light mode η is 33%. Most spatial heterodyne and absorption pictures were taken in the "high" light mode. Using the quantum efficiency and the conversion from camera counts to photoelectrons, 4.6 counts per photoelectron, the number of incident photons can be determined. The ORCA-ER is controlled largely with Labview IMAQ software, and the images are analyzed with a Labview program.

Figure 3.3 - Spatial Heterodyne image of the HAT

Regardless of the implemented mode, spatial heterodyne has a number of advantages over other nondestructive imaging systems. First, spurious fringes from optical elements can be filtered out. Typically unwanted fringes have a definite spatial frequency. With clever choice of filtering in the fourier plane, these fringes can be eliminated. Second, there is no need for a specially fabricated phase plate as necessary in phase contrast imaging (Andrews *et al.*, 1997). All optics used in the implementation of this method were standard-off-the-shelf optics. Third, spatial heterodyne can work over a large range of spatial scales. In phase contrast (Andrews *et al.*, 1997), the upper limit on the spatial scale that can be imaged is the size of the phase plate. In spatial heterodyne the upper limit is the size of the CCD chip. And finally, the probe beam can be attenuated relative to the reference beam. This means that the camera will see enough light from the reference beam to overcome technical noises (such as read noise and dark current) but this light will not destruct the atomic sample. A complete discussion of signal-to-noise and the non-destructive nature of spatial heterodyne in Appendix F, but I will summarize the results here. The real figure of merit for spatial heterodyne is the signal-to-noise per absorbed probe photon which is given by:

$$\frac{S/N}{A} = \frac{2\phi\sqrt{\eta N_p}}{\alpha N_p} \tag{3.3}$$

where η is the quantum efficiency of the camera and α is the absorption coefficient. This equation assumes that the number of photons in the probe beam, N_p is much less than the number of photons in the reference beam, N_r. It also assumes that N_r can be sufficiently large that technical noise from the camera can be neglected. The dominate source of noise is laser shot noise. Using the relation that $\phi/\alpha \approx \Delta/\Gamma$ gives

$$\frac{S/N}{A} \approx 2\frac{\Delta}{\Gamma}\sqrt{\frac{\eta}{N_p}}. \tag{3.4}$$

The ideal conditions to achieve high signal to noise ratio with the fewest number of photons scattered is to go to high detuning and low probe fluence. At $\delta = 11\Gamma$ and a

Fig. 3.4.— A nondestructive spatial heterodyne image of a MOT.

probe fluence of 61 pJ/cm^2, we were able to use spatial heterodyne imaging to image a MOT cloud by scattering only 0.0004 photons per atom. This is the record for the most nondestructive image taken of cold atoms. The image is shown is figure 3.4.

3.2.2 Absorption

I this section I will discuss the other destructive imaging method used in this experiment, absorption imaging. While nondestructive imaging is advantageous for preservation of the sample being imaged, it is difficult to do with optically thin samples. In these cases absorption imaging is a better choice.

In some cases, such as imaging optically thin clouds or for time-of-flight diagnostics, absorption imaging has a superior signal-to-noise ratio. Absorption is implemented by using a resonant probe beam of Gaussian beam waist several times larger than the atom cloud. The atoms cast a "shadow" in the resonant beam. This shadow is imaged on the camera. The attenuation of the probe beam after passing through the atom

cloud is related to the column density of the cloud by

$$I(x,y) = I_0(x,y)e^{-n(x,y)\sigma_0 l} \tag{3.5}$$

where σ_0 is the resonant absorption cross section. Assuming a narrow probe laser we can express the absorption cross section as $\sigma_0 = \frac{3\lambda^2}{2\pi}$.

Our apparatus for absorption imaging is easily modified from spatial heterodyne: block the reference beam and remove the 795 nm bandpass filter. Typically the imaging laser is shifted to be on resonance with the $^2S_{1/2}$ $F = 1$ to $^2P_{1/2}$ $F' = 2$ transition. A second laser, the IB beam, can be added to increase signal size as discussed below.

Producing an absorption image requires a series of three pictures. A 150 μsec pulse of resonant imaging light is sent through the atoms. The imaging transition has a fluorescence branching ratio of 2; if the fluence is sufficient then on average each atom will scatter two photons from the imaging laser before being optically pumped into the F=2 hyperfine state. Once in F=2, the atoms no longer interact with the imaging laser. After waiting 1 second for the once-trapped atoms to disperse, a second picture is taken of just the probe beam. Finally, the probe beam is blocked and background picture is taken. The background picture and the probe laser are subtracted from first picture.

Our implementation of absorption imaging is calibrated. Typically, absorption imaging is done on a cycling transition making it difficult to accurately account for the number of photons absorbed per atom. By using a non-cycling transition, such as the $^2S_{1/2}$ $F = 1$ to $^2P_{1/2}$ $F' = 2$ transition, we can accurately predict the number of photons absorbed by each atom and thus can calculate the number of atoms. This is done in the following way. A region of interest containing the cold atoms is identified. The processed absorption image is fit to a Gaussian in case a residual background remains. If present, the background is subtracted off, setting the pixels with no atom

information to zero. Next the ROI pixel values (in counts) are summed. The number of counts is converted to photoelectrons by using the ORCA-ER conversion of 4.6 photoelectrons/count. The quantum efficiency of the camera relates the number of registered photoelectrons to incident photons. Using this algorithm we can "count up" the number of missing photons. Assuming that on average the atoms scatter two photons, we divide the number of missing photons by two to measure the number of atoms.

The S/N ratio for our implementation of absorption imaging is

$$\frac{S}{N} = \frac{2\eta N_A}{\sqrt{\eta N_0}} = \sqrt{\eta N_0}\frac{2N_A}{N_0} \tag{3.6}$$

where N_A is the number of atoms per pixel and N_0 is the number of probe photons per pixel. This equation assumes that the sample is optically thick, and the primary source of noise is shot noise. In this case the S/N decreases for increased number of incident photons. Therefore it is desired to use the minimum amount of photons to increase S/N, but enough photons must be present to assure the calibration of our imaging system. We have several "tricks" to increase the S/N ratio. One such method is binning. The pixels can be binned 2x2, 4x4, or 8x8. Binning is advantageous when trying to defeat the read noise of the camera. This works because binning adds the signal but not the read noise. The disadvantage is that the resolution decreases at higher pixel binning. For time-of-flight images when resolution is not important, binning has proven to be very useful.

In the case of small signals or during time-of-flight measurements, two photons per atom might not be enough signal to attain sufficient S/N. A second beam, the "Image Booster Beam (IB Beam)" is turned on in concert with the imaging pulse. The IB beam is resonant to the $^2S_{1/2}$ $F = 2$ to $^2P_{3/2}$ $F' = 2$ transition. This transition also has a fluorescence branching ratio of 2; on average after scattering two photons

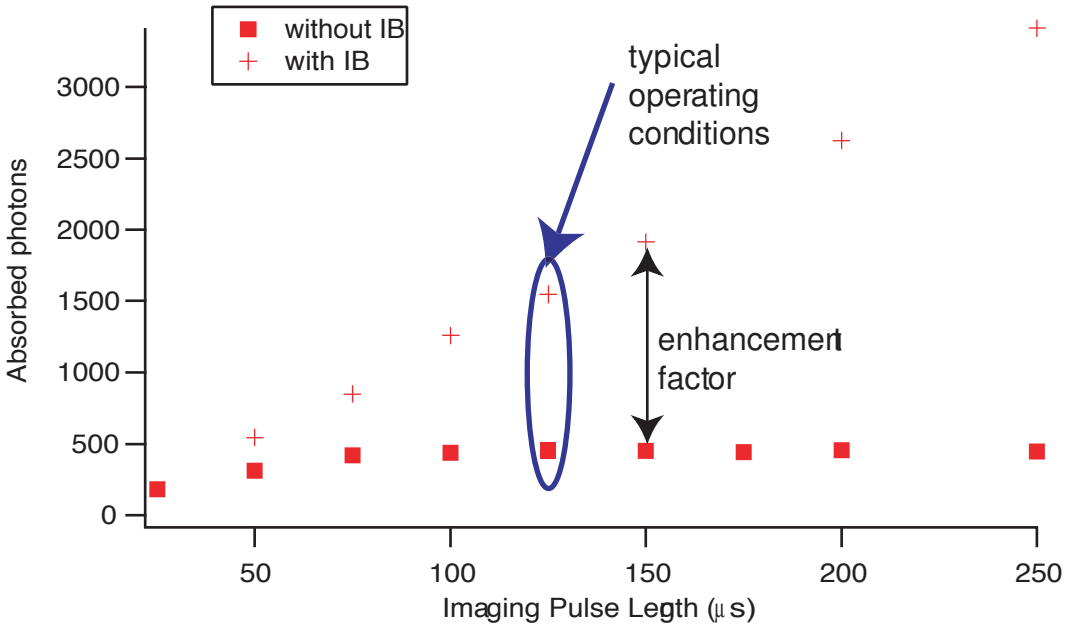

Fig. 3.5.— Enhancement of the absorption signal due to the IB Beam.

from the IB beam, the atoms are now back in F=1 and can rescatter imaging photons. Using this methods we can enhance the signal by a factor of 10-15 and can image approximately 10,000 atoms with a $S/N > 10$. This effect is shown in figure 3.5. The x-axis is proportional to the number of incident photons. In the presence of the IB Beam the signal growns linearly. Without the IB beam the signal saturates after the atoms have scattered two photons and have been optically pumped into a different hyperfine state. The arrow designates the typical operating conditions. In the absence of the IB beam we want to image with enough light so to insure that the atoms are scattering the necessary 2 photons per atom. We do not want, however, to use too much light as the shot noise of the laser will begin to degrade the S/N. As seen in figure 3.5, when the IB beam is used, the signal is enhanced.

As will be discussed in chapter 5 typically the atom samples produced in the HAT are optically dense. One disadvantage of absorption is that it can be over-sensitive and

can cause "black outs", or in other words, the signal from an optically dense cloud can easily saturate. This limits the amount of spatial information that can be extracted from the image. Detuning the imaging laser several linewidths has proven to be an effective method for attaining images which require spatial sensitivity.

3.3 Loading Procedure

We will now discuss the procedure for transferring atoms from the MOT to the HAT. In steady state we prepare a MOT with approximately 70% of the atoms in F=1. This is accomplished by the physical dark spot (see Chapter 2) and by attenuating the repumping beam to approximately 3 mW. We also add a depumper tuned +54 MHz from the F=2 to F$'$ = 2 transition. Typically we use 2-3 mW of the depumper, but the final powers of both the depumper and repumper are adjusted during the daily optimization process. By measuring the rapid increase in fluorescence after abruptly removing the dark spot, we can estimate there to be approximately 9×10^7 atoms in F=1.

We begin the loading procedure by first reducing the MOT beams' intensity by a factor of 4. This is achieved by using the intensity stabilized double-passed AOM as discussed in Chapter 2. After 50 ms we then increase the current in the MOT coils by a factor to 2 which increases the magnetic field gradient by a factor of 2. These two steps are part of a well-developed method for compressing a dark SPOT MOT (Petrich,*et al.* 1994), . After these two steps we have used spatial heterodyne imaging to measure the density of atoms in F=1 to be typically 4.7 x 10^{11} atoms/cm^3. Reducing the trapping intensity also reduces the molasses temperature from 188 μK to 47 μK. At this point we turn on the YAG laser. Figure 3.6 is a plot of the number of atoms loaded into the HAT as a function of loading time. We have found that the number of atoms loaded into the HAT is time dependent with a maximum number loaded in for loading times

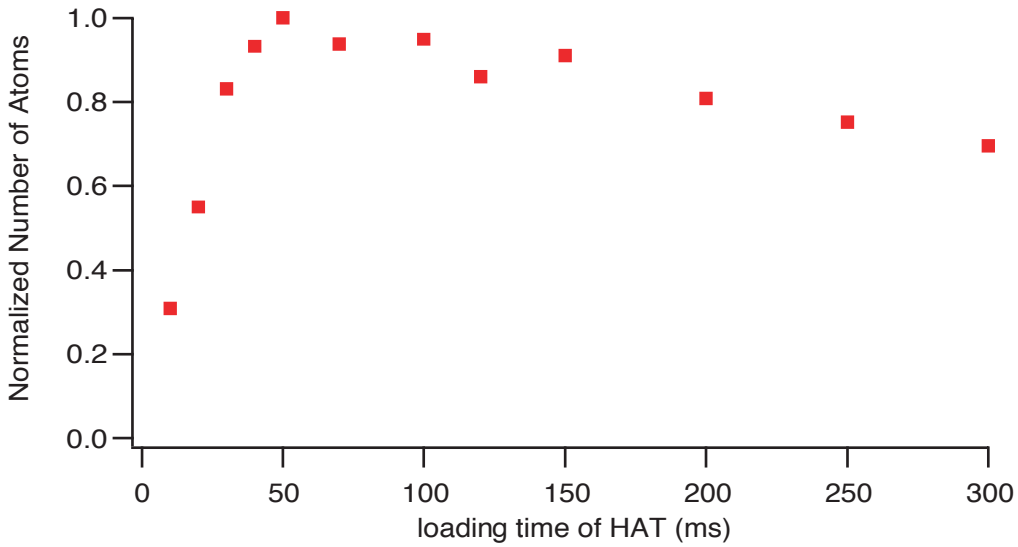

Fig. 3.6.— Number of atoms per Talbot fringe as a function of HAT loading time.

of 50 - 70 ms.

The electric field from the YAG cannot be neglected when considering the effect the YAG has on the MOT atoms. The AC stark shifts induced by the YAG are large. The relevant polarizabilities (Newell, 2003) are $\alpha(5\mathrm{S}_{1/2}) = 98.8$ Å^3 and $\alpha(5\mathrm{P}_{3/2}) =$ -271.0 Å^3. In the presence of the YAG the $5\mathrm{S}_{1/2}$ to $5\mathrm{P}_{3/2}$ frequency shifts are given by $\Delta\nu = -(\alpha_{5S_{1/2}} - \alpha_{5P_{3/2}})I/\hbar c$. In terms of the trap depth, $U_{max} = -2\pi\alpha_0\left(5S_{1/2}\right)I/c$, the frequency shift becomes

$$\frac{\Delta\nu_{5P_{3/2}\rightarrow 5S_{1/2}}}{U_{max}} = \frac{\alpha\left(5P_{3/2}\right) - \alpha\left(5S_{1/2}\right)}{h\,\alpha\left(5S_{1/2}\right)} \tag{3.7}$$

knowing that h = 48 μK/MHz, we can rewrite this in the convenient form of

$$\Delta\nu_{5P_{3/2}\rightarrow 5S_{1/2}} = -7.8\,MHz \times \frac{U_{max}}{100\ \mu K} = -1.3\Gamma \times \frac{U_{max}}{100\ \mu K}. \tag{3.8}$$

The total frequency shift is 7.8Γ, the $5\mathrm{S}_{1/2}$ is shifted down by 2.1Γ and the $5\mathrm{P}_{3/2}$ is shifted up by 5.7Γ.

While these frequency shifts are large, they work in our favor: the MOT and repumper lasers are shifted further from resonance, while the depumper is shifted closer into resonance. This cools the atoms and decreases the excited state fraction to only a percent so that now almost all of the atoms are in F=1. To further decrease the molasses temperature, we detune the MOT lasers from -18 MHz to -40 MHz. Considering the AC stark shifts, the final molasses temperature at this point is only a few μK. After 50 ms with the YAG on, the magnetic field is quickly turned off. 5 ms later all other lasers, the repumper, depumper, and Ti:Sapph, are extinguished.

The Duke group (O'Hara *et al.*, 2001b) uses the Fokker-Planck equations to model the loading dynamics in their CO_2 trap. A major result of this paper was the benefit of having a trap depth much greater than the molasses temperature. Their model shows rapid growth in the number trapped in the FORT at t=0 as the ratio of the trap depth to MOT temperature increases. Furthermore, the authors see the same FORT loading time dependences as discussed above. They show that the number loaded into the FORT increases rapidly at first but slows as the loading time approaches 20 ms. Similarly the Colorado group (Kuppens *et al.*, 2000) showed that the number of atoms in their FORT increases until the loading time approaches 100 ms, then slowly the number decays. Of course, the actual ideal loading time with vary depending on the specific trap conditions.

The final step in the loading procedure is a 20 ms pulse from the "loading beam" tuned to the $^2S_{1/2}$ $F = 2$ to $^2P_{3/2}$ $F' = 2$ (depumping) transition. This last step serves to optically pump any remaining F=2 atoms into F=1. Once all the lasers are turned off, the atoms now undergo rapid free evaporation in which atoms in the trap collide and in the process the hottest atoms are ejected from the trap. Free evaporation is an efficient process until the temperature of the atoms reaches 1/10 the well depth. At this point the temperature stagnates. Chapter 4 will be devoted to more of the

mechanics of evaporation.

Loading atoms into any FORT is really an art form. Besides following the procedure laid out above, there are three key factors to good HAT loading: high MOT cloud density, proper excited state fraction of the MOT, and positioning of the HAT relative to the magnetic field zero in the MOT cloud. When aligning the retro-reflections in the MOT it is generally better to sacrifice number for a smaller, denser MOT cloud. The second key factor, excited state fraction, is generally determined by trial and error but every effort should be made to make sure that all of the atoms are in F=1 by the end of the loading procedure. The final factor regarding the position of the HAT relative to the MOT was found by trial and error. Typically we try to position the HAT so that it coincides with the magnetic field zero of the MOT. Generally the magnetic field zero is at the center of the MOT. Furthermore, we can make a guess where the magnetic field zero is by watching the MOT load after power cycling the magnetic field. The spot where the atoms first collect is likely the magnetic field zero. But ultimately, locating the position where the HAT best loads is by trial-and-error. This result is somewhat contradictory to the findings in reference (Kuppens *et al.*, 2000) which reported that the FORT loads best when offset from the magnetic field zero.

3.4 Results after Loading

In this section I will give some typical results that we have achieved in the HAT. Spatial heterodyne imaging or absorption imaging were used to gather these results. I will limit this discussion to the results attained after loading and free evaporation. Chapter 4 will discuss what happens after that.

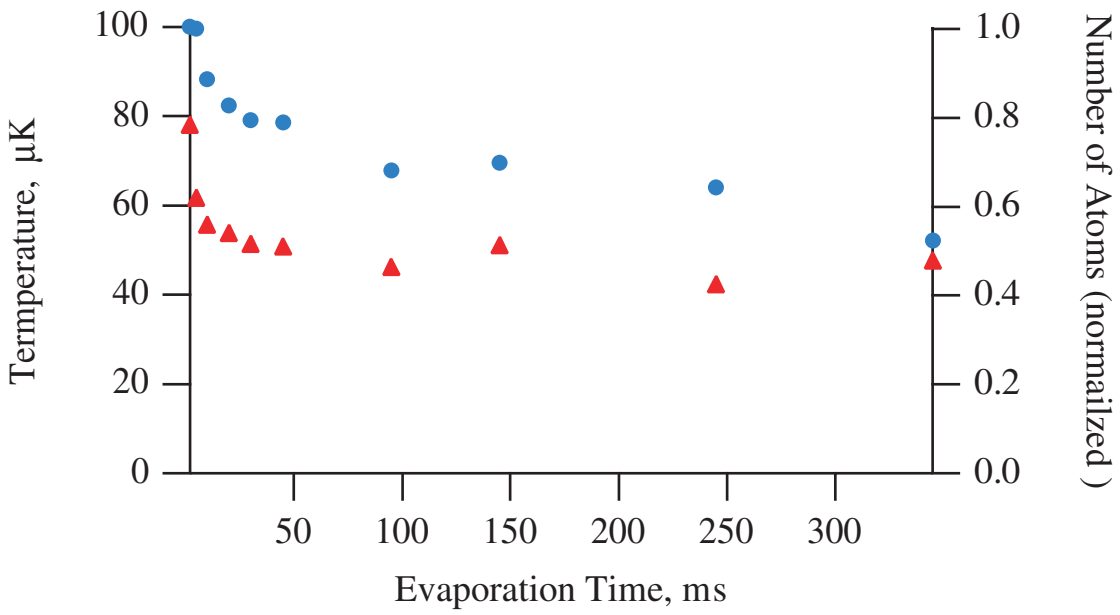

Fig. 3.7.— Left axis: Temperature (triangles) as a function of free evaporation time. Right: Normalized number of atoms per Talbot fringe (circles) as a function of free evaporation time.

3.4.1 Number per Talbot Fringe

After loading and during free evaporation, hot atoms leave the trap. In this case atom loss is a cooling mechanism. Using the calibrated absorption method described earlier in this chapter we can measure the number of atoms per Talbot fringe as a function of free evaporation time as shown in figure 3.7. The atom loss slows as free evaporation becomes less efficient. Typically after 40 ms of free evaporation we have 600,000 atoms in the most populated Talbot fringe.

3.4.2 Center Well Fraction

Our understanding is that during the loading process the atoms within a Talbot fringe redistribute themselves amongst the microtraps. The distribution of atoms

is proportional to $e^{-U/T}$. Assuming that all the microtraps are in thermal equilibrium, atoms are preferentially loaded into the center well. Once loading is finished the distribution remains fixed during the free evaporation process.

We can measure the distribution by taking absorption images of the microtraps then fitting the distribution to a series of Gaussian radii as shown in figure 3.8. Using the heights of the Gaussian fits, we can determine the center well fraction. We divide the height of the center peak by the sum of the heights of all the peaks. This is the fraction of atoms in the center well, but only in one dimension. We assume that the y-distribution (into the page) is the same as the x-distribution, and so the fraction in the center well is the square of the fraction in the x-direction.

Typically atoms in the Talbot fringe occupy 25 microtraps. We see center well fractions of approximately 4-6% after loading. From this we can determine the number of atoms in the center microtrap to be 36,000.

We have demonstrated a method, "shake-n-bake", to increase the center well fraction. Essentially, we purposely intensity modulate the trap at a frequency of $2\nu_i$ where ν_i is the oscillation frequency an outer well. This heats and ejects atoms in the outer well but not atoms in the center well. This can be seen in figure 2.4. If the laser is intensity modulated at a frequency less than the $2\nu_0$ (where ν_0 corresponds to the center trap oscillation frequency) there will be atom loss from the outer microtraps in the Talbot fringe, but atoms will not be lost from the center microtrap. With this method we have been able to increase the center well fraction by a factor of 2.7 compared to the initial conditions.

3.4.3 Lifetime

After free evaporation and in the absence of any heating mechanisms or laser fields, the trap loss is predominately collisions with background atoms; the time de-

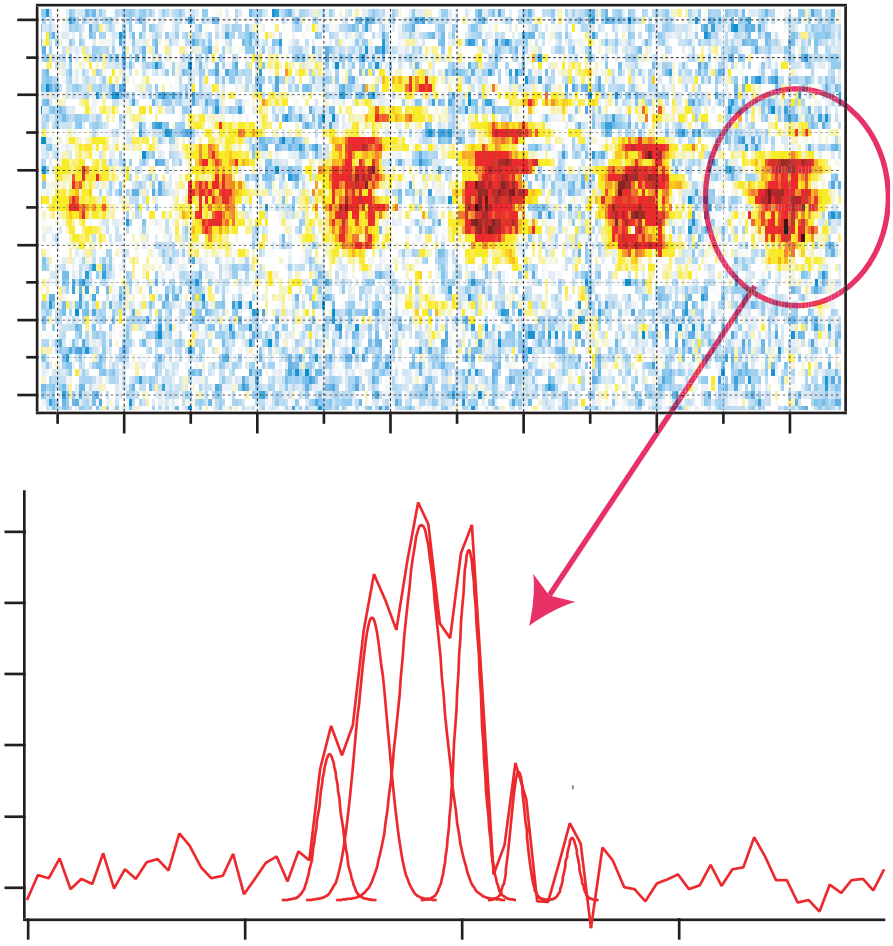

Fig. 3.8.— Typical absorption image (top) and distribution (bottom) of atoms in the microtraps.

pendence is well explained by an exponential. By fitting the number of atoms in the HAT as a function of time to an exponential, a lifetime can be extracted. The lifetime is an important number because it sets the time scale for forced evaporation. This too will be discussed in the chapter on evaporation, but if the evaporation procedure takes longer than the lifetime it will become very inefficient. Typically we measure HAT lifetimes of 3 seconds.

3.4.4 Temperature

We measure the temperature of atoms in the HAT with a time-of-flight(TOF) technique. The YAG is quickly extinguished and atoms ballistically expand at a rate proportional to the velocity distribution within the HAT prior to the YAG turn off. We image the expanding cloud at several expansion times, fit the cloud to a Gaussian radius, then plot the expanding radii as a function of time. Assuming a Boltzman velocity distribution, the Gaussian radii as a function of time can be described by the quadrature sum of the initial radius and the distance traveled

$$\sigma(t) = \sqrt{\sigma_0^2 + v_T^2 t^2}. \tag{3.9}$$

From the fit the velocity can be extracted. The temperature can be calculated by the standard method of $T = (1/2)mv_T^2$ which can be written in the convenient form of

$$T = 0.52\mu K + \left(\frac{v}{1cm/s}\right)^2. \tag{3.10}$$

It is difficult to measure the temperature of atoms in the trap immediately after loading because the untrapped MOT atoms have not completely left. After about 10 ms after loading, a TOF is possible. Figure 3.7 shows the temperature as a function of time during free evaporation. When the HAT is operated at U_{max}, the measured temperature after free evaporation is 60 μK which agrees well with the predication that free evaporation should cease when T = U/10.

Though free evaporation seems to be the dominant cooling mechanism, we made many attempts to laser cool the atoms in the HAT. A summary of these attempts is given in [Newell, 2003].

Chapter 4

Evaporation

4.1 Introduction

On the surface, evaporation is a simple idea: allow a few hot atoms to collide and leave the trap, resulting in an overall cooler sample. While in practice it is a bit more difficult, our simple picture serves as a good model for what is happening.

The ultimate goal of evaporation is to decrease the temperature of the atoms in such a way that the phase space density increases. Evaporation, in this context, was first preformed in magnetic traps and led to the observation of the first Bose-Einstein Condensate (Anderson *et al.*,1995) (Davis *etal.*, 1995). The prospects of evaporating to quantum degeneracy in an optical trap were good based on the high phase space densities and atomic densities with which atoms are loaded and the long storage times seen in some FORTs. With the lessons learned from magnetic traps, the Georgia Tech. group preformed optical evaporation of Rubidium in a crossed dipole optical trap (Barrett *et al.*, 2001) to achieve the first all optically produced Bose Condensation. Optical traps have a number of advantages over magnetic traps including a more efficient evaporation process and the ability to evaporate multiple spin components. This has allowed some interesting studies of the interaction of BEC's of different spinor components (Bar-

rett *et al.*, 2001). Furthermore, the high collision rates typical of optical traps have allowed BECs to be produced in a few seconds, much faster than in magnetic traps. Recently, optical traps have been used to produce the first Cesium condensate (Weber *et al.*, 2003) and to produce the first evidence of superfluidity in a Fermi degenerate gas (Kinast*et al.*, 2004).

The list of uses for evaporation is not limited to Bose Einstein Condensation. In Chapter 5 I will discuss using evaporation as a integral part for the formation of high density mesoscopic atom clouds. These clouds are of interest in a variety of experiments and are well tailored for studying the interactions of highly excited ultracold Rydberg atoms.

We have performed optical evaporation in the HAT and have used it for production of high phase space density clouds. We have already discussed the high initial densities attainable in the HAT. These high densities cause high collision rates which allow for rapid evaporation. Initial collision rates are in excess of 20,000/sec. For comparison, initial densities in magnetic traps are typically $1 \times 10^{11}/\text{cm}^3$, resulting in initial elastic collision rates of 12/sec. A vital tool in the production of these clouds is a simple model which describes the dynamics of evaporation and predicts the optimum conditions to achieve high phase space density. Using this model as a guide we have generated clouds with a phase space density of 1.1, extremely close to quantum degeneracy. In this chapter I will discuss in detail this model and give results typical when using the model to produce high phase space densities. In the next chapter I will discuss evaporation's use in producing extremely high density mesoscopic clouds.

4.2 Theory

I will discuss evaporation in two parts: free evaporation and forced evaporation. Forced evaporation in an optical trap is slightly different than its magnetic counterpart.

These differences will be briefly discussed.

4.2.1 Free Evaporation

After the atoms have been loaded into the HAT they collide with other trapped atoms. If the energy of the colliding pair is high enough, one of the atoms in the pair will be given enough energy to be ejected from the trap. Initally, the pair has a large amount of energy and there is a high probability that one of the atoms will be ejected during the collision. After ejecting the hottest of the atoms, the remaining atoms in the trap are at an overall colder temperature. This process is called free evaporation. It continues until the temperature becomes low enough that few colliding pairs of atoms have enough energy to be ejected. This usually occurs when the ratio of the trap depth to the temperature of atoms in the trap approaches 10. In other words, the temperature in the trap will go down with time but will stagnate at 1/10 the trap depth. Graphs of temperature and number of atoms as a function of evaporation time are shown in figure 3.7. As I will show in 4.3.1, during free evaporation both the density and the phase space density increase.

4.2.2 Optical Forced Evaporation

The point of forced evaporation is to restore the conditions of $T > U/10$ so that free evaporation can be rejuvenated. In magnetic evaporation this is done with the "RF knife": an RF probe which causes atoms near the upper edges of the trap to make transitions to untrapped magnetic sublevels. By changing the frequency of the RF knife, deeper cuts are made in the potential. In optical evaporation this is done by lowering the trap depth. In either case, the effect is a truncation of energies that can exist in the trap.

The major difference between optical evaporation and magnetic evaporation is

in regards to what happens to the spring constant of the trap during evaporation. A cartoon in figure 4.1 illustrates this difference. In the magnetic case the evaporation occurs from the top down, thus keeping the spring constant at the bottom of the well constant. It is then possible to increase the density as a function of time and a condition called "run away" evaporation is achieved. In optical evaporation, however, the trap depth is lowered; lowering the well depth decreases the spring constant and thus decreases the density. For this reason runaway evaporation is not possible in an optical trap. The saving grace of optical evaporation is that the starting phase space densities and atomic densities are orders of magnitude larger in optical traps than magnetic traps, allowing these barriers to be overcome.

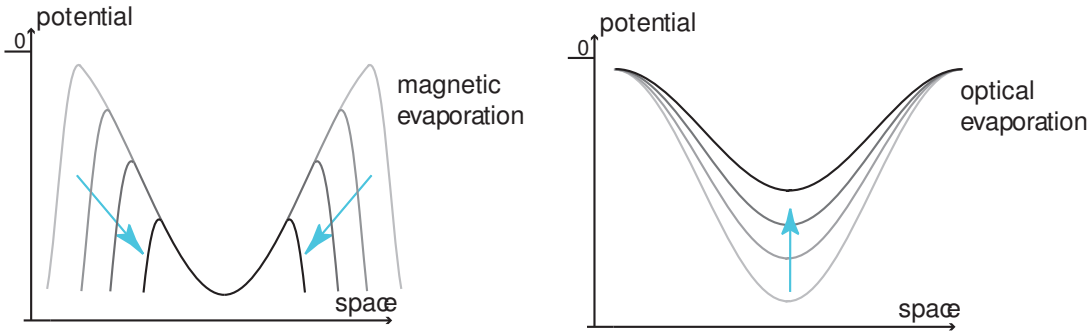

Fig. 4.1.— Left: Evaporation from a magnetic trap. Right: Evaporation from an optical Trap. (image used with the permission of R. Newell)

4.3 Model of Forced Evaporation

In this section I will describe our model for evaporation. There are two ways to model evaporation. The first method (Davis *et al.*, 1995b) treats evaporation as a sequence of two discrete steps: a truncation of the trap depth followed by a rethermalization process. In other words, in the first step the potential is truncated (experimentally

this is done with the RF knife). After the truncation, the second step begins which is the rethermalization of the atoms in the truncated potential. The rethermalization step cannot begin until the truncation step been completed. The two steps are repeated cyclically, and a set of simple scaling laws are used to calculate thermodynamic values (such as the number, phase space density, and temperature) only at the end of each truncation and rethermalization step. The model of Davis *et al.* pertained to evaporation in a magnetic trap; to our knowledge this treatment has never been extended to describe optical evaporation.

In contrast, O'Hara *et al.* (O'Hara *et al.*, 2001) models evaporation as a continuous process. This work uses the s-wave Boltzman transport equation to derive a set of time dependent, analytical functions to describe the evolution of the phase space density, temperature, etc. With these equations the thermodynamic values are known at all times, not just at the "end" of a step.

Even though the treatment of O'Hara *et al.* is more analytical and has more formalism, we have created a model for evaporation that is similar to (Davis *et al.*, 1995b) in that we treat evaporation as a sequence two discrete steps, but we have extended this model for the case of evaporation from an optical trap. This method is a very straightforward approach, and we have found the scaling law approach to be a useful intuitive tool. Below I will derive two sets of scaling laws: one set expresses all the pertinent thermodynamic variables for the rethemalization process in terms of the fractional energy and number remaining in the trap; the second set of scaling laws will describe the change in the thermodynamic variables which results from adiabatically lowering the potential. Like the Davis's *et al.* model, the two steps will be iterated, and the second step cannot begin until the first step has been completed. At the end of each step, the values of the thermodynamic variable will be recalculated. Lastly, I will discuss adaptations made to the model to account for losses due to background

collisions. In future chapters this model will be revisited and further adaptations will be discussed.

4.3.1 Scaling Laws for Rethermalization

We want to express all thermodynamic variables in terms of two parameters: ϵ, the fractional amount of energy retained after a cut, and ν, the remaining fraction of atoms. More explicitly

$$\nu = \frac{N'}{N} \tag{4.1}$$

and

$$\epsilon = \frac{E'}{E} \tag{4.2}$$

where the primed denotes the newly recalculated value, and the unprimed denotes the previous value. We also introduce the cut parameter, η which is

$$\eta = \frac{U}{T}. \tag{4.3}$$

We want to express ν and ϵ in terms of η. To determine the fraction of atoms that remain in the trap, we find the number of atoms, N$'$ that will remain in the trap after the cut and divide this by the total number of atoms

$$\nu(\eta) = \frac{N'}{N} = \frac{\int_0^{\eta kT} g(E) e^{E/kT} dE}{\int_0^{\infty} g(E) e^{E/kT} dE}. \tag{4.4}$$

Similarly we find the fractional energy retained by integrating the density of states over the truncated region divided by the total energy

$$\epsilon(\eta) = \frac{E'}{E} = \frac{\int_0^{\eta kT} g(E) E e^{E/kT} dE}{\int_0^{\infty} g(E) E e^{E/kT} dE}. \tag{4.5}$$

The density of states for a three dimensional harmonic oscillator is given by

$$g(E) = \frac{E^2}{2h^3 \bar{\nu}^3} \tag{4.6}$$

where here I am using $\bar{\nu}$ to refer to the geometric mean oscillation frequency, not to be confused with ν defined in equation (4.1). Plugging equation (4.6) into equations (4.4) and (4.5) we can integrate to get the analytic functions

$$\nu(\eta) = 1 - \frac{2 + 2\eta + \eta^2}{2e^\eta} \tag{4.7}$$

$$\epsilon(\eta) = 1 - \frac{6 + 6\eta + 3\eta^2 + \eta^3}{6e^\eta} \tag{4.8}$$

.

We can express the relevant thermodynamic variables in terms of $\epsilon(\eta)$ and $\nu(\eta)$. After rethermalization, the temperature will be

$$\frac{T'}{T} = \frac{\epsilon}{\nu}. \tag{4.9}$$

The density is reduced to

$$\frac{n'}{n} = \frac{N'}{N}\left(\frac{T}{T'}\right)^{3/2} = \frac{\nu^{5/2}}{\epsilon^{3/2}}. \tag{4.10}$$

The time between elastic collisions, $\tau = 1/\Gamma$, can be expressed as

$$\frac{\tau'}{\tau} = \frac{n}{n'}\left(\frac{T}{T'}\right)^{1/2} = \frac{\epsilon}{\nu^2}. \tag{4.11}$$

It has been shown that after roughly five collisions the gas is sufficiently rethermalized (Snokes, *et al.*, 1992). Given this, we set the time for rethermalization to be $\tau_{retherm} = 5\tau$. This determines the timescale for the rethermalization process. Lastly, the phase space density is

$$\frac{\rho'}{\rho} = \frac{N'}{N}\left(\frac{T}{T'}\right)^{3/2} = \frac{\nu^4}{\epsilon^3}. \tag{4.12}$$

From the scaling laws, we can see that the requirement for the temperature to decrease is that $\nu > \epsilon$, even though both these number are close to one. Under these conditions, the density increases and the time between collisions decreases, similar to magnetic evaporation. The phase space density also increases during free evaporation

4.3.2 Scaling Laws for Adiabatically Lowering the Potential

The second discrete step of our model for evaporation is concerned with adiabatically lowering the trapping potential. If done adiabatically, the number of atoms and the phase space density is conserved and

$$\rho' = \rho \tag{4.13}$$

$$N' = N \tag{4.14}$$

therefore

$$N'\frac{\nu'}{T'} = N\frac{\nu}{T} \tag{4.15}$$

$$\frac{\nu'}{T'} = \frac{\nu}{T}. \tag{4.16}$$

Based on this, a second set of scaling laws can be derived to describe the adiabatic lowering of the trap depth. This case is more simple in that there is now only one parameter needed to describe the process,

$$\mu = \frac{U'}{U}. \tag{4.17}$$

Since U = 1/2 m $\bar{\omega}^2 x^2$ and $\bar{\omega} = 2\pi\bar{\nu}$, the oscillation frequency scales as

$$\frac{\bar{\omega'}}{\bar{\omega}} = \sqrt{\frac{U'}{U}} = \sqrt{\mu}. \tag{4.18}$$

In a harmonic oscillator, the oscillation frequency is proportional to the temperature, so the temperature also scales as

$$\frac{T'}{T} = \sqrt{\mu}. \tag{4.19}$$

The density scales as

$$\frac{n'}{n} = \left(\frac{T}{T'}\right)^{3/2}\left(\frac{\bar{\omega'}}{\bar{\omega}}\right)^3 = \mu^{3/4}. \tag{4.20}$$

And lastly, the time between collisions goes as

$$\frac{\tau'}{\tau} = \frac{n}{n'}\sqrt{\frac{T}{T'}} = \frac{1}{\mu}. \tag{4.21}$$

The timescale for lowering the potential is derived from the adiabatic constraint that the potential must be lowered in a time slower than an atom oscillates in the trap. We set this time to be twice the geometric mean oscillation period,

$$t' = t + \frac{2}{\bar{\nu'}}. \tag{4.22}$$

Again, from the scaling laws we can make some predictions about the behavior of the thermodynamic variables during forced evaporation. Since the value of μ is less than one (typically we use $\mu = 0.98$), equation (4.19) and equation (4.20) predict that the temperature and density will decrease when the potential is adiabatically reduced. Since both the temperature and density are reduced, the time it takes to rethermalize the sample is increased.

After the potential has been adiabatically lowered, $U/10 < T$. This triggers evaporation to reoccur. Atoms will collide and rethermalize, again ejecting the hottest atoms in the sample. This step goes on for the time $\tau_{retherm}$, then the potential is lowered and the process repeats.

4.3.3 Background Collisions

The loss due to collisions with background atoms can be modeled by multiplying the N dependence by $e^{-\Gamma_{bg}t}$ in the scaling equations above. Γ_{bg} was defined chapter 3.

Evaporation must be completed in a timescale comparable to the lifetime due to background collisions. After this time, the losses due to background collisions overwhelm the evaporation process and progress towards higher phase space densities stagnate. The work presented here shows a factor of three longer lifetimes than earlier work [Newell, 2003].

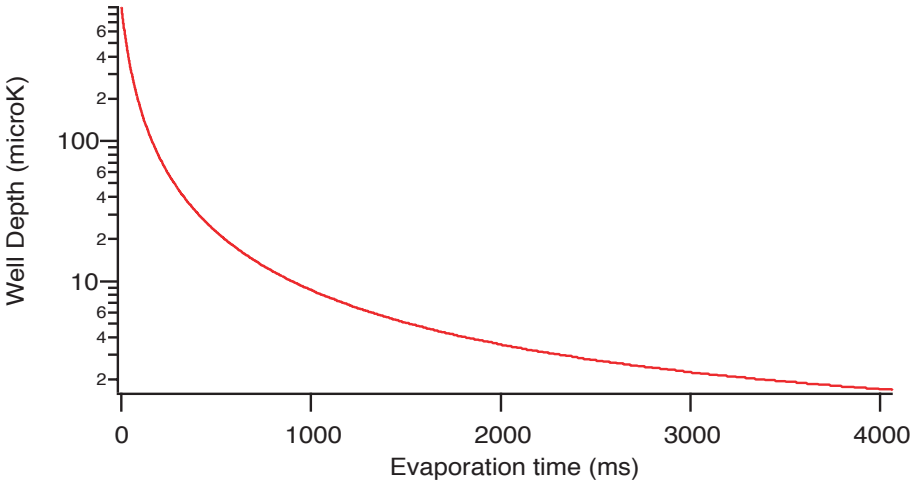

Fig. 4.2.— A typical evaporation curve with $\mu = 0.98$.

4.4 Model vs. Experiment

The goal of the model is to generate a curve for trap depth as a function of time that will yield an optimal final phase space density. A typical curve is shown in figure 4.2. The general shape of the curve is easy to understand. At the beginning of evaporation, the densities and the oscillation frequencies are highest therefore allowing the ramp to proceed rapidly. Towards the end, both density and oscillation frequencies decrease causing the ramp to slow. After trial and error (Newell, 2003) we have determined $\mu = 0.98$, which corresponds to an η= 10, to be an optimal value. The potential ramp is implemented by adjusting the RF power sent to the YAG AOM (discussed in Chapter 2). This adjusts the YAG power and thus the trap depth. We take absorption images at various points throughout the evaporation to characterize the number, center well fraction, and temperature. Below I will discuss how well our theoretical model describes our measured HAT values.

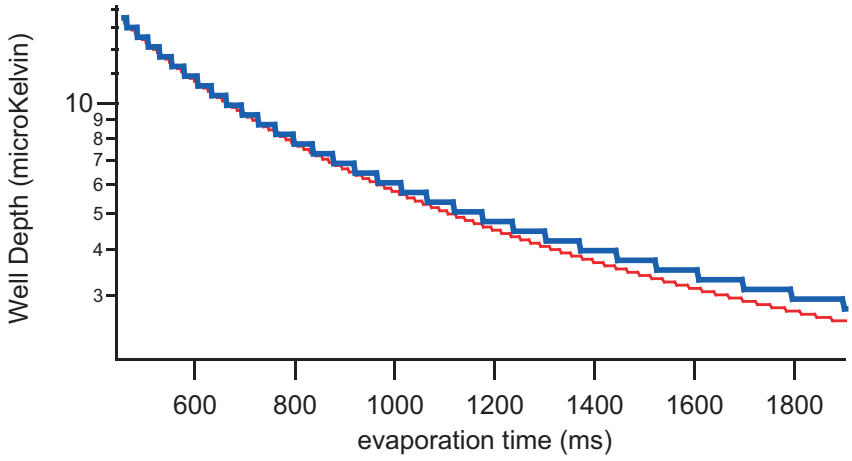

Fig. 4.3.— Well depth as a function of time for center microtrap and outer microtrap

4.4.1 Center Well Fraction

The density and oscillation frequency of the center microtrap sets the timescale for the rethermalization and adiabatic lowering of the potential. The outer wells have a lower density; atoms in those wells have lower oscillation frequencies and it takes longer to rethermalize those atoms. As a result, the adiabatic requirements for the outer wells is different from that of the center well. I have modeled this process; the result of these two effects is an additional atom loss from the outer wells and thus an increase in the center well fraction at later evaporation times. Figure 4.3 compares the potential as a function of time for the center well and an outer well. The evaporation dynamics in the outer wells are always lagging behind the dynamics in the center well. As a result, the outer wells are forced to take bigger cuts which mean costly atom loss. Figure 4.4 is a plot of the microtrap distribution before and after evaporation. A typical microtrap distribution prior to evaporation is input to the model. Then using the parameters of the experiment, we apply a typical curve for the trap depth as a function of time to each of outer wells and record the atom loss. This generates the

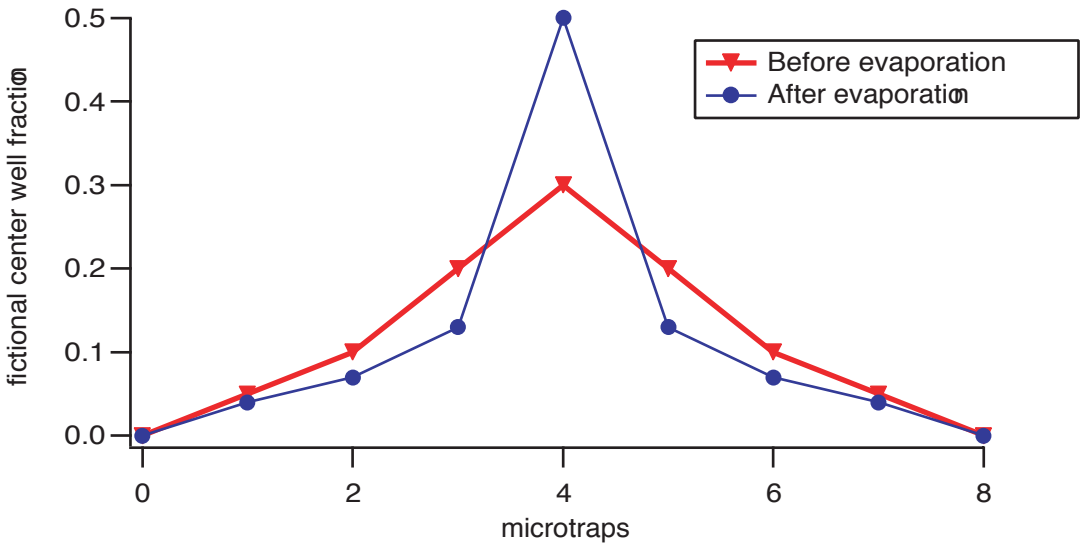

Fig. 4.4.— The enhancement of the center well fraction during evaporation.

post-evaporation distribution shown in figure 4.4. Note the increase in the center well fraction after evaporation.

Experimentally we measure the center well fraction as a function of evaporation time. The measurement procedure is outlined in chapter 3. Figure 4.5 shows that experimentally we measure an increase in the fraction of atoms in the center microtrap as a function of time. Typically we start with 6% and by the end of evaporation we measure 25-30%. By using the method of "shake-n-bake" discussed in Chapter 3, this number can be improved to at least 40%.

4.4.2 HAT Number

Figure 4.6 shows the theoretical prediction and experimental results for the number of atoms in the center well as a function of evaporation time for the curve shown in figure 4.2. Dots are experimental points. Solid line is theoretical. The data was collected for this plot as long as the S/N ratio for the image was greater than 1. The

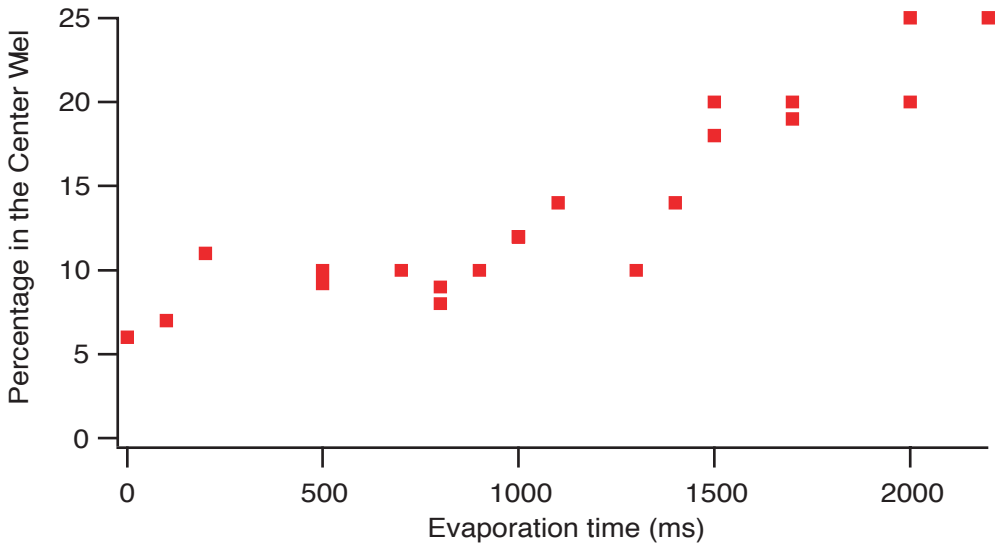

Fig. 4.5.— Typical data for the enhancement of the center well fraction during evaporation

model captures the general trend in the atom loss, but fails to accurately predict the final number of atoms in the center microtrap. Even with the inclusion of the center well enhancement and background collisions, we measure a greater atom loss from the trap then predicted by the model. This point will be revisited in Chapter 6.

4.4.3 HAT Temperature

At the beginning of forced evaporation, the temperature is approximately 60 μK. Using the ramp in figure 4.2 we measure the temperature of atoms, via time-of-flight, in the HAT as a function of time. We find quite good agreement with the theoretical curve (see figure 4.7). Again, the dots are experimental points, and the solid line is the model.

For the interest of the reader, the coldest temperature ever measured after evaporation was 400 nK. Typically we can cool the atoms by over two orders of magnitude

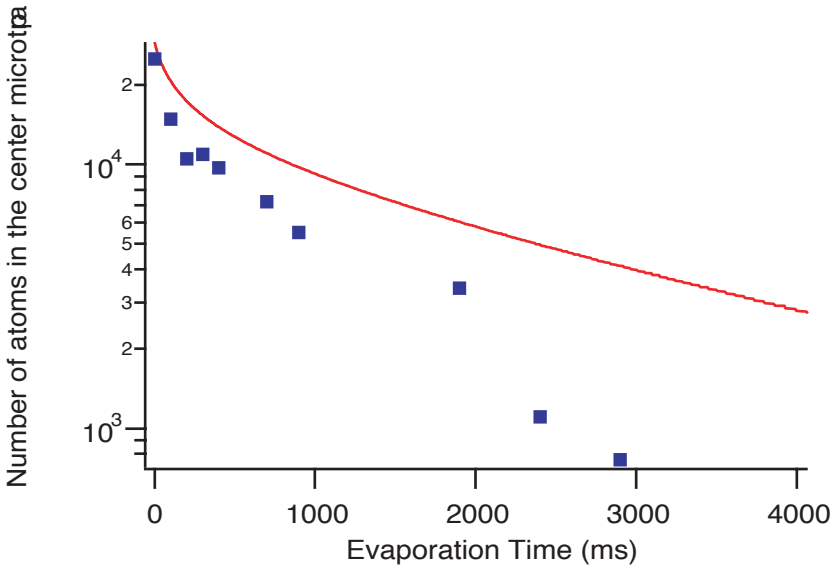

Fig. 4.6.— Number as a function of time for evaporation.

during the course of forced evaporation.

4.4.4 Phase Space Density

The phase space density as a function of time is shown in figure 4.8. The theoretical prediction, represented by the solid line, is derived from the predicted number of atoms in the trap, the predicted temperature of the atoms, and the oscillation frequency of the atoms in the trap. The data, represented by the squares, is a result of knowing the oscillation frequency (measured by parametric heating), the number (figure 4.6) and the temperature (figure 4.7). After loading and free evaporation, the phase space density at the beginning of forced evaporation is typically 1/200. According to the model, we should have a phase space density of 1.5 after 2 seconds of evaporation. We measure, however, a phase space density of 0.75. This discrepancy between the model and the experimental results is almost entirely due to the fact that experimentally we measure more atom loss than the model predicts. The model also predicts that if we

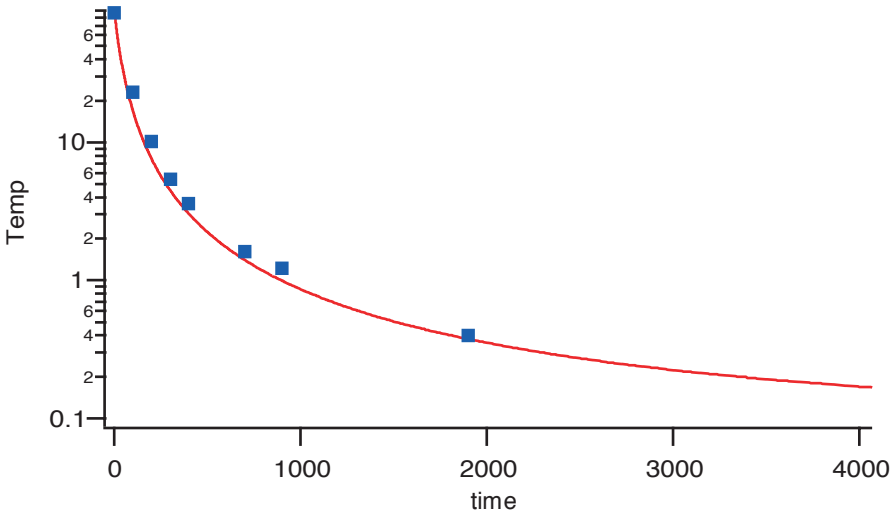

Fig. 4.7.— Temperature as a function of time for evaporation.

evaporated for a longer amount of time, 4 seconds, the phase space density would stagnate at 2.5. This stagnation is a result of collisions with the background gases. The lifetime of HAT is limited by background collisions to be approximately 3 second. If the evaporation cycle is not completely in a time less than this lifetime, the process becomes too inefficient to make progress towards increasing the phase space density.

The highest phase space density we have measured in the HAT is 1.1 (see figure 4.9). For this data set and in the absence of the additional atom loss, theoretically quantum degeneracy would occur after only 2.4 seconds of evaporation.

4.4.5 HAT Density

As discussed above, the density in the HAT will decrease during forced evaporation. Typically the beginning density is 2×10^{14} atoms/cm^3. This density is important to the success of the evaporation. At these high densities the rethermalization rate is fast and evaporation can proceed quickly. Initial collision rates in the HAT are in excess of 30,000/sec. Using the ramp in figure 4.2, the number measured in figure 4.6,

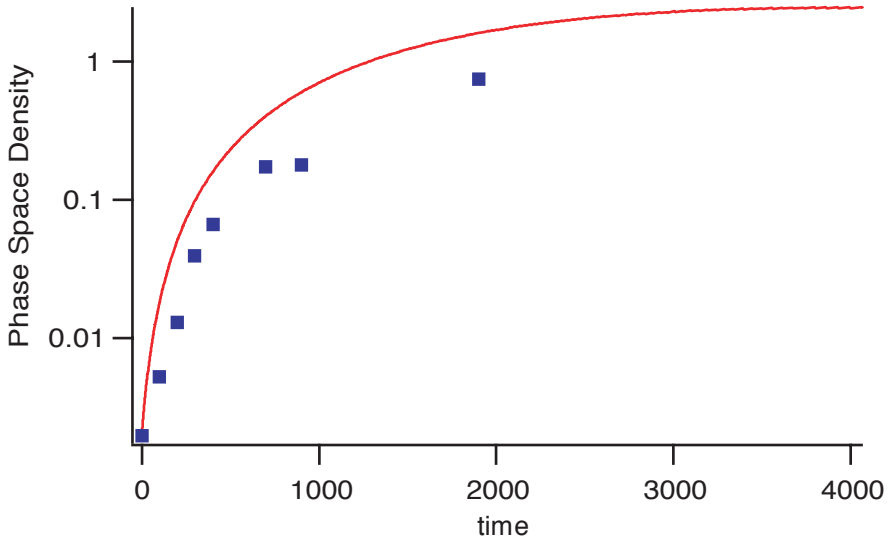

Fig. 4.8.— Phase space density as a function of time for evaporation.

and the temperature measured in 4.7, the model can predict the density as shown by the solid line in figure 4.10. Again, the disagreement between experiment and theory hinges on the fact that we measure an atom loss not predicted by the theory. The density decreases by almost an order of magnitude during evaporation.

4.5 Conclusions

The evaporation of atoms from the HAT can be understood by a simple iterative model which separates evaporation into two steps: the rethermalization of the atom cloud and the adiabatic lowering of the trap depth. The model generates a curve for the trap depth as a function of time which optimizes the final phase space density. We use this theoretical curve as a guide to perform forced evaporation. During evaporation we measure the trap depth (oscillation frequency), the number of atoms per Talbot Fringe, the center well fraction, and the temperature. From this information, phase space density and atomic density can be extracted. Our simple model does a good

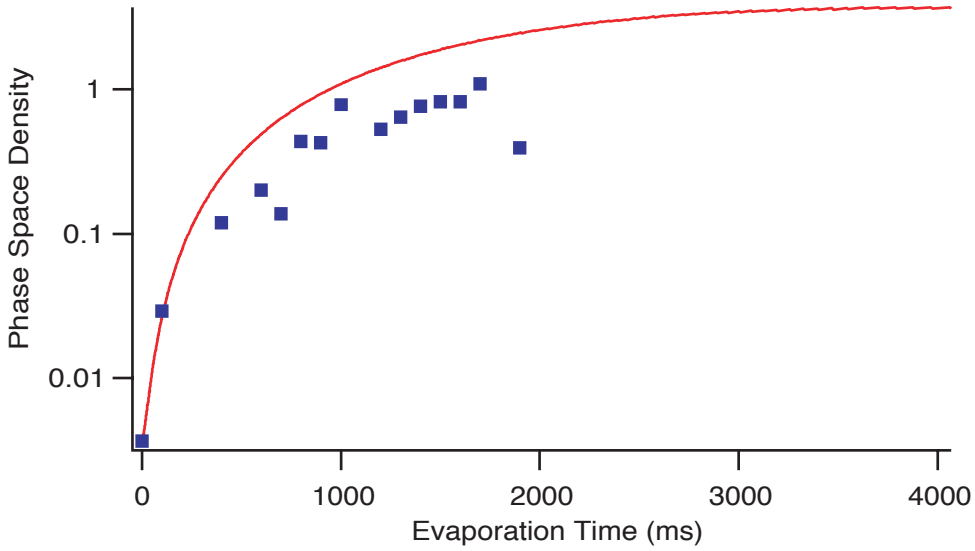

Fig. 4.9.— Highest measured phase space density.

job of explaining the temperature of the atoms during evaporation, but the model fails to predict the additional atom loss that we see. This atom loss is the reason for discrepancies between theory and experiment for the phase space density and atomic density. Despite this atom loss, we have used forced evaporation to improve the phase space density in the HAT by a factor of 250 and have measured phase space densities of 1.1 in less than 2 seconds. Rapid evaporation is possible because the high densities yield fast rethermalization rates.

The unpredicted atom loss is likely a sign of heating mechanisms. Ordinarily, a heating mechanism would cause an increase in temperature, however, during evaporation this is not the case. If a heating mechanism is present, the temperature will still decrease as expected but at the cost of more atom loss. Furthermore, it seems that in the presence of these heating mechanisms, quantum degeneracy is not attainable in the HAT. Chapter 6 will be devoted to discussing these heating mechanisms.

In the next chapter we will discuss the production of high densities, small clouds

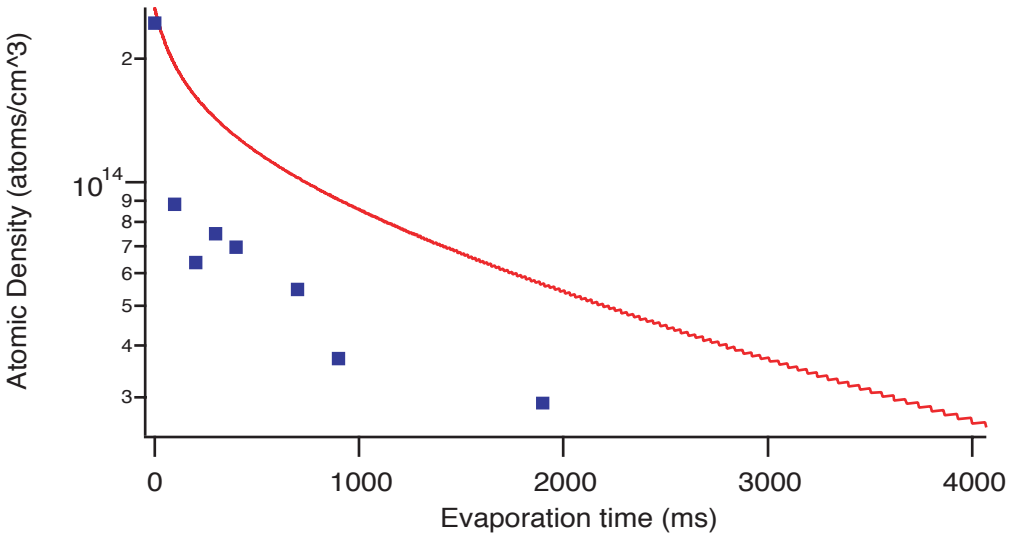

Fig. 4.10.— Density as a function of time for evaporation.

in our HAT. The production of these clouds uses the evaporation model described here to evaporate the atoms to high phase space density. After evaporation the trap depth is adiabatically recompressed. We will show that these samples are well suited for studies of some interesting properties of highly excited Rydberg atoms and their interactions.

Chapter 5

High Density Mesoscopic Samples

5.1 Introduction

In this chapter I will describe a second experiment which makes use of the Holographic Atom Trap. This chapter contains some of the primary results of this dissertation. I will discuss the demonstration of high density, mesoscopic samples and their potential use in Rydberg experiments.

In the experiment described below I will detail a new method to produce high density ($< 10^{15}$ atoms/cm^3) atomic samples (Sebby-Strabley *et al.*, 2004). To our knowledge this is the highest density attained in incoherent ultracold matter. We evaporate atoms in the HAT to high phase space density then adiabatically recompress the potential. This process increases the density by as much as two orders of magnitude. The high densities have been verified three ways: direct measurement of the number, oscillation frequency of the atoms, and the temperature of the atoms; measurement of the 3-body recombination rate; and measurement the cloud size. The model presented in Chapter 4 is modified to include the adiabatic recompression. From the model a simple set of scaling laws is given which governs the process. Also, the optimal conditions for achieving the high densities will also be derived. With these high density

samples new and exciting physics will certainly be revealed. It has been predicted in the literature (Greene *et al.*, 2000) (Boisseau *etal.*, 2002), (Farooqi *et al.*, 2003)that with these densities ultralong range Rydberg molecules, trilobite molecules, can be produced at a high rate. Furthermore, Rydberg plasmas (Simien *et al.*,2004) (Walz-Flannigan *et al.*, 2004) (Gallagher *et al.*, 2003) (Roberts *et al.*, 2004) have never been studied at these densities.

In addition to the high density clouds, we demonstrate the robust production of mesocopic atomic clouds. The clouds discussed in this chapter are as small as 5.6 μm in the longest direction (semi-major axis) and approximately 250 nm in the transverse directions (semi-minor axes). The demonstration of these clouds is important because these clouds have a length scales less than the range of influence for a highly excited Rydberg atom. Evidence for suppression of Rydberg excitation has been seen in MOTs where the range of influence is less than the size of the atomic sample (Tong *et al.*, 2004) (Singer *et al.*, 2004). Experiments that could be done with the clouds presented here are different. The demonstration of these clouds represents progress towards observation of dipole blockade (Lukin *et al.*, 2001).

The chapter concludes with some discussion of the prospects for achieving total blockade. Appendix B estimates the probability of exciting two Rydberg atoms within a single microtrap. The results of this calculation are summarized in the text. For a cloud with a semi-major axis of 5.7 μm, the probability of two excited Rydberg atoms is approximately 0.001. Furthermore, I discuss the possibilities of using a static electric field to cause a stronger, dipole-dipole interaction between atom pairs. The drawback of this potential is that zeros in the potential and areas of weak interaction occur for certain orientations of atom pairs. In other words, if a Rydberg atom is excited, atoms oriented 54.7° relative to the Rydberg atom will have little or no interaction. This could cause a "leaky" blockade because those atoms are not prevented from being excited.

The anisotropic trap geometry of the HAT mictrotraps, however, virtually eliminates this concern. Even if the dipole-dipole potential is zero or close to zero, there will be a sizable enough van der Waals potential to blockade a second atom from being excited to the Rydberg state. More over we will show that most of the atom pairs have a dipole-dipole shift in excess of 10 MHz, and that there is a small probability of exciting a pair of atoms which has a weak interaction.

5.2 Production of High Density Samples

In this section I will give the theoretical and experimental details of how the high density samples are produced. This method builds on the model discussed in chapter 4. Like before, we evaporate the sample to high phase space density, but now we add a step of adiabatically increasing the potential which compresses the atomic clouds. With this method we have demonstrated densities in excess of $1 \times 10^{15}/\text{cm}^3$ and a dynamic range of 20 in the final density. I will discuss the theory behind the adiabatic recompression, derive the conditions for achieving the highest densities, and finally give some results.

5.2.1 Adiabatic Recompression

We begin with the model discussed in chapter 4 which describes evaporation in the HAT. After the evaporation is complete, we append to the model a procedure to adiabatically increase, or recompress, the potential. Again, a set of simple scaling laws is used to gain insight into the dynamics. At a trap depth of U_b we begin the recompression. If the recompression is adiabatic then the phase space density is conserved. This sets the condition that

$$\frac{\nu_b^3}{T_b^3} = \frac{\nu_t^3}{T_t^3} \tag{5.1}$$

where the subscripts b denotes values at the "bottom" of the ramp, or after evaporation. The subscript t represents values at the "top" of the ramp, or after recompression. The oscillation frequency will increase as

$$\nu_t = \nu_b \sqrt{\frac{U_t}{U_b}}. \tag{5.2}$$

as will the temperature (using equation (5.1))

$$T_t = T_b \frac{\nu_T}{\nu_b} = T_b \sqrt{\frac{U_t}{U_b}}. \tag{5.3}$$

The ratios of the densities at the top and bottom therefore scale as

$$\frac{n_t}{n_b} = \frac{(\nu_t/\nu_b)^3}{(T_t/T_b)^{3/2}} = \left(\frac{\nu_t}{\nu_b}\right)^{3/2} \tag{5.4}$$

so the final density is given by

$$n_t = n_b \left(\frac{U_t}{U_b}\right)^{3/4}. \tag{5.5}$$

Indeed, adiabatically recompressing the trap increases the density almost linearly with the change in the trap depth. Unlike evaporation which relies on the rethermalization of the atoms after every step, the adiabatic recompression of the potential does not need to be done step-wise and can be done in one step. Equation (5.5) suggests that the lower you make U_b, the higher the final density. Considering that we have a large dynamic range of the trap depths, a factor of 600, this increase in density can be a factor of 120. A simple argument given in 5.2.2 reveals that this is not exactly the case in the HAT, and the optimum condition for achieving the highest density is derived.

It is interesting to point out that after recompression a typical value for the temperature is 8 - 10 μK and U = 600 μK, therefore T<U/10. In this situation evaporation is "shut off" and a heating mechanism will heat the atoms, not cause atom loss. This will be exploited in Chapter 6 to measure heating rates.

5.2.2 Derivation of Optimum Conditions for High Densities

The question to be addressed is: what value of U_b gives the highest n_t? To answer this we need to rewrite the density at the bottom in terms of the phase space density at the bottom

$$n_t = n_b \left(\frac{U_t}{U_b}\right)^{3/4} \tag{5.6}$$

$$\sim \rho_b T_b^{3/2} \left(\frac{U_t}{U_b}\right)^{3/4}. \tag{5.7}$$

Using our results from evaporation that $U_b = 10T_b$ we derive that

$$n_t \sim \frac{\rho_b T_b^{3/2}}{T_b^{3/4}} U_t^{3/4}, \tag{5.8}$$

and for fixed value U_t the equation for the optimum density is

$$n_t \sim \rho_b T_b^{3/4}. \tag{5.9}$$

As discussed in Chapter 4, evaporating to lower potentials does not necessarily lead to higher phase space densities – the phase space density can stagnate or even decrease after long evaporation times due to heating mechanisms and collisions with background atoms. From this we can conclude that by starting the recompression at a value of U_b which optimizes the function $\rho_b T_b^{3/4}$, the highest densities will be realized. A plot of $\rho_b T_b^{3/4}$ as a function of U_b is given in figure 5.1. From the graph it is clear that the optimum trap depth to start the adiabatic recompression is at $U_b = 8 - 10\mu$K.

5.2.3 Results and Comparison to Theory

To test the model we show recompression densities for several values of U_b in figure 5.2. The points are data; the solid line is the model. The center microtrap densities were measured by measuring the oscillation frequencies, the number of atoms, and the temperature of the atoms. More detail on the density measurements is given in section

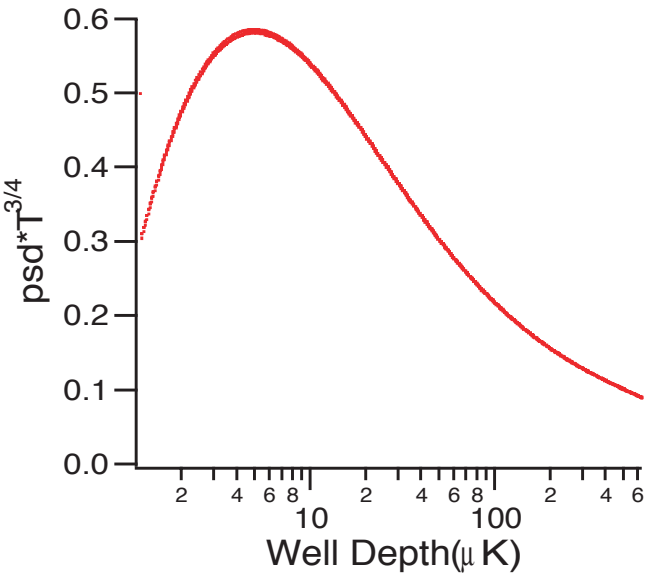

Fig. 5.1.— $\rho T^{3/4}$ as a function of trap depth.

5.3.1. Figure 5.2 shows that the experiment agrees with the theory quite well. Figure 5.2 also verifies that by varying U_b, the resulting n_t is also varied. The circles represent a U_b of 100 μK and result in n_t = 7 x 10^{14}/cm^3; squares represent U_b = 50 μK and n_t = 1 x 10^{15}/cm^3; and lastly, the triangles show $U_b = 10\mu$K and n_t = 2 x 10^{15}/cm^3. Our highest densities were achieved at $U_e = 10\mu$K which agrees with the predictions of figure 5.1.

It is interesting to point out that the timescale for the recompression is just the adiabatic constraint described in Chapter 4. As a result the recompression can be done quite quickly. Furthermore, unlike evaporation, this constraint becomes less time consuming as the recompression continues and is even a bit flexible. The potential for the $U_e = 10\mu$K data in figure 5.2 was raised faster than normal adiabatic constraints would allow to limit losses due to background collisions. The result is a small break down of the scaling laws in section 5.2.1 which assume perfect adiabaticity.

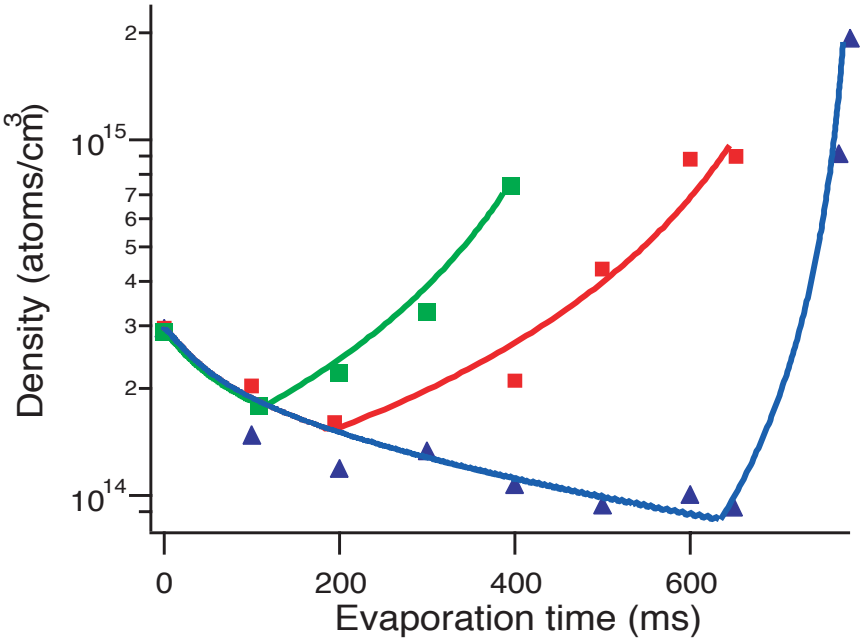

Fig. 5.2.— Recompression data for several values of U_b.

5.3 Verifying the Densities

This section details three methods of verifying the densities claimed in section 5.2.3. The first method involves precise measurement of the number in the center microtrap, the temperature, and the oscillation frequency. The second method is measuring the 3-body recombination rate for atoms in the microtraps and comparing our measured rates to previous measurements (Tolra *et al.*,2004) (Burt *et al.*,1997). This method is very sensitive to the density as the loss rate is proportional to n^2; below I will show that our measured rates are in good agreement with previous measurements. The final verification is the direct measurement of the spatial distribution of atoms in the microtrap.

5.3.1 Direct Measurement of N, ν, and T

The first method for verifying our densities is direct measurement of N, ν, and the temperature, then calculating the density using equation 4.10. The calibrated method used to measure N is given in chapter 3. From this we measure that the number of atoms in the highest density samples is 11310 ± 2300 atoms. As discussed in chapter 2, the x and z oscillation frequencies are measured with parametric heating (Friebel *et al.*, 1998) to be 18.400 kHz $\pm$ 1.2 kHz and 735 Hz $\pm$ 62 Hz. The geometric mean is then 6300 Hz $\pm$ 330 Hz. Lastly the temperature is measured by time-of-flight (see Chapter 3) to be 8.82 μK $\pm$ 0.4 μK. From this we calculate the density to be 1.8 ± 0.5 x $10^{15}/\mathrm{cm}^3$.

5.3.2 Three Body Recombination Rate Coefficient

Putting aside the existence of heating meachanisms, it is a good approximation that the loss rates measured in the HAT are dominated by one-body and three-body processes. Two-body losses can be neglected (Burt *et al.*,1997) and we can write the following rate equation to describe the atom loss

$$\frac{dN}{dt} = -K_3 \int n(t)^3 \, dV - K_1 N \tag{5.10}$$

where K_3 is the 3-body recombination rate coefficient and $K_1 = \Gamma_{bg}$, the one-body loss rate coefficient.

We measure the number of atoms per Talbot fringe as a function of time immediately after recompression. Since the fraction of atoms in the center microtrap is fixed during recompression, the number of atoms in the center microtrap can be extracted in the usual way. The data is shown in figure 5.3. In the presence of 3-body recombination we see rapid atom loss until the density decreases enough that the 3-body collisions are suppressed. On a longer timescale the collisions with the background gas dominate,

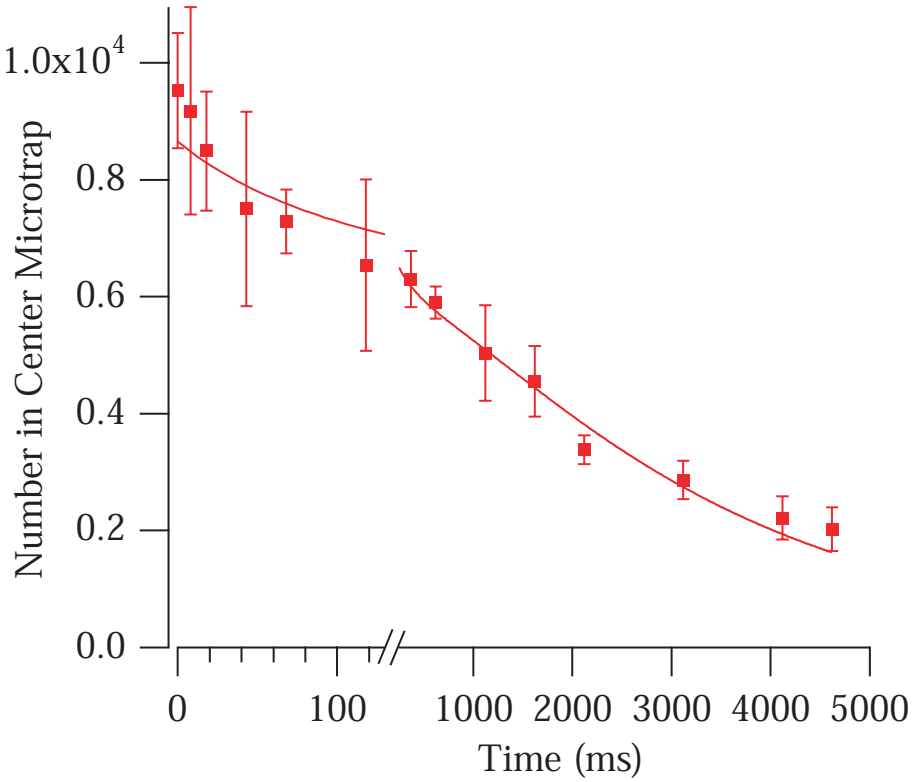

Fig. 5.3.— Number of atoms in the center microtrap as a function of time after recompression.

giving the final slow decay process.

We can determine the 3-body recombination rate from the fit to the data. The fitting function is derived in Appendix A, however, there are two complications. First, in the fitting function we have to take into account any temperature increase due to heating. As mentioned in section 5.2.1, if a heating mechanism is present it will raise the temperature of the atoms and cause the density to decrease. In figure 5.3 the density is decreasing due to both atom loss from the 3-body recombination and due to heating.

The second complication comes from the fact that by measuring the number of

atoms per Talbot fringe, which includes atom clouds of varying densities, we measure the losses from a sample whose effective density is less than the density of the center microtrap. The measured 3-body loss rate might be artificially lowered by this effect. From Appendix A, the measured loss rate from three-body recombination is

$$\frac{dN_{Talbot}}{dt} = \frac{-K_3 n_{eff}^2 N}{3^{3/2}} = -\frac{K_3}{3^{3/2}} \left(\frac{n_{eff}}{N}\right)^2 N^3 = AN^3 \tag{5.11}$$

where K_3 is the 3-body loss rate averaged over the entire Talbot fringe and A is a parameter in the fit function defined in Appendix A. We have modeled this effect and determined a correction factor. The model proceeds as follows. Initially we take the simplified case of only two microtraps. The loss rate from the two traps can be written as

$$\frac{dN}{dt} = \frac{-K_3'}{3^{3/2}} \left[\left(\frac{n_2}{N_2}\right)^2 N_2^3 + \left(\frac{n_1}{N_1}\right)^2 N_1^3\right] \tag{5.12}$$

where K_3' is the corrected 3-body recombination rate. Letting f_i be the fraction of the atoms in the i^{th} microtrap, we can rewrite this and equate it to equation 5.11

$$\frac{dN}{dt} = -K_3' \left[\left(\frac{n_2}{N_2}\right)^2 f_2^3 + \left(\frac{n_1}{N_1}\right)^2 f_1^3\right] N^3 = AN^3. \tag{5.13}$$

Solving the equation for K_3'

$$K_3' = \frac{A}{\frac{1}{3^{3/2}} \left[\left(\frac{n_2}{N_2}\right)^2 f_2^3 + \left(\frac{n_1}{N_1}\right)^2 f_1^3\right]} \tag{5.14}$$

and generalizing to the case of many wells,

$$K_3' = \frac{A}{\frac{1}{3^{3/2}} \sum_{i>0} \left(\frac{n_i}{N_i}\right)^2 f_i^3}. \tag{5.15}$$

Now we multiply the top and bottom by $3^{3/2}(N_0^2/n_0^2)$ where N_0 and n_0 are the number and density in the center microtrap respectively. The numerator is equation A.18 in Appendix A for K_3. The resulting equation is

$$K_3' = \frac{K_3}{\left(\frac{N_0}{n_0}\right)^2 \sum_{i>0} \left(\frac{n_i}{N_i}\right)^2 f_i^3}. \tag{5.16}$$

The denominator is the correction factor for having multiple wells. In practice we fit N_{talbot} versus time and determine K_3 from equation (A.18). Then we use equation 5.16 to find the 3-body recombination rate for the maximum density in the center microtrap. A typical value for the correction factor is 0.00571, concluding that the 3-body recombination rate for the maximum density in the center microtrap is 170 times higher than the 3-body recombination rate averaged over the effective density of the Talbot fringe.

Including all this factors we have concluded that our 3-body recombination coefficient is $K_3 = 3.5 \pm 1.9$ x 10^{-29} cm^6/sec. This is in good agreement with Burt *et al.* who measured $K_3 = 4.3$ x 10^{-29}cm^6/sec. To our knowledge, this was the first measurement of the 3-body recombination rate made in a purely optical trap. We repeated the measurement in a 2.5 Gauss bias field, typical of a field present in magnetic traps, and measured $K_3 = 4.8 \pm 2.3$ x 10^{-29} cm^6/sec. The difference between the rates is insignificant and we concluded that the presence of the bias field was not important for making the measurement. The good agreement with the measurements of Burt *et al.* are a second confirmation that the recompressed atomic densities are in excess of 1 x 10^{15}/cm^3.

5.3.3 Spatial Measurement

The third validation of the densities is to measure the spatial distribution of atoms in the microtrap. In the x and y direction the thermal radius is several hundred nm, much too small to be resolved. We can, however, resolve the z-axis which provides confirmation in the measured oscillation frequency and temperature, both important factors in determining the density. The calculated z-axis thermal radius, $\sigma_{calc} = \sqrt{2kT/m\omega_z^2}$ for T = 13 μK and $\omega_z = 2\pi \times 735$ Hz is 10.8 μm. We measure a radius of 12.09 μm, but there are several factors that affect this measurement. The

measured z-axis radius is

$$\sigma_{measured} = \sqrt{\sigma_{diffraction}^2 + \sigma_{calc}^2 + \sigma_{TOF}^2} \tag{5.17}$$

where σ_{TOF} takes into account the motion of the atoms during the imaging pulse, and $\sigma_{diffraction}$ is the diffraction limited radius calculated from the diameter and focal length of the imaging lens and the wavelength of the imaging laser. I have modeled σ_{TOF} for a velocity of 5 cm/s and an imaging pulse of 200μs to be $\sigma_{TOF} = 3.5$ μm.

The resolution of our imaging system is limited by aberrations and can be improved by using an iris to limit the amount of the lens used to make the image. We put an aperture in front of the imaging lens (f = 150 mm) and experimentally determined that a diameter of 15 mm yields the highest resolution. The diffraction limit for d = 15 mm is 4.8 μm. Using these values in equation (5.17), $\sigma_{measured} = 12.3\mu$m. We can understand our measurement within 0.21 μm which serves as third validation that our measured oscillation frequencies, temperatures, and thus densities are correct.

5.4 Mesoscopic Samples

In this section I will discuss the production of mesoscopic atomic samples. Here we are less concerned with density and more concerned with attaining small cloud sizes. Experimentally this is done in much the same way as generating high densities; the cloud is evaporated to high phase space densities and then rapidly recompressed. The production of mesoscopic samples is different from the production of high density samples in that it has a different set of optimal conditions. I will also discuss the prospects of seeing a complete, or near complete, dipole blockade and how the highly anisotropic nature of HAT has some advantages for dipole blockade.

5.4.1 Derivation of Optimum Conditions

The thermal radius of the cloud after recompression scales as

$$\sigma_t = \sigma_b \sqrt{\frac{T_t}{T_b}} \left(\frac{\nu_b}{\nu_t} \right). \tag{5.18}$$

Since the recompression is adiabatic, equation (5.1) applies. The result is

$$\sigma_t = \sigma_b \sqrt{\frac{\nu_b}{\nu_t}} = \sigma_b \left(\frac{U_b}{U_t} \right)^{1/4}. \tag{5.19}$$

This suggest that minimizing U_b yields the smallest thermal radius. The 1/4-power dependence means a large U_b/U_t ratio is necessary to achieve substantial size reduction.

5.4.2 Results

We have demonstrated a dynamic range in the trap depth of 300, giving a factor of 4 reduction in the radius. During evaporation the radius is constant because the radius is proportional to T/U which is held constant by the evaporation process. After the completion of free evaporation, the z-direction radius is always 23 μm . By evaporating to a trap depth of $U_b = 2\mu$K, the recompressed z radius is 5.6 μm and 220 nm in the x and y-direction.

These radii are all too small to be resolved with our imaging system. The best way to verify these sizes is to use the measured temperature and oscillation frequencies to calculate the radius. Since there are only about 2000 atoms left in the microtrap at this time, it is difficult to have sufficient signal-to-noise ratio to get an accurate measurement of the atoms' temperature. We have observed clouds which resulted from evaporating to a $U_b = 2\mu$K, but we were unable to measure the temperature of these atom clouds. From the scaling relationship in equation (5.19) we can conclude that the clouds had a thermal radius of 5.6 μm. We were, however, able to measure the temperature for a cloud which resulted from evaporating to $U_b = 4\mu$K. Using

the measured temperature and the measured oscillation frequency, we calculated the thermal radius of this cloud to be 8 μm.

5.4.3 Prospects of Dipole Blockade

As mentioned above, if the size of the clouds is smaller than the effective range of the Rydberg atom, a total blockade of the production of multiple Rydberg atoms is possible. We estimate here the probability of a double excitation, P_2. The details for calculating P_2 are given in Appendix B. I will assume the following scenario. In our experiment, the Rydberg atoms are excited via a 2 photon transition into a Rydberg state with principle quantum number n. We will assume that the first photon comes from a laser with $\lambda = 780$nm and a beam waist large compared σ. The second photon comes from a laser with $\lambda = 480$nm and has a beam waist w which is comparable to σ. We apply a pulse of the 480 nm laser light for a time, T. For n = 95 Rb atoms, a Gaussian beam waist of w = 10 μm, and a pulse width T = 1 μs we can calculate a mean frequency shift for the cloud, $\overline{\Omega}$, for an arbitrary potential. This is given as

$$\frac{1}{\overline{\Omega}^2} = \frac{2(1+2\sigma^2/w^2)}{N^2} \sum_{i<j} \frac{e^{-2(x_i^2+x_j^2)/w^2}}{\Omega_{ij}^2}. \tag{5.20}$$

where Ω_{ij} frequency shift between pairs of Rydberg atoms. For the case of a van der Waals potential this is given by

$$\Omega(R) = \frac{\delta}{2} + \sqrt{\frac{4U_3(R)^2}{3} + \frac{\delta^2}{4}} \tag{5.21}$$

where δ is the energy for the $s + s \rightarrow np + (n-1)\,p$ defect, $U_3(R) = C_3/R^3 = e^2\langle ns||r||np\rangle\langle ns||r||(n-1)p\rangle/R^3$, and C_3 is the van der Waals coefficient (Walker et al., 2004). Using equations (5.21) and (5.20) we can calculate the probability, P_2 that there will be 2 excited Rydberg atoms,

$$P_2 = \frac{\pi^2}{2T^2\overline{\Omega}^2}. \tag{5.22}$$

$\sigma(\mu m)$	w (μm)	$\Omega/2\pi$(MHz)	P_2
8.0	10	10.5	1.1×10^{-3}
8.0	20	2.09	0.029
8.0	∞	0.92	0.148
5.7	10	28	2×10^{-4}
5.7	20	8.8	1.6×10^{-3}
5.7	∞	5.1	4.9×10^{-3}

Table 5.1: Summary of the dipole-diople shifts and probabilities of doubly excited states in the HAT for various σ and w values.

Table 5.1 shows the blockade results for various cloud sizes, σ, and Gaussian beam waists, w, for 95 s states in Rubidium. Even using the clouds with thermal radius of 8 μm, a large enough frequency shift would result that the probability of exciting two Rydberg atoms would be 0.1%. Given these low probabilities, it seems that the HAT is a good candidate for the observance of Rydberg blockade.

5.4.4 Elimination of Dipole Zeros

In the absence of any external field, the interaction of two Rydberg atoms is very short-ranged and has a $1/\mathrm{R}^5$ or $1/\mathrm{R}^6$ dependence. As discussed in (Walker et al., 2004), under certain unusual conditions application of an external electric field can greatly enhance this interaction in a resonant collision process known at a Föster process. The resulting interaction goes as $1/R^3$ and is isotropic. More generally, in the presence of an external field the Rydberg atoms can also acquire a "permanent" dipole moment, $\mathbf{p}$, causing the familiar dipole-dipole interaction

$$V_{DD} = \frac{1}{4\pi\epsilon_0}\left(3\mathbf{p}_A \cdot \hat{\mathbf{R}}\hat{\mathbf{R}} \cdot \mathbf{p}_A - \mathbf{p}_A \cdot \mathbf{p}_B\right) = \frac{1}{4\pi\epsilon_0}\frac{p^2}{R^3}\left(3\cos^2\theta - 1\right) \tag{5.23}$$

where θ is shown in figure 5.4 and $\mathbf{R}$ is the interatomic separation. The dipole moment is $p \approx n^2 e a_0$, so for highly excited Rydberg atoms this interaction can be made quite large. The only unfortunate drawback of this potential is that at $\theta = 54.7°$ the interaction is

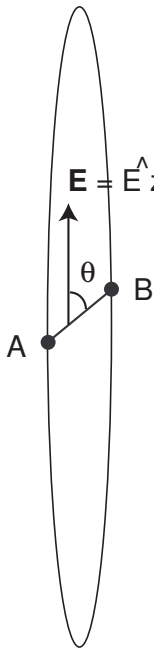

Fig. 5.4.— Microtrap orientation relative to external electric field

zero. This could cause a "leaky" blockade because for atom pairs oriented 54.7° from the electric field there is no mechanism for blockading the excitation to the Rydberg state for the the pair of atoms. Furthermore, atoms pairs close to this orientation will have a weak interaction thus increasing the probability for a doubly excited Rydberg state.

In the HAT, this is less of a concern. After recompression in the HAT, the radii in the x and y directions are between 250 and 360 nm. By orienting the electric field along the z-axis we can take advantage of the highly anisotropic geometry of the HAT in order to nearly eliminate the problem of zeros in the potential. We have estimated the dipole-dipole blockade in a method similar to that done for the van der Waals interaction. Figure 5.5 shows histograms of the number of atoms pairs that experience a certain dipole-dipole shift for two different trap geometries. The top histogram is for the case of a trap with isotropic geometry with cloud radii 5.7μm $\times$5.7μm $\times$5.7μm.

The bottom histogram is for an anisotropic trap, such as the HAT, with cloud radii 5.7μm $\times$238nm $\times$ 238 nm. In the isotropic trap there are many atom pairs which experience zero or small dipole-dipole shifts. As a result, the mean frequency shift is less than 1 MHz. In the anisotropic trap, the number of atom pairs experiencing a small frequency shift is much less. Most of the cloud experiences a dipole-dipole shift in excess of 10 MHz. According to the histogram, only 7 atom pairs have dipole shifts less than 10 MHz. But according to equation 5.20, there is only a $1/N^2$ probability that a given atom pair will be excited. This make the excitation of weakly interacting pairs unlikely.

If the atom pair is oriented such that the dipole-dipole potential is small or even zero, in the HAT there will still be a sizable van der Waals potential between the atom pair causing a blockade shift. The results for the dipole-dipole blockade are given in table 5.2. For this simulation we took Ω_{ij} in equation (5.20) to be $\Omega_{ij} = \sqrt{\Omega_{dd}^2 + \Omega_{vdw}^2}$ where Ω_{dd} is the frequency shift caused by the dipole-dipole interaction and Ω_{vdw} is the shift caused by the van der Waals interaction. Again we assume that the doubly-excited n = 95 pair is being produced for a π-pulse of T = 1 μs.

By comparison of Table 5.2 with Table 5.1, it is clear that much larger frequency shifts and hence smaller P_2 values result by using a dipole-dipole interaction. For the case of a isotropic trap of cloud radius 5.7 μm and a Gaussian beam waist of 10 μm, the combined dipole-dipole and van der Waals shift is 415 MHz. Again, far superior

σ	w	$\bar{\Omega}_{vdw}/2\pi$	$\bar{\Omega}_{dd}/2\pi$	$\bar{\Omega}/2\pi$	P_2
8	10	11	197	254	1.9×10^{-6}
8	20	2.2	109	115	9.5×10^{-6}
5.7	10	29	413	415	7.2×10^{-7}
5.7	20	9.2	240	252	2.0×10^{-6}

Table 5.2: Summary of Dipole-Dipole blockade results for various values of σ and w

blockade could be seen in a anisotropic trap such as the HAT, as opposed to an isotropic trap.

5.5 Conclusion

In this chapter I have discussed the demonstration of the rapid production of high density, mesoscopic atom clouds in our Holographic Atom Trap. Using the method of adiabatic recompression we are able to make clouds with atomic densities in excess of $10^{15}/\text{cm}^3$. These densities are the highest densities attained in incoherent matter. The method of adiabatic recompression was appended to the model discussed in Chapter 4 to predict the final densities. The model and the experiment show good agreement. We have also derived the condition for achieving the highest density. It was with these conditions that we were able to produce clouds with atomic densities of $2 \times 10^{15}/\text{cm}^3$. These density measurements were verified three ways: direct measurement of the number, oscillation frequency of the atoms, and the temperature of the atoms; measurement of the 3-body recombination rate; and measurement the cloud size. All the methods showed good agreement and provided strong validation that our measured densities are correct.

We then described a similar experiment which produced atom clouds with a radii of 5 - 10 μm in the largest dimension and several hundred nanometers in the shorter dimensions. These clouds show good prospect for seeing complete dipole blockade. In order for the blockade to be successful, there must be a low probability that two Rydberg atoms could be excited within a single microtrap. We have calculated a mean Rydberg-Rydberg frequency shift (see Appendix B) caused by the van der Waals potential for n=95 s Rb atoms. From that we have estimated a probability, P_2, that two Rydberg atoms could be excited. The results were summarized in table 5.1. With our $\sigma = 8\mu$m clouds, the probability of 2 Rydberg atoms being excited in π pulse of

duration 1 μs is less than 0.1%. This number is even more encouraging when clouds of size $\sigma = 5.7\mu$m are used. These low probabilities are very encouraging and show good prospects for seeing a Rydberg-Rydberg blockade.

To conclude the chapter I discussed the prospects of seeing dipole-dipole blockade in a microtrap. With the addition of a static electric field, the potential between the atoms becomes the stronger dipole-dipole potential. The difficulty with this potential is that at certain angles the potential is weakened or even zero. This is hurdle that needs to be overcome for the demonstration of dipole-blockade, however, in the HAT this is less of a problem. If any atom pair is orientated such that the dipole-dipole potential is small or even zero, the anisotropic nature of the HAT allows for a sufficiently large enough van der Waals potential to prevent a the excitation of two Rydberg atoms. We have estimated the frequency shifts for pairs of atoms by using the quadrature sum of the dipole-dipole interaction and the van der Waals interaction. The results of these estimations are summarized in Table 5.2. Using an atomic cloud with a radius of 5.7 μm, the mean blockade shift is greater than 400 MHz which results in P_2 values as low as 7×10^{-7}. Furthermore we have shown a histogram for the dipole-dipole blockade shifts seen by pairs of atoms. Only a few atom pairs have blockade shifts less than 10 MHz. According to equation (5.20), there is only a $1/\mathrm{N}^2$ probability of exciting a given pair of atoms. Thus the probability of exciting the weakly blockaded pairs is small. For comparison, a histogram of the dipole dipole blockade shifts for an isotropic trap was given. In this case the mean dipole-dipole shift was less than a MHz. Many atom pairs experience a weak interaction raising serious concerns about the validity of a blockade in a isotropic trap. Nonetheless, the estimations for the HAT are very encouraging and indicate that observation of a high fidelity van der Waals and/or dipole dipole blockade are possible in the HAT.

The ability to produce a completely blockaded transition is integral to the pro-

posed quantum computing scheme of Lukin *et al.* Furthermore, Saffman *et al.* has also suggest using blockaded states as a deterministic single photon source (Saffman *et al.*, 2002). Since only one atom is excited to the Rydberg state, only one photon will be emitted from the atomic ensemble. Using the proper choice and orientation of the laser fields, Saffman *et al.* showed that this single photon scheme can be both on-demand and have directionality, both important factors for quantum manipulation and quantum computation.

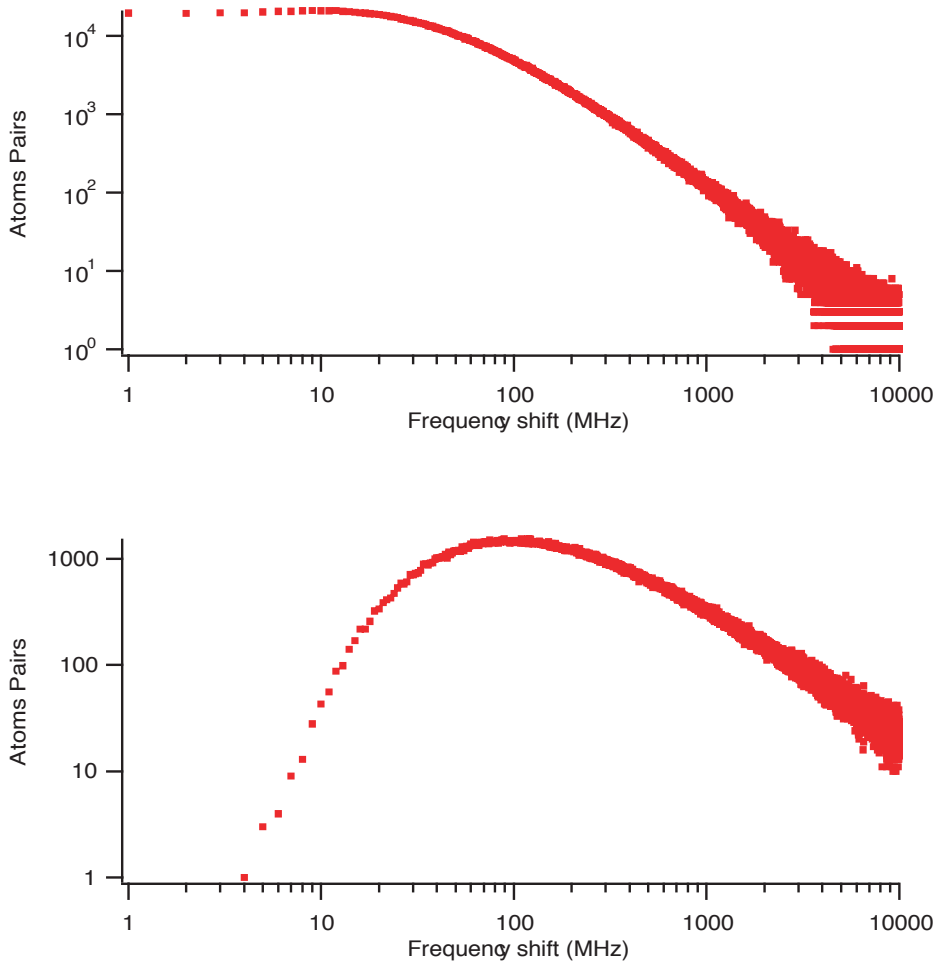

Fig. 5.5.— A histogram for the dipole-dipole shift. The top picture is for a isotropic trap. The bottom is for the HAT geometry.

Chapter 6

Heating Mechanisms

6.1 Introduction and Background

In Chapter 4 I discussed forced evaporation in the Holographic Atom Trap. While comparing our model with our experimental results, the model was unable to explain the extra atom loss. It was suggested that a heating mechanism might have caused the discrepancy.

Heating meachanisms which occur during evaporation manifest themselves in the form of atom loss, rather than in the form of a temperature increase. Recall from Chapter 4 that evaporation will occur until the temperature of the atoms is 1/10 the trap depth. If a heating mechanism is present, evaporation will succeed in decreasing the temperature to 1/10 the trap depth, but at the cost of greater atom loss. This might explain our results.

Our approach to solving this problem was the following. First we needed to answer the question: what heating rate would explain the additional atom loss that we see? Using our model for evaporation, we were able to get a "ball park" idea for the types of heating rates that would cause the atom loss not predicted by our current theory. We found that the heating rate varied as we varied the trap depth, but at

deeper traps depths the heating rates were on the order of 10 μK/sec and at shallower traps the heating rates were approximately 1 μK/sec. The method used to attain these results and the more thorough explanation of the results will be discussed in Section 6.2. With this information we would measure and calculate the heating rates from various heating mechanisms and try to draw a conclusion about the cause of the atom loss.

In Section 6.3, I discuss two categories of heating mechanism: heating due to the confining laser and heating do to collisions with the background gas. Heating due to the confining laser is often a function of the trap oscillation frequencies. During evaporation in an optical trap the oscillation frequencies are constantly changing, therefore we are vulnerable to heating from laser noise at all frequencies. The four types of laser induced heating that I will discuss are photon scattering, pointing stability, heating from intensity noise, and torque heating. The group at Duke has extensively studied heating due to pointing instability and laser noise, and I will be applying their results when applicable. To our knowledge we are the first group to study torque heating. We estimate the heating rates from laser intensity noise, pointing stability, and torque by measuring power spectra of the YAG laser for various conditions. I will show that at low trap depths, the heating rates from laser intensity noise are significant enough to account for some of the atom loss we see. I will also shown that heating due to photon scattering, pointing instability, and torque heating are negligible.

The second type of heating mechanisms, heating caused by collisions with background gases, will be discussed in Section 6.4. These mechanisms include quantum diffractive collisions with background atoms and secondary collisions. Secondary collisions are triggered by a primary collision with a background atom causing a trapped atom to be ejected. As the atom leaves the trap, it undergoes secondary collisions with another trapped atom. The energy transfer in the secondary collisions is not sufficient

to eject the second atom from the trap, but the energy gained in the collision is distributed amongst the remaining atoms in trap as a form of heat. These mechanisms are functions of the trap depth which also change during evaporation. So again, these heating rates must be studied over the range of trap depths. The background that I am referring to can be either a vacuum contaminant, such as hydrogen or helium, or it could be the background Rubidium vapor. Since the installation of a titanium sublimation pump, we are confident that we have very low levels of contaminant. In our case the majority of the background is untrapped Rubidium atoms. I will show that both of these heating mechanisms make a significant contribution to heating rates in the HAT. At large trap depths the dominate heating mechanism is quantum diffractive collisions, and at shallower trap depths secondary collisions become important.

In section 6.5 we discuss a method we have developed for direct measurement of the heating rates. The method is similar to the procedure used to produce the high density, mesoscopic samples. This measurement takes advantage of the fact that after the recompression step $T \ll U/10$ (discussed in Chapter 5), evaporation is effectively "shut off". Under these conditions we can measure the increase in temperature as a function of time. The measured heating rates are in good agreement with the quadrature sum of the calculated heating rates from intensity noise, quantum diffractive collisions, and secondary collisions.

Finally in Section 6.5.2 we discuss modifications we have made to the evaporation model to account for the presence of heating mechanisms. We show that by including the heating due to quantum diffractive collisions and secondary collisions, the model is able to predict the phase space density extremely well, except at the very end where heating from intensity noise probably needs to be considered.

6.2 Preliminary Determination of the Heating Rate

Using the model for evaporation discussed in Chapter 4, we designed an experiment to estimate the heating rate that would account for the extra atom loss. The experiment proceeds as follows. First we would preform forced evaporation to a certain trap depth U_{hold}, hold that trap depth at U_{hold}, and measure atom loss as a function of time. Then using the model we add in a ficticious heating rate and adjust that heating rate to account for the atom loss that we measure. Using this method we determined the heating mechanisms that would be needed at various trap depths to cause the atom loss that we see. This data is shown in table 6.1.

A direct way of measuring heating rates will be given in Section 6.5, but this method gives us a "ball park" range of rates which could be problematic. We will now turn to measuring various heating rates in attempts to determine the heating mechanisms we are effected by.

6.3 Laser Induced Heating

The first category of heating mechanisms that I will discuss are those caused by the confining laser. The four mechanisms that I will discuss are photon scattering, intensity noise, pointing stability, and torque heating. To esimtate the heating due to the last three mechanisms I will be presenting Fourier spectra of the YAG laser light

Trap Depth (μK)	Predicted Heating Rate (μK/sec)
121	7
45	2
5	0.700

Table 6.1: Trap depths and the heating rates at that trap depth that would account for the measured atom loss.

using an Standford Research Systems model SR760 spectrum analyzer.

6.3.1 Photon Scattering

I will first discuss heating due to atoms scattering photons for the YAG laser. We can express the scattering rate as

$$R_{sc} = \frac{\sigma_{rayleigh} I}{\hbar\omega} \tag{6.1}$$

where

$$\sigma_{rayleigh} = \frac{8\pi}{3}\alpha_0^2 k^4 \tag{6.2}$$

where ω is the frequency of the YAG light. Using this equation we calculate the rate to be 0.57 photons/second at maximum trap depth. The energy each YAG photon imparts to a Rb atom is given by E = $\hbar^2$k^2/2m = 194 nK. Therefore the heating rate at U = 600 μK is 111 nK/sec, and the heating rate decreases linearly with decreasing trap depth. The heating rate at a trap depth 5 μK is 925 pK/sec. Clearly, this mechanism is negligible.

6.3.2 Intensity Noise

Heating in a ar off resonant trap can also be the result of intensity fluctuations in the confining laser. Fluctuations in the laser power change the trap depth and thus the spring constant. As we have discussed in Chapter 4, if the trap depth is modulated at twice the trap oscillation frequency, then atoms are heated and ejected from the trap. While this is a useful tool for measuring oscillation frequencies, it can be a source of unwanted heating. The effects of laser intensity noise on atoms in FORTs were done by (Savard *et al.*, 1997) and (Gehm *et al.*, 1998). The major result of these papers was the heating rate due to intensity noise

$$\dot{E} = \left\langle \frac{dE_i}{dt} \right\rangle = \frac{\pi}{2}\omega_i^2 S_k(2\omega_i) \left\langle E_i(t) \right\rangle = \left\langle \dot{E}_i \right\rangle = \Gamma_i \left\langle E_i \right\rangle \tag{6.3}$$

where $S_k(2\omega_i)$ is noise spectral density in units of fractional noise/$\sqrt{Hz}$ and i is the corresponding components in x,y, or z. The solution to equation (6.3) infers that intensity noise causes an exponential increase in the temperature with a rate of

$$\Gamma_i = \pi^2 \nu_i^2 S_k(2\nu_i) \tag{6.4}$$

where again ν_i refers to the oscillation frequency of the atoms in the i^{th} dimension. The equation for $\left\langle \dot{E} \right\rangle$ is proportional to the energy because the force exerted on the atoms as a result of the fluctuations increases as the square of the distance from the center of the trap. The dependence on 2ν rather than ν is expected since this is a parametric heating process. It is interesting to point out that the heating rate is proportional to ν^2. Any noise component at a high frequency can lead to an extremely high heating rate.

Intensity noise can be eliminated or at least suppressed by the addition of a feedback circuit or noise eater as discussed in Chapter 4. However, we have found that our feedback loop performs differently over the course of the dynamic range of trap depths. The intensity noise on the laser might be different for different trap depths. To study this we have taken Fourier spectra at several trap depths. For each spectrum the laser power was a constant 19 W; the trap depth was decreased by decreasing the RF power sent to the AOM in the YAG optical train. From the Fourier spectra and equation (6.4) we can estimate the heating rates. Figure 6.1 shows a typical set of power spectra. For both of these the trap depth was 600 μK. The top spectrum corresponds to the z-axis; the bottom corresponds to the x-axis. The data was taken for a range of trap depths and is summarized in Table 6.2.

Comparing Table 6.1 and Table 6.2, it is clear that intensity noise is a problem. As mentioned above, the feedback circuit performs differently for different values of the trap depth. Therefore optimizing the circuit for the best noise suppression at one range

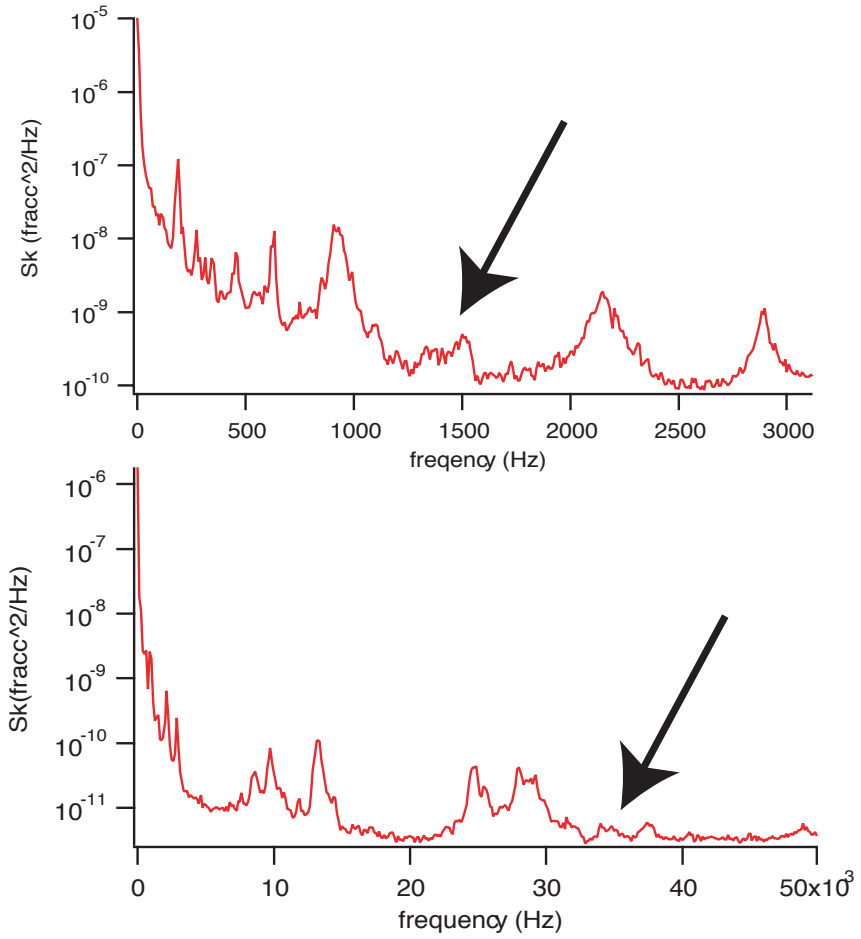

Fig. 6.1.— Power Spectra for the YAG at full trap depth. Arrows designate $\nu = 2\nu_{x,z}$

of frequencies often makes the performance worse at another range. The solution for this is to use two AOMs in the optical train. The first AOM would serve to stabilize the intensity via a feedback loop; the second AOM would provide the means for lowering the trap depth. This new apparatus has been constructed but not yet installed. While this will provide excellent noise suppression, it will come at the cost of laser power and thus will lower the maximum attainable trap depth.

Though there is work to be done on remedying the intensity noise, we have made a great deal of progress. We have designed a better feedback circuit (see Appendix C).

U	ν	S_k	$\Gamma(1/sec)$	$\langle E \rangle_{evap}$ (μK)	$\langle \dot{E} \rangle$(μK/sec)
600	735	3.98e-10	0.002	180	0.360
600	18400	4.35e-12	0.014	180	2.52
400	600	5.3e-10	0.002	120	0.240
400	15300	2.3e-11	0.054	120	6.48
100	300	7.5e-8	0.067	30	1.99
100	7500	2.96e-11	0.016	30	0.48
50	210	1e-7	0.044	15	0.652
50	5257	1.8e-10	0.05	15	0.75

Table 6.2: Summary of heating rates from laser noise. The high heating rate at U = 400 μK demonstrates the point that noise at a high frequency can yield an exceptional heating rate.

The regulated versus nonregulated power spectrums are shown in figure 6.2.

We have also changed how the feedback loop is implemented. In the work described by (Newell, 2003), the feedback circuit monitored a third order beam from the holographic diffraction grating. For reasons not understood, the noise characteristics for each of the diffracted orders is not correlated. By monitoring the third order, the feedback circuit was adding noise to the first and zeroth orders. To fix this, the feedback circuit is now monitoring the zeroth order. This does a great deal to suppress the low frequency noise in the zeroth order beam(see figure 6.3), but still adds noise to the first order. In figure 6.3 both spectra were taken of the zeroth order beam from the diffraction grating. The arrow designates the spectrum taken when the stabilization was applied to the 3rd order beam from the diffraction grating. As of now, we have no solution for this source of intensity noise.

6.3.3 Pointing Stability

Atoms in the HAT can also be heated as a result of laser-beam-pointing noise. This can be a problem inherent to the laser or can be a result of mechanical oscillations

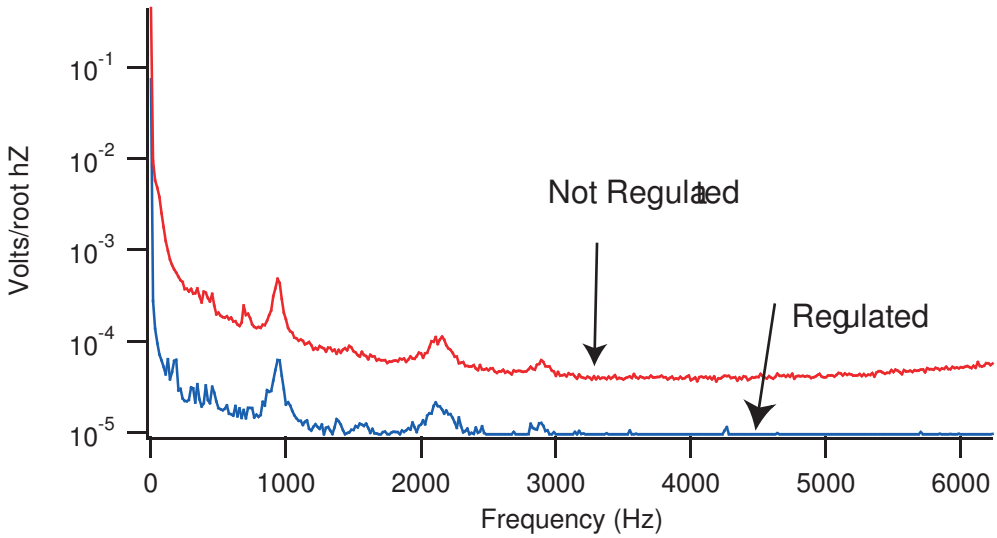

Fig. 6.2.— YAG Power Spectra showing the noise suppress when feedback is applied.

in the optical components. The equations governing the heating rates are once again described in (Savard *et al.*, 1997) and (Gehm *et al.*, 1998). These papers give a heating rate due to pointing instability to be

$$\left\langle \dot{E} \right\rangle = \frac{\pi}{2} M \omega_x^4 S_x(\omega_x) \tag{6.5}$$

where $S_x(\omega)$ is the power spectrum of position fluctuations of the trap center. The heating from pointing instability is independent of energy, thus heating of this type does not cause an exponential increase in the temperature as does heating from intensity noise.

We measured the pointing stability of our optical train as shown in figure 6.4. We place a slit in the focal plane of the last lens. This corresponds to the position of the atoms. The photodiode signal after the slit is very sensitive to any movement of the beam on the slit. Before the measurement, we moved the slit a calibrated amount to get a relationship between movement of the beam at the focal plane and the generated photodiode current. This calibration was used to scale the amplitudes of the power

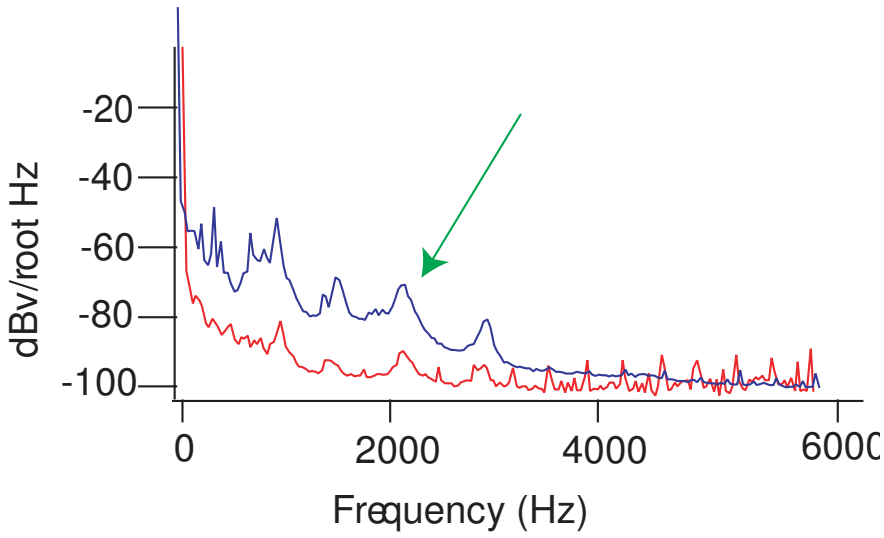

Fig. 6.3.— Suppress of intensity noise by stabilization of the 0^{th} order diffracted beam.

spectra shown in figure 6.5b). Power spectra comparing slit open to slit closed is shown in figure 6.5 a). From figure 6.5 we would conclude that there is little pointing instability in our set-up. The calculated heating rates are summarized in table 6.3.

The heating rates listed in Table 6.3 are much less than the estimated rates in Table 6.1. In conclusion, the heating rates associated with pointing instability do not account for the heating rates present during evaporation.

6.3.4 Torque Heating

After measuring the pointing stability of the optical train, we have concluded that at the atoms, the YAG has good pointing stability. It is possible, however, for the position of the focus to be fixed yet the beam to rotate about the focus. If this was the case, the microtraps would also be rotating an angle, θ, about their center. This would be another possible source of heating which we have named torque heating. A complete derivation of torque heating is given in Appendix E, but I will give the major

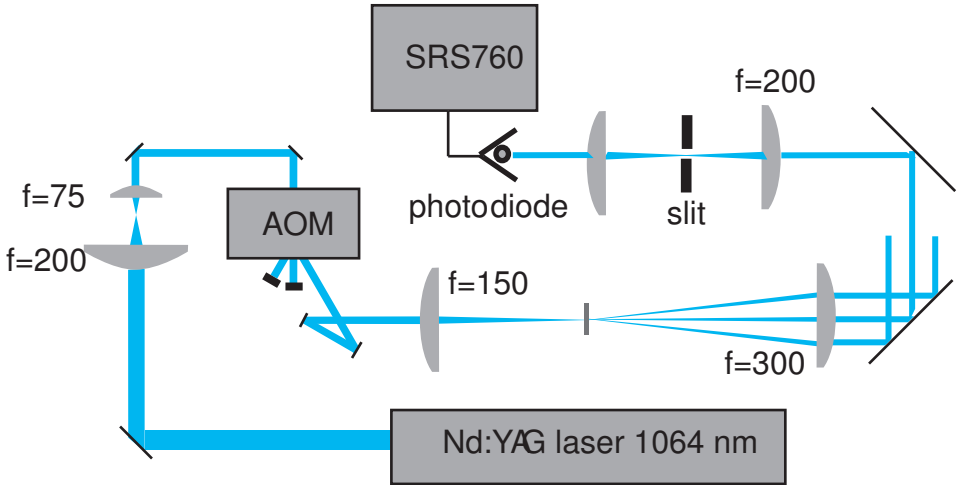

Fig. 6.4.— Optical setup for measuring pointing instability.

results here.

Like intensity noise, the change in energy due to torque heating is proportional to the average energy of the sample,

$$\left\langle \frac{dE}{dt} \right\rangle = \frac{\omega_x^4}{2\omega_z^2} \langle E \rangle \int \cos\omega_z\tau \cos\omega_x\tau\epsilon(\tau)\epsilon(t-\tau)\, d\tau. \tag{6.6}$$

Assuming that $\omega_z \ll \omega_x$, this can be written as

$$\left\langle \frac{dE}{dt} \right\rangle = \left(\frac{\omega_x^4}{2\omega_z^2} \right) S_k(\omega_x) \langle E \rangle \tag{6.7}$$

where $S_k(2\omega_i)$ is noise spectral density in units of radians^2/Hz. As done in Gehm *et al.*, we define a rate, Γ as

$$\Gamma = \left(\frac{\omega_x^4}{2\omega_z^2} \right) S_k(\omega_x). \tag{6.8}$$

We measured the torque heating with an apparatus similar to figure 6.4 except we remove the lens right before the photodiode and the slit at the focal plane of the first lens. If there is a long distance between the focus and the photodiode, the photodiode signal is very sensitive to the change in angle.

Trap Depth	ν_z	$S_x(\omega_z)$ μm^2/Hz	$\langle \dot{E} \rangle$ μK/sec
600	735	5.4e-7	4
400	600	5.4e-7	1.7
100	300	5.1e-7	0.105
50	210	5.3e-7	0.026

Table 6.3: Summary of heating rates from pointing instability.

By calibrating the angular movement of the beam with the signal seen on the photodiode and taking the power spectrum, we can apply the appropriate scaling to the power spectrum and extract heating rates due to torque heating. The heating rates at several values of the trap depth are given in table 6.4. A typical power spectrum and time constants for torque heating are given in figure 6.6

From table 6.4 we can conclude that the effects of torque heating have a negligible contribution to the heating rates seen in the HAT.

6.4 Heating from Collisions with background Rb atoms

The second source of heating mechanisms common in optical traps are those caused by collisions between the trapped atoms and the background vapor. These collisions can be especially troublesome in vapor cell experiments where the MOT is loaded from a background vapor.

The condition for heating due to collisions with the background is derived in references (Bali *et al.*, 1999) and (Beijerinck, 2000). In general, the condition that a collision will cause heating is that

$$U > \frac{1}{2} m (\Delta v)^2 \tag{6.9}$$

where $\Delta v = v_R \theta \mu / M$ is the change in the velocity of the trapped atom during the collision. We define μ is the reduced mass, θ is the incident angle of the background atoms prior to the collision, and v_R is the relative velocity between the trapped atom

and background atom. This equation assumes elastic collisions and a small angle approximation has been applied. If $U < (1/2)m(\Delta v)^2$ the collision would result in atom loss rather than heating. Thus equation (6.9) limits the range of collision angles that will lead to heating as opposed to just atom loss. If the incident angle, θ is less than a maximum angle, θ_{max}, then the atom will remain in the trap and will cause heating. If $\theta > \theta_{max}$ then the atom will be ejected from the trap.

6.4.1 Quantum Diffractive Collisions

We know that the angle θ must be small to cause heating rather than atom loss. Small angle collisions are treated with quantum diffractive theory if the maximum energy transferred via a diffractive collision is greater than the trap depth. Hence for shallow traps small angle collisions are often described by diffraction. The maximum energy transferred in a diffractive collision is

$$E_d = \frac{4\pi\hbar^2}{M\sigma} \tag{6.10}$$

where σ is the classical scattering cross section. For Rb-87, $E_d = 2.8$ mK which is greater than the maximum HAT trap depth of $U_{max} = 0.6$ mK, so it is valid to treat all heat causing collisions with the background as diffractive collisions.

The result of (Bali *et al.*, 1999) is an equation for the heating rate due to quantum diffractive collisions

$$\frac{dE}{dt} = 0.37 \times \gamma_c \frac{U^2}{E_d} \tag{6.11}$$

Trap Depth (μK	Γ (1/sec)	$\langle E \rangle$ (μK)	$\left\langle \dot{E} \right\rangle$ (nK/sec)
175	4.48e-5	52.5	2.3
100	5.45e-5	30	1.6
50	4.47e-5	15	0.67
10	3.37e-5	3	0.1

Table 6.4: Heating rate from torque heating for several value of the trap depth.

where $\gamma_c = \gamma_{bg}$ is the measured loss rate due to background collisions and E_d is given above to be 2.8 mK. For this calculation we assume that the collisions are all binary collisions between two Rb atoms (one trapped, one untrapped). Details about the measurement of γ_{bg} for the HAT are given in Chapter 3. This number is typically 1/3.5 sec = 0.286 /sec. At maximum trap depth, heating due to diffractive collisions is approximately 14 μK/sec. Note that this is over a factor of 5 improvement over (Newell, 2003), yet still a substantial source of heating. A summary of heating rates from quantum diffractive collisions at several trap depths is given in Table 6.5. At

Trap Depth (μK)	Heating rate (μK/sec)
600	14.1
400	6.26
100	0.392
50	0.098
10	0.004

Table 6.5: Summary of heating rates from quantum diffractive collisions.

large values of the trap depth, the heating due to quantum diffractive collision is much larger than the estimated heating due to intensity noise. At shallower trap depths the estimated heating from intensity noise is larger.

6.4.2 Secondary Collisions

As discussed above, if the energy transfer in a collision is greater than the trap depth, the collision will cause atom loss, not heating. This is not true, however, for the case of collisionally thick clouds (Beijerinck, 2000). The impacted atom will still leave the cloud, but as the atom leaves there is a finite chance that there will be a secondary collision with another trapped atom on the way out. Energy is transferred to the second atom in the collision, but the atom does not have enough energy to leave the trap. Rather, the second atom stays in the trap and the excess energy is distributed

amongst the other trapped atoms in the form of heat. This is of concern in the HAT because the densities are so high.

The collisions are studied in detail in (Beijerinck, 2000). The major result of that paper is an equation for the heating rate

$$\frac{dE}{dt} = 153nk/s\left(\frac{100s}{\tau^p}\right)\times\left(\frac{\langle nl\rangle}{10^{15}m^{-2}}\right)\times\left(\frac{87}{M}\right)\times\left(\frac{U}{1mK}\right)^{1/2}\times\left(\frac{E^s_{ref}}{1.36mK}\right)^{-5/6}\times\left(\frac{E^p_{ref}}{17.5mK}\right)^{1/6} \tag{6.12}$$

where τ^p is the measured lifetime due to primary collisions, $\langle nl\rangle$ is the average column density, E^s_{ref} is the energy transferred between two Rb atoms during a secondary collision, and E^p_{ref} is the energy transferred between two Rb atoms during a primary collision. The values of E^s_{ref} and E^p_{ref} for Rb-Rb collisions are equal and are given in (Beijerinck, 2000) to be 1.36 mK.

Beijerinck also discusses the appropriate column density for an asymmetric potential, such as seen in the HAT. For the case that the transverse oscillation frequency is much greater than the axial frequency,

$$\langle nl\rangle = 0.866\times\frac{\pi}{2}n(0)l_r \tag{6.13}$$

where l_r is

$$l_r = \sqrt{\frac{kT}{(2\pi\nu_r)^2M}}. \tag{6.14}$$

The corrected column density for a typical evaporation set and calculated heating rates are shown in Table 6.6.

The heating rates shown in Table 6.6 are overall lower than those of diffractive collisions in Table 6.5, except at shallow trap depths. It is important to note that the heating rates due to secondary collisions decrease as $NU^{1/2}$, while the heating rates due to quantum diffractive collisions decrease as U^2. As seen in figure 6.7, at a trap depth of approximately 40 μK heating from secondary collisions dominate heating from quantum diffractive collisions.

Above I discussed possible heating mechanisms in optical traps, estimated the heating rates for these heating mechanisms, and discussed how the measured heating rates change during evaporation in the HAT. These heating rates were put into context by Table 6.1. The rates in 6.1 were estimated by our evaporation model as the minimum heating rates necessary to cause the additional atom loss measured in the experiment but not predicted by standard evaporation dynamics. Based on Tables 6.2 - 6.6, we can draw some conclusions about which heating mechanisms dominate. At large trap depths, the dominate heating mechanism is quantum diffractive collisions. At low trap depths, heating from laser intensity noise and secondary collisions in the collisionally thick microtraps dominate.

6.5 Measuring Heating Rates via Recompression

In this section I will describe a method for direct measurement of the heating rates in the HAT. As discussed previously, in evaporation heating mechanisms can be disguised as a loss mechanism because the temperature will decrease until T=U/10, but in the presence of the heating mechanism more atoms will be ejected in the process. To directly measure the heating rates we would need to "shut off" evaporation. This could be achieved by creating a condition in which $T \ll U/10$. In this scenario heating mechanisms increase the temperature until $T \approx U/10$ and evaporation would be triggered. This is exactly the condition that occurs after evaporation and recompression in

Trap Depth	n ($1/cm^3$)	l_x (nm)	nl (cm^{-2})	Heating Rate (μK/sec)
600	3.1e14	654	2.8e10	0.619
400	2.7e14	654	2.4e10	0.433
100	2.0e14	654	1.77e10	0.163
50	1.67e14	654	1.5e10	0.096
10	9.9e13	654	8.8e9	0.025

Table 6.6: Summary of heating rates for Secondary collisions

the HAT. Recall in chapter 6 that atomic temperatures after recompression were approximately 9μK while the trap depth is 600μK. In this section we will use evaporation followed by recompression to directly measure the heating rates in the HAT.

6.5.1 Results

We performed a number of evaporation and recompression sequences. Each trial we would ramp the trap depth down to $U_b = 5$ μK then recompress to a varied value of U_t. We then measure the temperature as a function of time and apply an appropriate fit function to determine the heating rate.

If the heating is associated with quantum diffractive collisions or intensity noise on the laser, the temperature will increase linearly with time and a linear fit function is appropriate. If the heating is caused by secondary collisions a more sophisticated fit function is necessary due to the temperature dependence in the $\langle nl \rangle$ term. I will give the result here, but a complete derivation is found in Appendix D. The fit function describing secondary collisions is

$$T(t) = \sqrt{T_0^2 + \frac{2}{3}\dot{Q}T_0 t}. \tag{6.15}$$

Table 6.7 shows the results of our measurements, the theoretical values for quantum diffractive collisions and secondary collisions, and a reminder of the heating rates

U_t	n ($1/cm^3$)	l_x (nm)	$\langle nl \rangle$ ($1/cm^2$)	Theory dE/dt_{qd}	Theory dE/dt_{second}	Laser Noise dE/dt	Measured dE/dt
600	8.8e14	240	2.9e10	14	0.642	2.5	31.5
400	1.5e15	207	4.2e10	6.26	0.758	6.48	13.2
100	3e14	334	1.4e10	0.392	0.126	1.99	0.990
50	2.4e14	414	1.35e10	.098	0.086	0.990	1.38

Table 6.7: Theoretical and measured heating rates for different trap depths and column densities. All heating rates are in units of μK/sec.

due to the intensity noise on the YAG laser. By comparing measured heating rates after recompression (the last column in table 6.7) with the modeled heating rates during evaporation, (table 6.1) it seems that the heating rates during evaporation are overall higher than after recompression. In addition to this discrepancy, a larger mystery remains: we are unable to explain the large heating rate at full trap depth. At this point the dominate heating mechanism should be quantum diffractive collisions, all other heating mechanisms are negligible.

Table 6.8 summarizes our study of heating rates. The predicted heating rate is the quadrature sum of the expected heating rates from secondary collisions, intensity noise, and quantum diffractive collisions. Overall these mechanisms are able to account for our measured heating rates. At large trap depths, quantum diffractive collisions dominate, though we cannot explain why our measured rates are not in better agreement with the prediction of Bali *et al.* At shallow trap depths the dominate heating mechanisms are secondary collisions and intensity noise. In the next section we will use this information to modify the model so to include heating due to these mechanisms.

6.5.2 Inclusion of Heating Rates into Evaporation Model

We can now reconfigure the model to include the heating rates from quantum diffractive collisions and secondary collisions. This sets a lower limit on the effects of heating in the HAT. Heating from laser noise was neglected for simplicity. Recall that

Trap Depth	Predicted heating rates	Measured heating rates
600	14.2	31.5
400	9.04	13.2
100	2.03	0.99
50	0.76	1.38

Table 6.8: Summary of heating rates. All heating rates are in units of μK/sec.

our model for evaporation was a sequence two steps: rethermalization and lowering the potential. We will now change the model to have three steps: rethermalization, lowering the potential, and finally addition of the heating mechanism. As before, this three step sequence is cycled many times. The result is shown in figure 6.8. The arrows point to the theory curve which includes heating from quantum diffractive collisions and secondary collisions. With this modification the theory does a much better job predicting the atom loss and thus the phase space density. The additional atom loss at the end of the evaporation cycle is most likely a result of intensity noise on the YAG laser.

It is important to note that with the inclusion of heating due to quantum diffractive collisions and secondary collision, the predicted phase space density never reaches 2.6, the phase transition to Bose Condensation. Based on this, we conclude that the presence of the heating mechanisms in the current set up prevents us from attaining quantum degeneracy.

While heating mechanisms are a problem in our experiment, we have made vast improvements towards suppressing the heating due to intensity noise and quantum diffractive collisions. Since the work of (Newell, 2003), we have suppressed quantum diffractive heating by a factor of 5. This was done by improving the vacuum. We have also done much work on improving the intensity noise on the YAG. The remaining laser noise can be remedied by the use of a second AOM whose purpose is to solely be a "noise eater". The current AOM would be used for adjusting the trap depth during evaporation. The heating due to background collisions is a much harder problem to fix. The possible solutions are to increase the initial number of atoms loaded into the HAT so that during evaporation we can tolerate the additional loss due to diffractive heating, make further improvements to the vacuum, or load the MOT from an atomic beam rather than the background vapor. Regarding the vacuum, most of the background is

Rb which is needed to trap large number of atoms in the MOT and the HAT. Neither of the other two solutions are very practical at this time.

Lastly, it is important to point out that while these heating mechanisms may have prevented us from getting BEC, they have not prevented us from producing the high density mesoscopic clouds discussed in Chapter 6. The heating mechanisms will have no effect on our current work with Rydberg atoms, most importantly these heating mechanisms will not effect our ability to produce a dipole blockade.

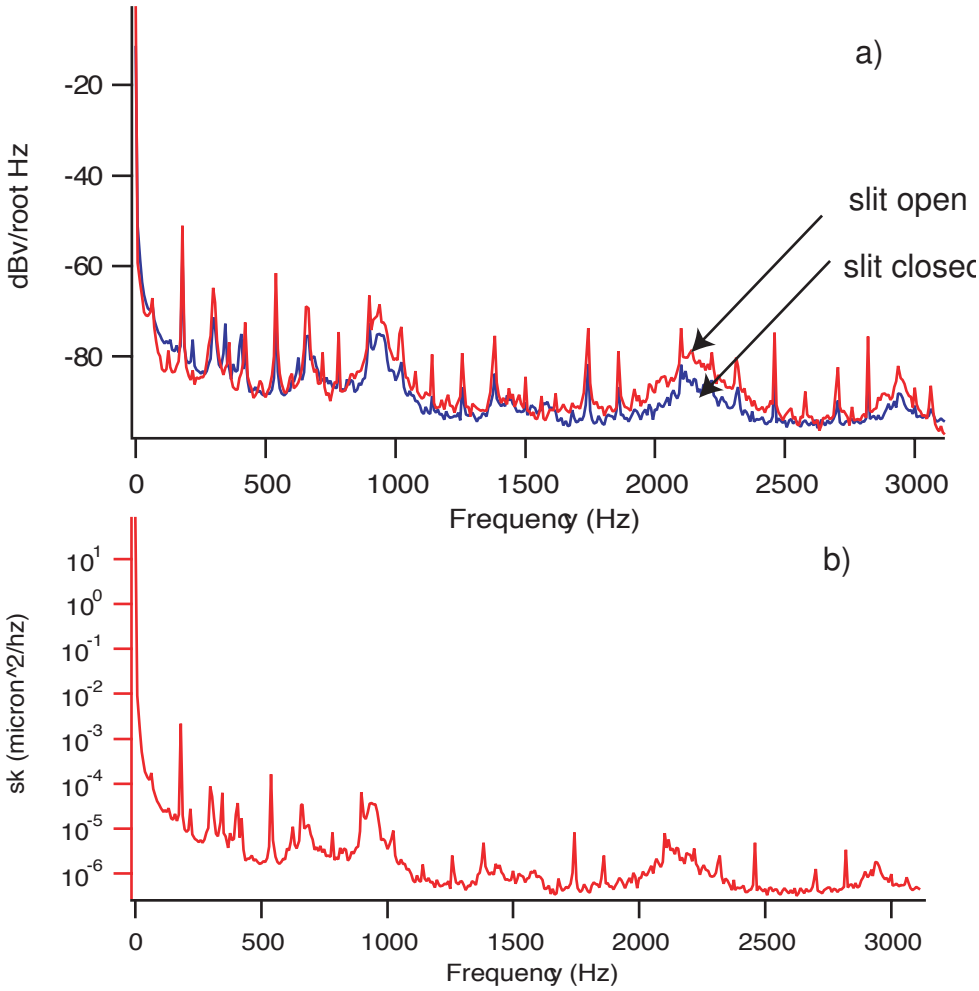

Fig. 6.5.— Pointing Stability of the optical train of the YAG. a)Power spectra for slit open versus slit closed. There is little difference. b)Frequency spectrum from pointing instability

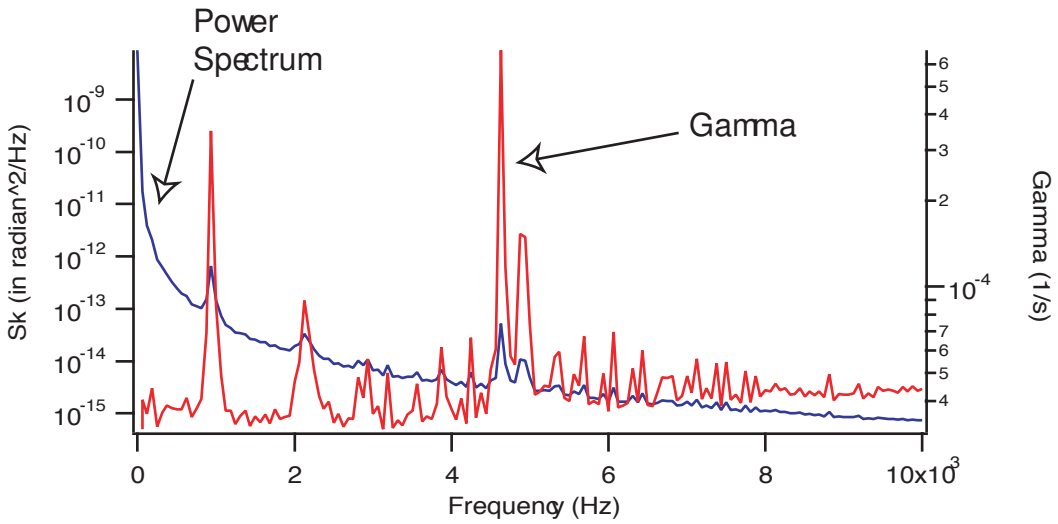

Fig. 6.6.— Power spectrum of torque heating.

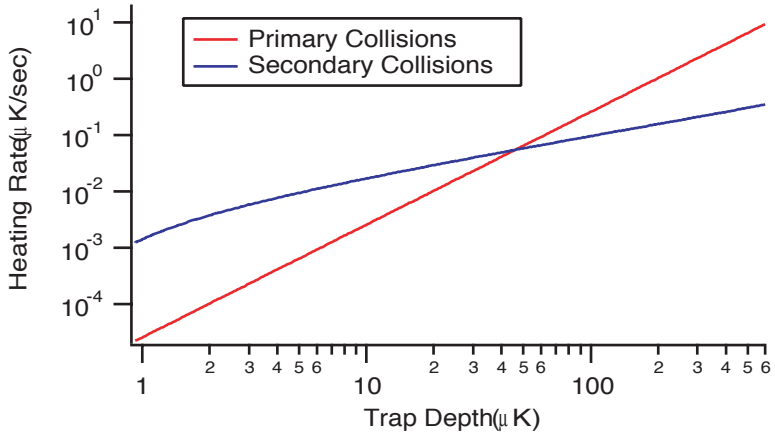

Fig. 6.7.— Diffractive heating and secondary heating as a function of trap depth.

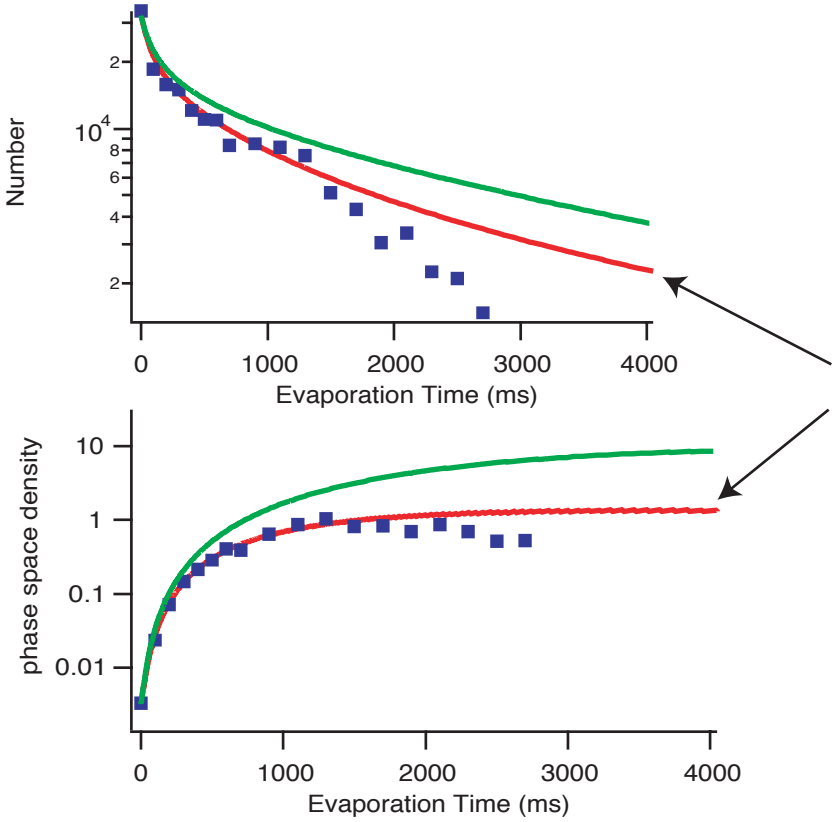

Fig. 6.8.— Inclusion of the heating due to quantum diffractive collisions and secondary collisions into the model for evaporation help make theory (solid line) and experiment (squares) agree. The arrow points to the theory curve which includes the heating mechanisms.

Chapter 7

Experiments with Rydberg Atoms

7.1 Introduction

Experiments with cold Rydberg atoms can be divided into two categories: those which take place above the ionization limit and those that take place below the ionization limit. Experiments at NIST, Rice, Michigan, and Virginia, to name a few, have excited cold atoms to high n states then have proceeded to make a cold Rydberg plasma. Much research has been done to understand the dynamics of the cold plasma. As a result, many interesting results have been uncovered.

The other category of Rydberg research, experiments below the ionization limit, has been deeply affected by the prospects of using interactions between cold Rydberg atoms to do quantum computing and quantum manipulation (Jaksch *et al.*, 2000) (Lukin *et al.*, 2001). Key to this is the concept of blockade, where a single atom at a time is excited from an ensemble. An important current goal is to demonstrate a complete dipole blockade. In Chapter 5 I discussed the prospects of seeing a complete blockade in one mictrotrap of the HAT. After evaporation and recompression, the dimensions of the HAT (5.6 μm x 250 nm x 250 nm) are ideal for demonstrating a total blockade because it is possible to make a Rydberg atom which has a range

(radius) of influence larger than the trap size. This means that if one atom in the microtrap is excited to a Rydberg state via a narrowband laser, the electric field from that atom would be sufficient to alter the energy levels of all the other atoms in the ensemble so that the narrow band laser no longer was coupled to the Rdyberg state. Thus, no other Rydberg atoms could be made. Total Rydberg blockade has not yet been demonstrated.

Recently, two groups (Tong *et al.*, 2004) and (Singer *et al.*, 2004) have seen evidence for suppression of Rydberg atom excitation. It is important to make this distinction: suppression demonstrates that fewer Rydberg atoms are excited than expected by classical theory; blockade suggests the excitation of one, and only one, atom into a Rydberg state. Both groups used a standard MOT as the source for making the cold Rydberg atoms. In this case the excited Rydberg atom's range of influence is much less than the size of the MOT. This allows for multiple excitations, but the number of excitations to the Rydberg state will be smaller because the range of influence around each Rydberg atom prevents neighbors from being excited.

Before discussing our work, I will briefly report on the state-of-the-art in the field. In section 7.1.2 I will give a summary of the experiment described in this chapter.

7.1.1 Summary of Related Work

The Conneticut group, (Tong *et al.*, 2004), reported the Rydberg suppression by doing the excitation via a pulse UV laser resonant with the 5s to np Rydberg state. The suppression was caused by the long-range van der Waals potential ($V_{vdW} \sim C_6/R^6$). After the Rydberg excitation a 1500 V/cm electric field was applied to ionize the Rydberg atoms. The ions were detected by a microchannel plate detector (MCP). This procedure was implemented for three different n states. The van der Waals coefficient $\sim n^{11}$, therefore it is expected that the suppression would be greater for high values

of n and much less for lower n-states. This group models the Rydberg excitations by solving the Bloch equations with the inclusion of an mean field energy level shift do to the Rydberg-Rydberg interaction. A factor α contains the average frequency shift due to the Rydberg interaction and the peak density of excited atoms, and alpha is scaled to fit the experimental data to the model. As expected, this work reports on strong suppression of excitation to n=70 and n=80 Rydberg states, and no suppression for n=30.

Similar results were reported in the work of (Singer *et al.*, 2004). In this work the excitation to the Rydberg state was done using a narrow band CW laser. Atoms were first excited from the $5S_{1/2}F = 2$ to the $5P_{3/2}F' = 3$ state with the MOT lasers; a second laser, a blue laser, was tuned to the $5P_{3/2}F' = 3$ to nl transition. The density of atoms in the ground F=2 state was adjusted using a depumper laser to purposely remove atoms from $F = 2$ and shelve the atoms in F=1. Prior to the Rydberg excitation, the MOT lasers are shifted to be on resonance with the $5S_{1/2}F = 2$ to the $5P_{3/2}F' = 3$ transition and the blue laser was pulsed on for 20 μsec. Like (Tong *et al.*, 2004), the detection is done by field ionizing the Rydberg atoms and detecting ions with an MCP. The MCP is calibrated by deducing the number of atoms lost from the fluorescence signal. The primary goal of this work was to study lineshapes of the Rydberg transitions, and the dependence of density and power on the number of Rydberg atoms produced. Rydberg spectra were taken for n=62 and n=82, and for each value of n the Rydberg spectra was taken in the low blue power regime (6 W/cm^2) and the high power regime (500 W/cm^2). At high power the group reports significant linebroadeing which they attributed to level shifts of the Rydberg states due to van der Waals interactions among Rydberg pairs. They also report saturation of the n=82 transition at a lower power than the saturation of the n=62 transition. This

was attributed to the onset of dipole suppression.

7.1.2 Summary of this work

In this chapter I will discuss on-going research of Rydberg atom production. I will first report on the production of 46d and 48s Rydberg atoms via both single photon excitation from the $5P_{3/2}F' = 3$ to np Rydberg state and two-photon excitation from the $5S_{1/2}F = 2$ to the 46d. To our knowledge, we are the first group to generate Rydberg atoms with a two-photon excitation. The two-photon process is preferable to the single photon excitation because in the two photon case the affects of the intermediate state are negligible. In the single photon excitation case the intermediate state has a finite lifetime allowing atoms to decay from the intermediate state without being excited into the Rydberg state. This is a source of decoherence in the system. For experiments such as Rabi flopping, the two photon process will be essential.

The detection of the Rydberg atoms is achieved by monitoring the MOT fluorescence. From the fluorescence signal, absolute loss rates, γ_1, due to the Rydberg atom excitation in the MOT can be extracted and plotted as a function of the laser power used to excite the Rydberg atoms. Saturation of the single photon excitation into the 48 s and 46 d states was observed. Weak saturation of the two-photon 46 d transition was also observed. The measured γ_1 at saturation for the single photon excitation to the 46 d state was approximately 25/sec which is surprisingly low given that the fundamental lower limit on the loss rate of Rydberg atoms from the MOT is given by the black body ionization rate which we have calculated for n=50 to be 290/sec. We would expect for a classical two-level system to measure a loss rate approximately half the black body ionization rate, because classically we could excite half of the MOT atoms into the Rydberg state. By measuring a lower loss rate than expected, it suggests that we are not exciting as many atoms to the Rydberg state as classically possible.

In section 7.4 I will discuss a model which has been generated to explain the loss rate of Rydberg atoms from the MOT. Included in this model is the effect of suppression of Rydberg excitation due to Rydberg-Rydberg interactions. We modeled Rydberg excitation in the MOT has a four level system: a ground state (g), an excited state (e), a Rydberg state (r), and a storage state (s). The purpose of the storage state is to account for the atoms lost from the Rydberg state due to transitions among n states and ionization, both a result of black body radiation. Since the excitations in the MOT are considered to be incoherent, we were able to model the Rydberg excitation as a set of three rate equations. At low laser power, our data closely fits the model when no suppression is present. This is expected because at low laser power the density of Rydberg atoms is low and the atoms are not closely enough packed to be influenced by neighboring Rydberg atoms. At high laser powers our data deviates from the no-suppression model. This deviation suggests that indeed, a suppression mechanism is present. The degree of deviation is extracted from the fit function, and from that we determined we were exciting Rydberg atoms with a range of influence of 4.8 μm, almost 50 times the classically calculated ($r \sim a_0 n^2$) size of a n = 50 Rydberg atom.

There are several features of this work which are novel compared to the previously mentioned work of (Singer *et al.*, 2004) and (Tong *et al.*, 2004). These include the ability to measure the absolute loss rate of Rydberg atoms from the MOT. By using the MOT fluorescence rather than an ion detector to measure losses due Rydberg atoms, our measurements are self-calibrated. As stated above, we demonstrate the first two-photon excitation of a Rydberg state. Others have demonstrated the one photon excitation to the Rydberg state. The two-photon transition is necessary for coherent manipulation of atoms. This excitation method will be necessary when exciting Rydberg atoms in the HAT since the heating due to the scattering of resonant light will eject large numbers of atoms trapped in the HAT. And finally, our detection system is unique in that we

use only the MOT fluorescence to detect the presence of Rydberg atoms.

The work presented here is our first efforts in making Rydberg atoms. This work is ongoing and is carried out by my co-workers in the lab. The ultimate goal to measure the absolute loss rate from the MOT due to Rydberg excitations for three n-states with the expectation of seeing greater suppression of Rydberg excitations at higher n-states because the potential scales as n^{11}. The next step will be to generate Rydberg atoms in the HAT in effort to produce a total van der Waals or dipole-dipole blockade.

7.2 Apparatus

The excitation to the Rydberg state is a two step process. We have demonstrated this excitation using two methods shown in figure 7.1: a single photon transition from the $5P_{3/2}$ F'=3 excited state, and a two photon transition from the $5S_{1/2}$F=2 state. In the single photon excitation from the excited state, atoms are excited into the $5P_{3/2}F = 3$ state via the standard trapping beams. The excited state fraction is approximately 0.23. For the two photon excitation, atoms are excited to a virtual level -1.2 GHz to the red of the $5P_{3/2}F' = 3$ state. We use a Toptica TA-100 at 780 nm to generate these photons. Using a Burleigh WA-1000 optical wavemeter, we use the piezo on the diode laser grating to tune the frequency. From the WA-100 we measure that the Toptica is stable to 98 MHz over 1 hour. Overall we have found the WA-1000 to have excellent long-term stability and no other stabilization is needed. Typically we adjust the piezo voltage every few hours to retune the laser to the proper frequency. The TA-100 can produce 500 mW of light at 780 nm. An IntraAction Corp. AOM is used to pulse the laser. After the AOM we can deliver 250 mW of light to the atoms. The Gaussian beam waist of this laser is 1.8 mm at the MOT cloud. Even though this laser is far detuned, it has a visible depumping effect on the MOT cloud.

The one photon excitation scenario is experimentally simpler than the two pho-

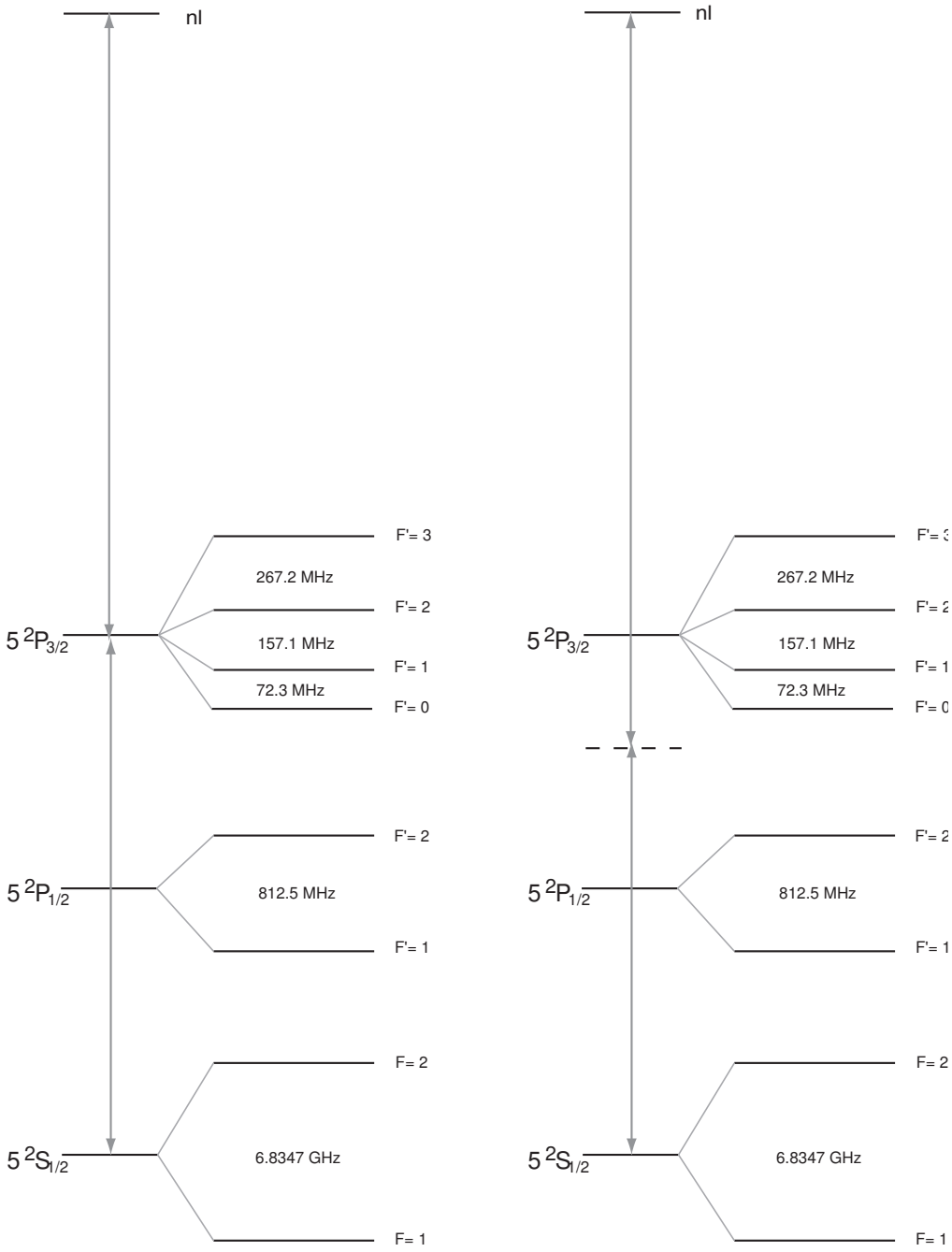

Fig. 7.1.— The left diagram shows a single photon excitation from the excited state to the Rydberg State. On the right is the two photon excitation from the ground state to the Rydberg state.

ton excitation, however, it suffers the drawback that the effects of the intermediate state are not negligible. Atoms in the excited $5P_{3/2}F' = 3$ state can decay back to the ground state thus broadening the Rydberg transition and contributing to decoherence in the system. In the two photon case, the intermediate state is a virtual state. Given sufficient blue laser power, the two photon case can be a coherent process. The requirement for a coherent process is that $\epsilon_2 > \Gamma_2$ where ϵ_2 is the 2-photon Rabi frequency and Γ_2 is the linewidth of the transition. A demonstration of Rabi flopping could only be done in a 2 photon excitation scheme.

In both the one photon and two photon cases, the n = 5p to n = 50 is $\approx \lambda_b$=480 nm photon. The blue light is achieved by frequency doubling a 960 nm laser. The 960 nm laser is a Sacher Tiger Laser which can provide 500 mW at 960 nm. The Tiger laser is frequency stabilized by the use of a homemade confocal stable cavity. The cavity is temperature stabilized; by adjusting the temperature of the cavity, the frequency of the red light can be adjusted which in turn adjusts the frequency of the blue light. Typically the blue output power is 20 mW with a laser linewidth of approximately 10 MHz. The blue light is transported to the trapping chamber via an Oz Optics polarizing maintaining (PM) fiber. We have demonstrated 14 mW of blue light delivered to the atoms.

The optical train for the blue laser in on trapping table is shown in figure 7.2. This imaging system is capable of producing an 11 μm Gaussian waist at the MOT cloud. This will be useful for production of Rydberg atoms in the HAT. For studies of Rydberg atom production in the MOT, we move the last lens so that we have a 1 mm beam waist at the MOT cloud.

The detection of the Rydberg atoms is done by monitoring the fluorescence of the MOT cloud. Depending on the amount of blue light used, we have seen the MOT fluroescence decrease by almost two orders of magnitude when tuned to a Rydberg

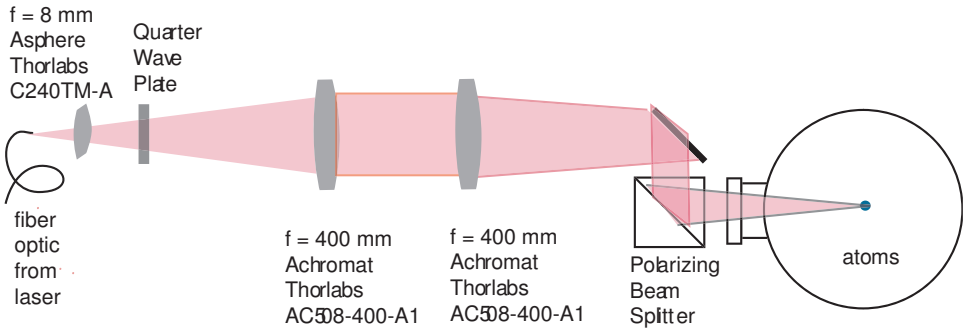

Fig. 7.2.— Optical Train for blue light

resonance.

7.3 n=50 Spectra

7.3.1 Single Photon 46 d state

Using the apparatus detailed above, we have produced Rydberg atoms with principal quantum numbers of approximately n=50. We have studied the 46 d state and the 48 s state. The 46d state was generated by both single photon excitation and two photon excitation.

The first spectrum we studied was the single photon excitation of the 46 d-state (see figure 7.1). A sample spectrum is shown in figure 7.3. The laser is scanned across the resonance peak by changing the temperature of the stable cavity. The MOT cloud fluorescence is recorded as a function of frequency. The x-axis in this figure is the frequency of the red (960 nm) laser; the y-axis is proportional to the number of atoms in the MOT cloud. The two peaks represent the 46 $d_{5/2}$ at $\lambda_{IR} = 960.6511$ nm and the 46 $d_{3/2}$ at $\lambda_{IR} = 960.6513$ nm separated by the fine structure splitting. For this state the splitting is 120 MHz in the blue or 60 MHz in the IR. In this scan we measure 57

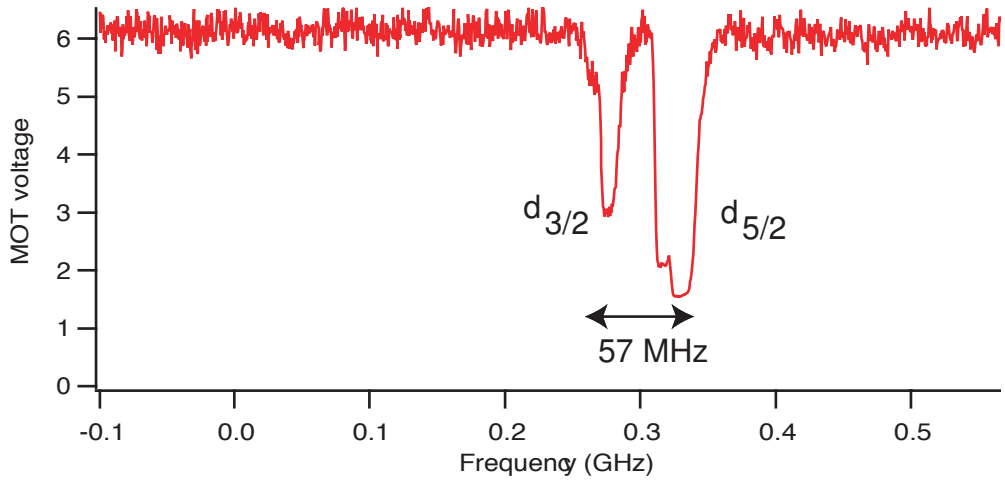

Fig. 7.3.— 46d spectrum

MHz (IR). We measure the linewidth of the $d_{3/2}$ transition to be 9.4 MHz (IR).

We have studied the lineshape of the 46 d as a function of power as shown in figure 7.4. Each $d_{5/2}$ peak was fit to Gaussian; the respective Gaussian radii are shown for each peak. As blue power increases we see the effects of power broadening. In the absence of saturation, the ratio of the $d_{5/2}$ to $d_{3/2}$ transitions should be 9:1.

We measure the loss rate due to the Rydberg atom production. The number of atoms in the MOT cloud is given by

$$\frac{dN}{dt} = L - (\gamma_1 + \gamma_0)\, N \tag{7.1}$$

where γ_0 is the typical loss rate seen in the MOT (due to laser induced collisions or background collisions) and γ_1 is the loss rate due to Rydberg atom production. In steady state we can write this as

$$\frac{1}{N} = \frac{\gamma_0 + \gamma_1}{L} = \frac{1 + \gamma_1/\gamma_0}{N_0} \tag{7.2}$$

where N_0 is the number of atoms in the MOT without any loss due to Rydberg atom formation, or in other words, γ_0 and N_0 are measured under the same conditions.

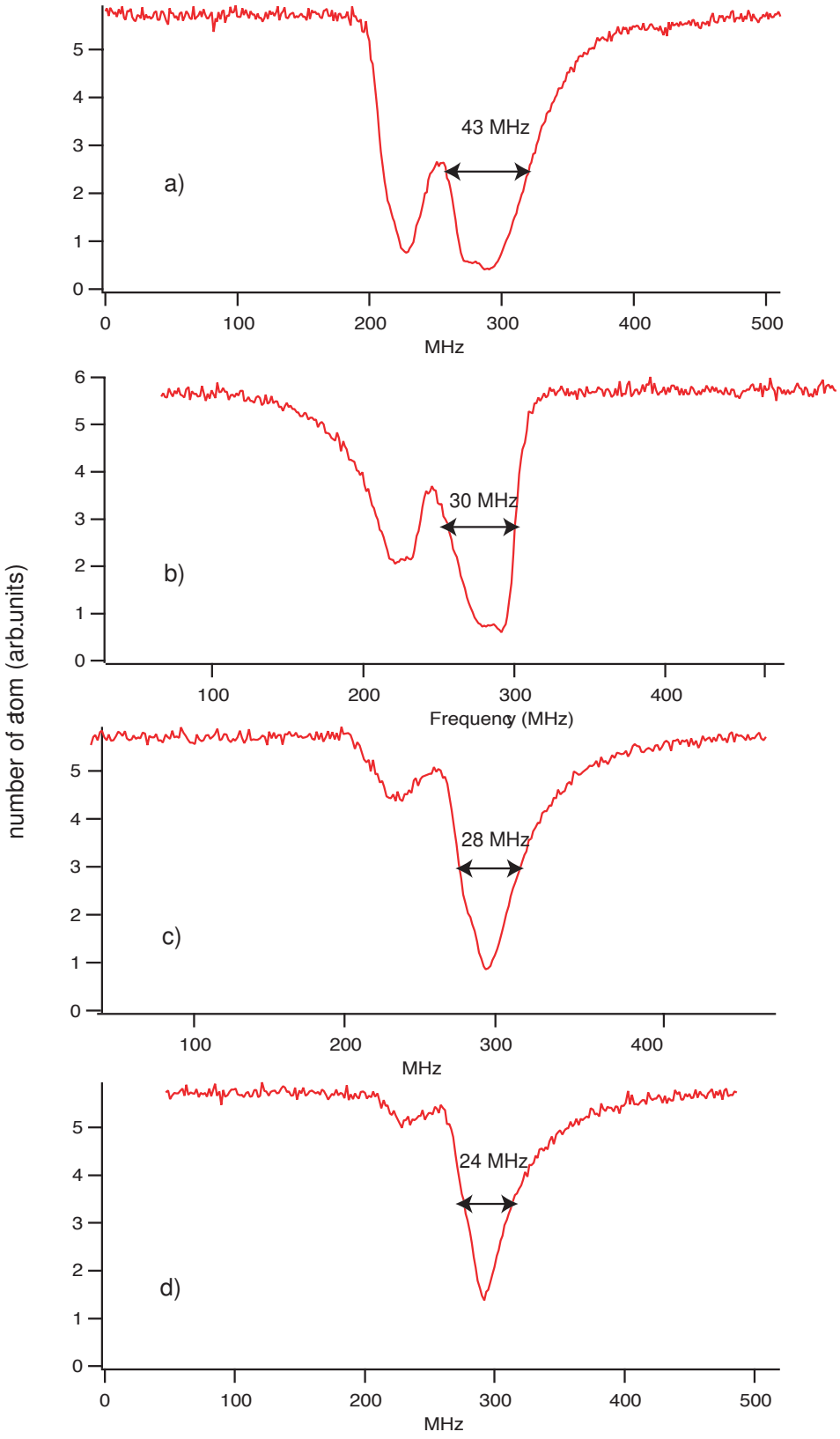

Fig. 7.4.— 46d spectra for various blue powers. a) 300 μW b) 94μW c)30μW d) 20 μW

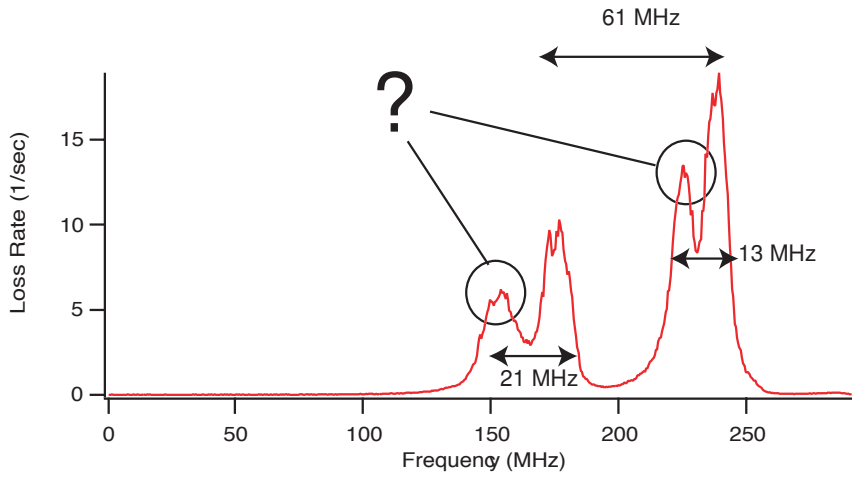

Fig. 7.5.— Loss rate due to Rydberg atom production for the singly excited 46d vs Frequency

Solving for γ_1,

$$\gamma_1 = \gamma_0 \left(\frac{N_0}{N} - 1 \right). \tag{7.3}$$

Figure 7.5 uses the above method to normalize the change in fluorescence due to Rydberg production in the 46 d single photon excitation case.

The linewidth of the spectrum in figure 7.5 is 12 MHz. Notice the doublet splitting inside both the $d_{5/2}$ and $d_{3/2}$ peak. It is a feature that we have not been able to account for its origins. The peaks emerge as blue power is increased; the space between the two doublets (13 MHz and 21 MHz respectively) does not change as a function of blue power. Since the frequency splitting is not a function of blue power, Autler-Townes (Teo *et al.*,2003) and laser induced AC stark shifts from the blue laser can be eliminated because both of those effects would show an increase in the frequency splitting as a function of increasing blue laser power. I can only speculate that the cause of these doublets is a misalignment of a laser field. It might be possible that the MOT lasers are misaligned so that some atoms have larger stark shifts than others which causes the

appearance of two sets of peaks. We have checked for stray electric fields by tuning the blue laser so that it would be resonant with a dipole forbidden transition such as the 47 p-state. In the presence of an electric field, this state might be allowed. Evidence of this was discussed in reference (Singer *et al.*, 2004). We were unable to observe an p to p or p to f Rydberg transitions, thus the present of a stray field is unlikely.

We have also studied the loss rate, γ_1, as a function of blue power. This is shown for the single photon excitation of the 46 d state in figure 7.6. We see a maximum loss rate of 25/sec.

We can calculate the Rabi frequency which causes this saturation. At a blue laser power of 5 mW and a blue beam waist of 1 mm, the intensity is $I_b = 0.31$ W/cm^2. The

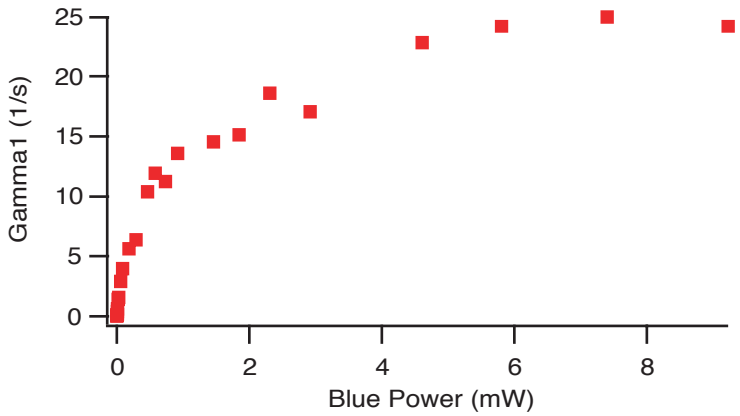

Fig. 7.6.— Loss rate due to Rydberg atom production for the singly excited 46d vs Blue power

Rabi frequency associated with the blue transition is

$$\epsilon^2 = \frac{\pi \alpha a_0 \lambda f I_b}{h} \tag{7.4}$$

where α is the fine structure constant and f is the oscillator strength of the 5 p to 50 d transition. The oscillator strength for the 5 p to 50 d is 2.71×10^{-5} (Walker, private communication). The ratio of the $d_{5/2}$ to $d_{3/2}$ is 9:1, so the oscillator strength

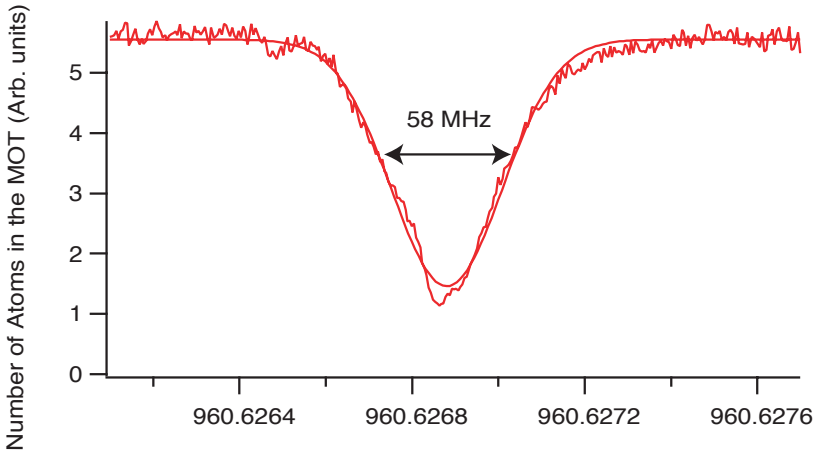

Fig. 7.7.— 48 s spectrum.

of the $9/10 \times 2.71 \times 10^{-5}$. Using $I_b = 0.3$ W/cm^2 and $\lambda = 480$nm, we calculate a Rabi frequency of 680 kHz $= 0.13\Gamma$.

7.3.2 Single Photon 48 s state

We have also studied the one photon excitation of the Rydberg 48 s-state. A spectrum is shown in figure 7.7. We have studied the linewidth of the transition as as a function of blue laser power (figure 7.8). Again, at large laser powers we see broadening of the transition. As seen for the 46 d transition, we see the appearance of an extra peak emerging at higher blue powers. It is frequency split 16 MHz from the original peak.

Using equation (7.3) we have calculated the loss rate due to Rydberg atom formation, and we have studied this as a function of blue laser power. This is shown in figure 7.9. As seen with the one photon 46 d transition, we are able to saturation the 48 s transition. The saturation power is about the same as with the 46 d, but the 48s

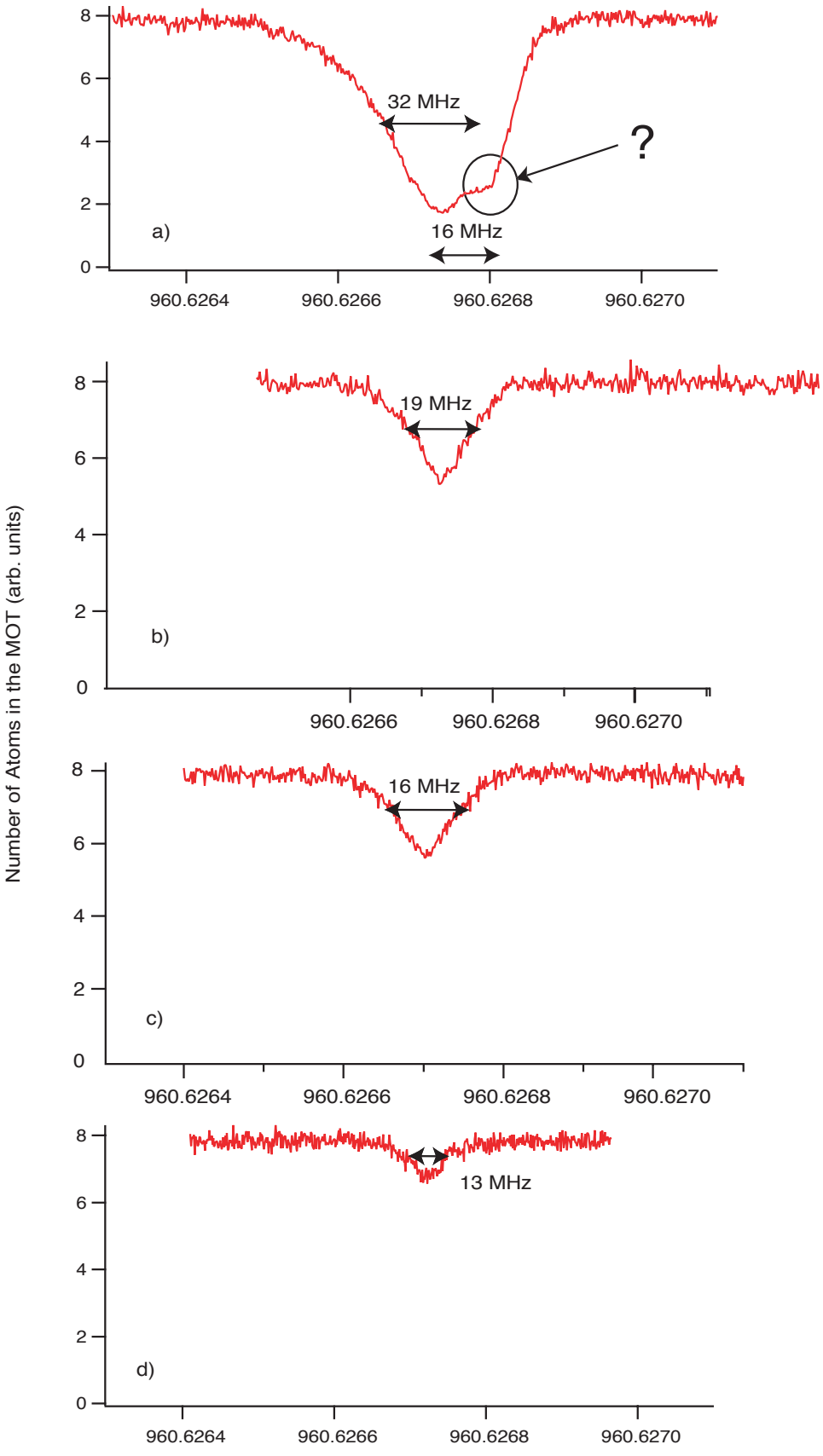

Fig. 7.8.— 48 s spectra for various blue laser powers. a) P = 600 μW b) 20 μW c) 12 μW d) 6μW.

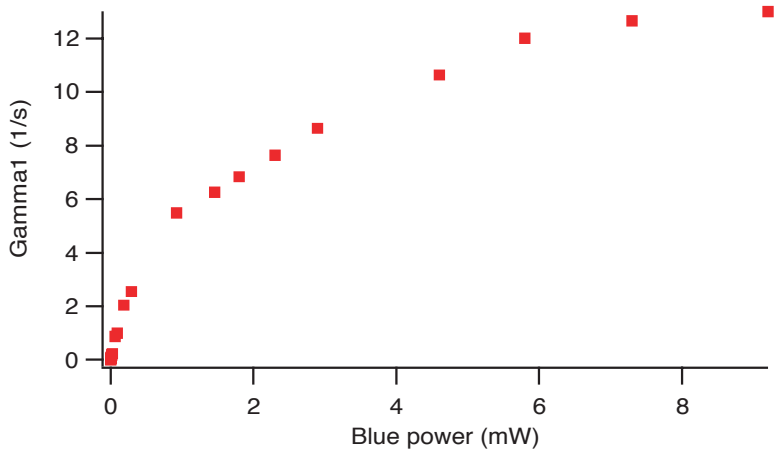

Fig. 7.9.— Loss rates due to formation of 48 s Rydberg atoms versus blue laser power.

saturates at a lower $\gamma 1$, $\gamma 1 \approx 12$/sec. The Rabi frequency at saturation for the 48 s transition is smaller because the oscillator strength is smaller (f = 3.84×10^{-6}). For P = 5 mW and w = 1 mm, hence, I = 0.3 W/cm2, we can using equation (7.4) to calculate a Rabi frequency of ϵ_b = 270 kHz = 0.045Γ.

7.3.3 2 photon Excitation of the 46 d state

We have also demonstrated 2 photon excitation of Rydberg atoms (see figure 7.1) from the ground F=2 state to the Rydberg state. The two photons come from the blue laser and an extra 780 nm laser which we call "Big Red". Big Red is tuned -1.2 GHz from the $5P_{1/2}$ F=2 to $5P_{3/2}$ F=3 transition. To ensure that the formation of the Rydberg atoms is due to the 2 photon transition from the ground state and not from a single photon excitation from an excited state, Big Red is pulsed on with a duty cycle, d. When Big Red is on, the trapping laser is turned off. Also, the Rydberg resonance occured 1.2 GHz from where it occured in the one photon case, giving the ultimate evidence that we are producing these Rydberg atoms via a two photon process. We leave the repumper on so to keep the F=2 level populated. If

Rydberg atoms spontaneously decay into the F=1 state this could mistakenly look like atom loss from the trap. Leaving the repumper on prevents this from happening.

We have studied the 2 photon 46 d transition as a function of both Big Red power and blue laser power. First I will show the functionality on Big red laser power. The Big Red laser has a 1.8 mm Gaussian beam waist at the atoms. The power can be varied from 30 mW to 268 mW. Sample spectra at various Big Red powers are shown in figure 7.10. Scaling all the γ_1 values in figure 7.10 to a blue laser power of 14 mW and a duty cycle of 1, we can summarize the results as shown in figure 7.11. We choose to scale to 14 mW because that is the maximum amount of blue laser light that we have available after taking into account the loss from the fiber and other optics. From figure 7.11 the maximum loss rate is approximately 15/s which is lower than the maximum loss rate measured in the one photon excitation of the 46d, $\gamma_1 = 25$/s. Also note the absence of the unexplained doublet that was present in the one photon 46d and the one photon 48 s. It is possible that we are not sensitive enough to detect this. Another possibility is that the MOT lasers are slightly misaligned and are responsible for Stark shifting some of the atoms more than others, causing the appearance of the two resonances.

The Rabi frequency associated with this transition is the two photon excitation given by

$$\epsilon_2 = \frac{\epsilon_r \epsilon_b}{\Delta} \tag{7.5}$$

where ϵ_r and ϵ_b are the Rabi frequencies of the red and blue lasers respectively and Δ = 1.2 GHz. Using a Big Red power of 200 mW and a Gaussian beam waist for 1.8 mm, the intensity is given by $I_r = 3.9$ W/cm^2. Likewise for 14 mW and a Gaussian beam waist of 1 mm, the intensity is $I_r = 0.9$ W/cm^2. From this we can calculate a two photon Rabi frequency, $\epsilon_2 = 590$ kHz $= 0.1\ \Gamma$. We have also studied the dependence of

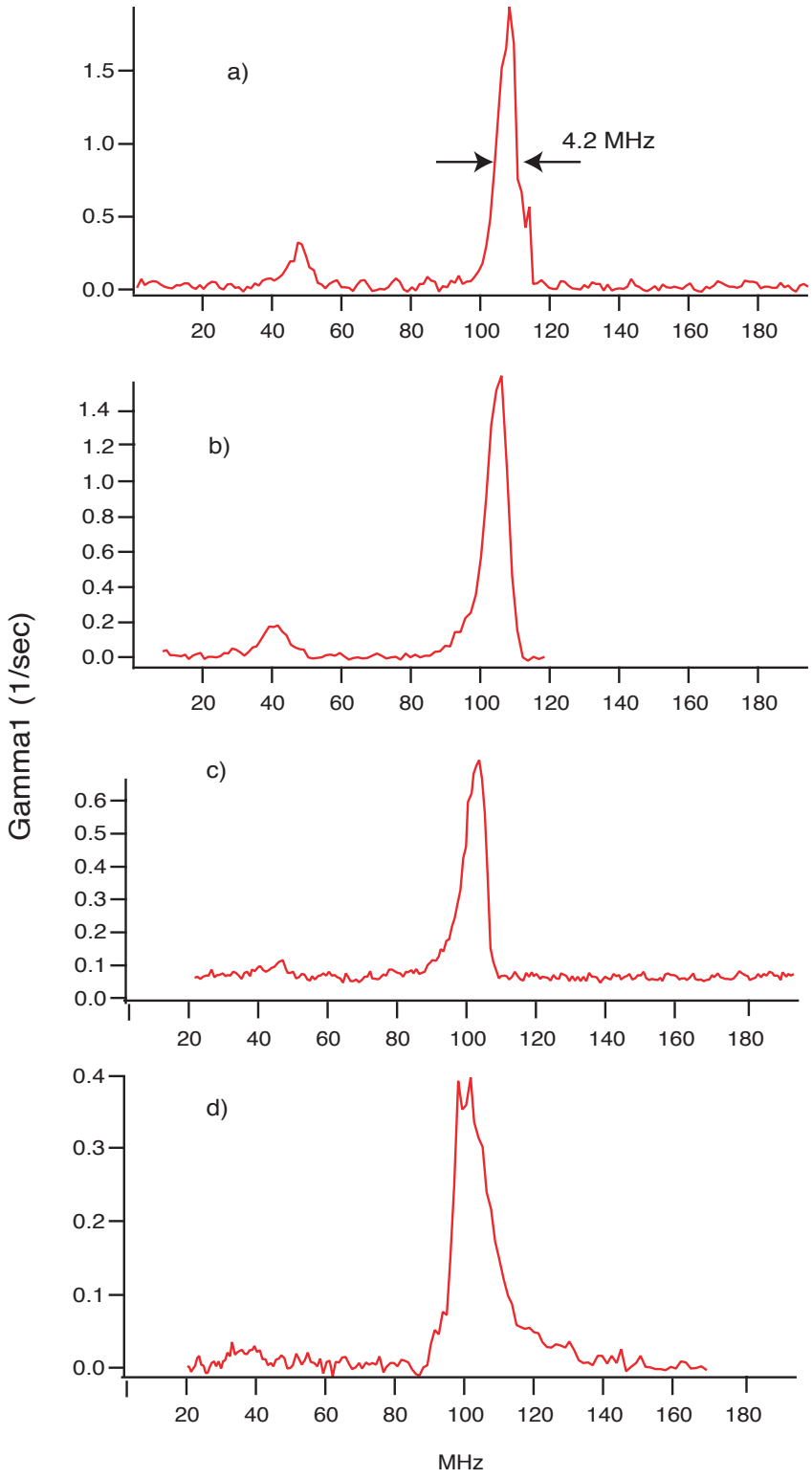

Fig. 7.10.— Loss rates versus frequency for the 2 photon transition to the 46 d state for various powers of Big Red a) P_{bigred} = 268 mW b) 142 mW c) 51 mW d) 31 mW.

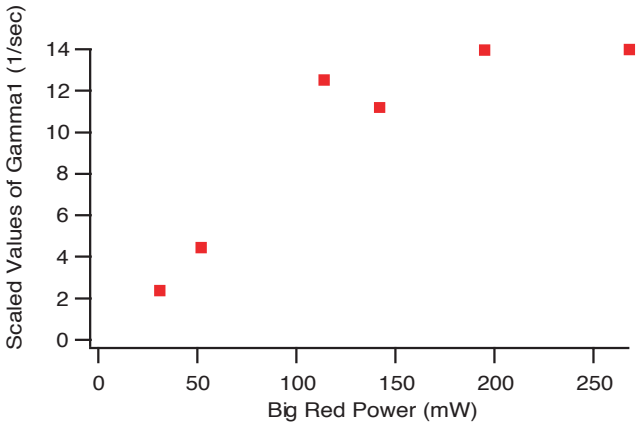

Fig. 7.11.— Loss rates versus Big Red power for the 2 photon 46 d transition. All loss rates are scaled to a blue power of 14 mW and a duty cycle of 1

the loss rate on blue power while the Big Red power is 270 mW. The data is shown in figure 7.12. For this data set we had insufficient blue power to saturated the 2 photon transition.

The Rabi frequencies at which we see saturation of the 46d state are approximately 700 kHz, regardless of the excitation method. The reason we measure a lower γ_1 for two photon excitation versus one photon excitation is most likely because the fundamental linewidth of the transition is narrower for the two photon case than the one photon case. In the two photon case, the fundamental linewidth of the transition given is

$$\Gamma_2 = \frac{\epsilon_r^2}{\Delta^2}\Gamma = 0.265\Gamma. \tag{7.6}$$

Experimentally, this means that the linewidth of the two photon transition is the linewidth of the blue laser. And since the linewidth of the blue laser is approximately 1.6 Γ, only a fraction of the blue photons are actually at the proper frequency to excite the two photon transition. Furthermore, since the linewidth of the 2-photon transition is greater than the 2-photon Rabi frequency, $1.6\Gamma > 0.1\Gamma$, the two photon transition is

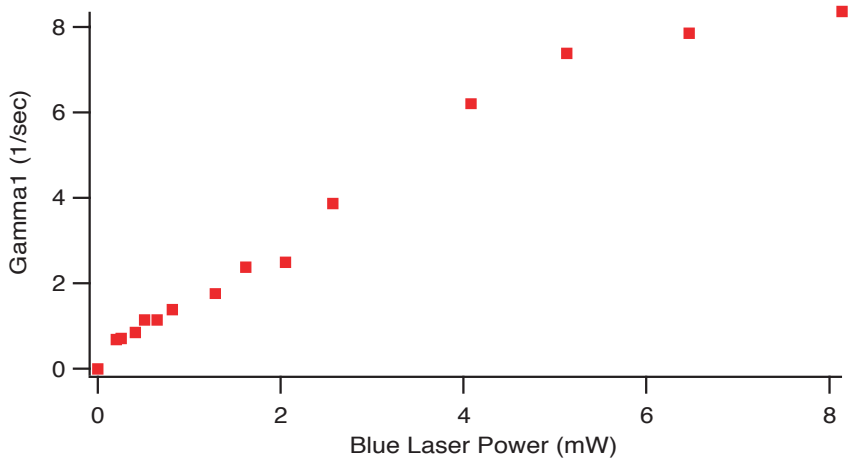

Fig. 7.12.— Loss rates due to 46 d two photon excitation as a function of blue laser power

incoherent. In our case, if the two photon linewidth was truly the linewidth given in equation (7.6) then our two-photon process would be close to being coherent.

For experiments in the MOT it is necessary to have large beams so that all atoms in the MOT see the same Rabi frequency. In the HAT, however, we can focus the blue laser to 11μm providing a large enhancement in our Rabi frequencies. This will increase the blue laser intensity to 7.4×10^3 W/cm^2. The 2-photon Rabi frequency is now 7.3 MHz = 1.2 Γ which shows promise for being able to coherently drive the transition.

7.4 Model

While this data is very interesting, it raises a very fundamental questions: why are the measured loss rates so low? What is causing the saturation? Another key to be answered is: are we seeing any evidence of dipole suppression? Since this is work in progress, the answers to these questions and many other questions change daily. Nonetheless, we did attempt to model the loss dynamics that occur when Rydberg

atoms are produced in the MOT and compare this with the loss rates we have measured. Below I will give the details for the model specifically designed to explain the saturation data for one photon excitation of the 46d state. We chose to apply the model to this set because of the significant level of saturation seen for this transition compared to the data for the two photon excitation which was only weakly saturated.

In the literature (Teo *et al.*,2003), (Singer *et al.*, 2004), and (Tong *et al.*, 2004), it is commonly suggested that the dominate loss mechanism is ionization from black body radiation. For n=50, the black body ionization rate is $\gamma_{bbi} = 290$/sec. Naively, for a classical two level system (ground state and Rydberg state) we should be able to transfer half of the MOT population into the Rydberg state, $N_{ryd} = 1/2\ N_{MOT}$. From this, one would expect that we would measure a loss rate half the value of the black body ionization rate, or in other words, in excess of 100/sec. This is surprising given that the maximum loss rates we have measured are approximately 25/sec. If other loss mechanisms are present, such as Rydberg-Rydberg loss mechanisms, our measured rates should be even higher. By considering only the effects of black body radiation we are putting a fundamental lower limit on the Rydberg loss rate. Considering the low loss rates that we have measured, the measurements would suggest that we are not exciting as many Rydberg atoms as we would classically expect and a suppression mechanism could be present.

As an attempt to understand the discrepancy in the measured loss rates and the expected loss rates, we have modeled the trap loss from Rydberg production via either the single photon excitation or the two photon excitation. As done previously in the literature, we have included the effects of dipole blockade as a factor limiting Rydberg excitation.

In the model the following assumptions were made. First, we assumed that the Rydberg density was low enough that the dominate loss mechanism is black-body

ionization from the black-body background radiation. Though other loss rates may be present, this loss rate represents a lower limit. Our second assumption is that we can model the system as a four level system. Figure 7.13 shows the four levels we use in our model. R_1 is the rate at which atoms are excited from the ground state, g, to the excited state, e; R_r is the rate at which atoms are excited from the excited state, e, to the Rydberg state r. The third assumption is that in the MOT transitions between the ground, excited, and Rydberg state are basically incoherent and can be described by rate equations. A formal treatment of the Bloch equations is not necessary. The fourth assumption is that once an atom has been excited to the Rydberg state, three processes are possible: spontaneous emission (at rate γ), stimulated emission, or ionization by black body radiation. The fifth assumption is that black body radiation can also cause transitions to other Rydberg state at a rate γ_{bb} (Gallagher, 1994). At this point it is important to distinguish between γ_{bb} and γ_{bbi}. γ_{bb} is the rate at which black body radiation shuffles atoms amongst n states; γ_{bbi} is the rate at which Rydberg atoms are photoionized from black body photons. When atoms are photonionized by black body radiation, we see atom loss. The value of γ_{bbi} at n=50 was given above as 290/sec (Walker, private communication). The value of γ_{bb} can be calculated from the following equation in (Gallagher, 1994) in atomic units,

$$\gamma_{bb} = \frac{4\alpha^2 T}{3n^2} \tag{7.7}$$

where α is the fine structure constant and T is the temperature of the background taken to be 300K. The excited Rydberg states can spontaneously decay to the ground state at a rate similar to γ (see figure 7.13). This is a good assumption because according to (Gallagher, 1994), transitions to other Rydberg states caused by black body radiation are typically to close lying n states. The lifetime of a Rydberg state is given in (Gallagher, 1994) to be $\tau = 1/\gamma = 2.09\text{nsec} \times n^{2.85}$. While there is some n

dependence, in the limit that only mixing of nearby n states is allowed, the correction in γ is small. All nearby n states will be modeled as a single "storage" state, labeled s in figure 7.13. Lastly, we have included the effects of dipole blockade. We assume that dipole blockade reduces the rate at which atoms are excited from the the excited state to the Rydberg state. The stimulated emission from the Rydberg state to the excited state is unaltered by the interaction. We therefore assume the suppression appears in the following manner:

$$P_e \rightarrow P_e\left(1-\eta P_r\right) = P_e\left(1-\frac{n_r}{n_{max}}\right) = P_e\left(1-\frac{n_{MOT}}{n_{max}}P_r\right) \tag{7.8}$$

where n_{max} is the maximum allowed Rydberg density assuming no dipole blockade, n_r is the actual Rydberg density, and n_{MOT} is the MOT density. In our model η is the only free parameter. Once η is determined, we can determine n_{max} and then the effective range (radius) of influence of a single Rydberg atom.

We can write three rate equations which describe the populations in the s, e, and r states.

$$\frac{dP_r}{dt} = -R_r P_r + R_r P_e\left(1-\eta P_r\right) - \gamma P_r - \gamma_{bb} P_r \tag{7.9}$$

$$\frac{dP_s}{dt} = \gamma_{bb} P_r - \gamma P_s \tag{7.10}$$

$$\frac{dP_e}{dt} = R_1 P_g - R_1 P_e + R_r P_r - R_r P_e\left(1-\eta P_r\right) + \gamma P_r + \gamma P_s - \Gamma P_e \tag{7.11}$$

and finally in a closed system the sum of the populations in all three states needs to equal unity: $P_r + P_e + P_s + P_g = 1$. We solve this set of differential equations for the loss rate for $1/(P_s + P_r)$ because the measured Rydberg loss rate from the trap is $\gamma_1 = \gamma_{bbi}\left(P_s + P_r\right)$. The solution is long and not very enlightening so will not be given here.

It would be convenient to fit our data of γ_1 as a function of blue light power. To do this we need to express the above rates in terms of known values. We already

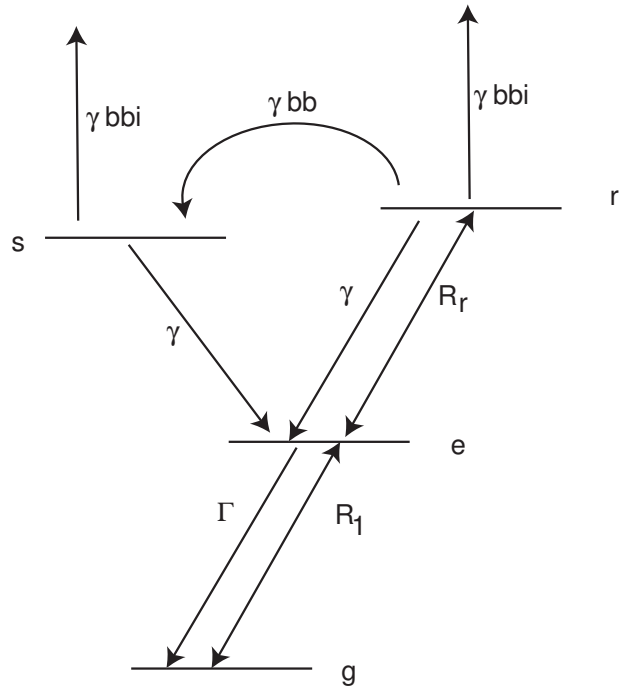

Fig. 7.13.— Trap loss model due to Rydberg excitation in a MOT.

have numerical solutions for γ_{bb} and γ_{bbi}. R_1 is 0.46Γ given that we have an excited state fraction of 0.23 which can be calculated knowing the trapping laser intensities and detunings. The excitation rate from the excited state to the Rydberg state, R_r is $R_r = \sigma I/\hbar\omega$. σ is the scattering cross section given by

$$\sigma = \frac{\sqrt{\pi} r_e f c}{\nu_L} \tag{7.12}$$

where r_e is the classical electron radius, f is the oscillator strength, $f = 0.9(2.7 \times 10{-}5$ [Walker, 2004], and ν_L is the laser linewidth defined by $I(\nu) = I_0 \times e^{-\delta\nu/\nu_L}/\sqrt{\pi}\nu_L$. I_0 can be calculated given the experimentally measured blue power and the measured beam waste of 1.0 mm. We take the laser linewidth to be 8 MHz.

Using these known values in the rate equations above, we can fit our measured loss rates as a function of blue power and extract the parameter η. Given the value of η and the MOT density, we can determine the maximum density of Rydberg atoms that

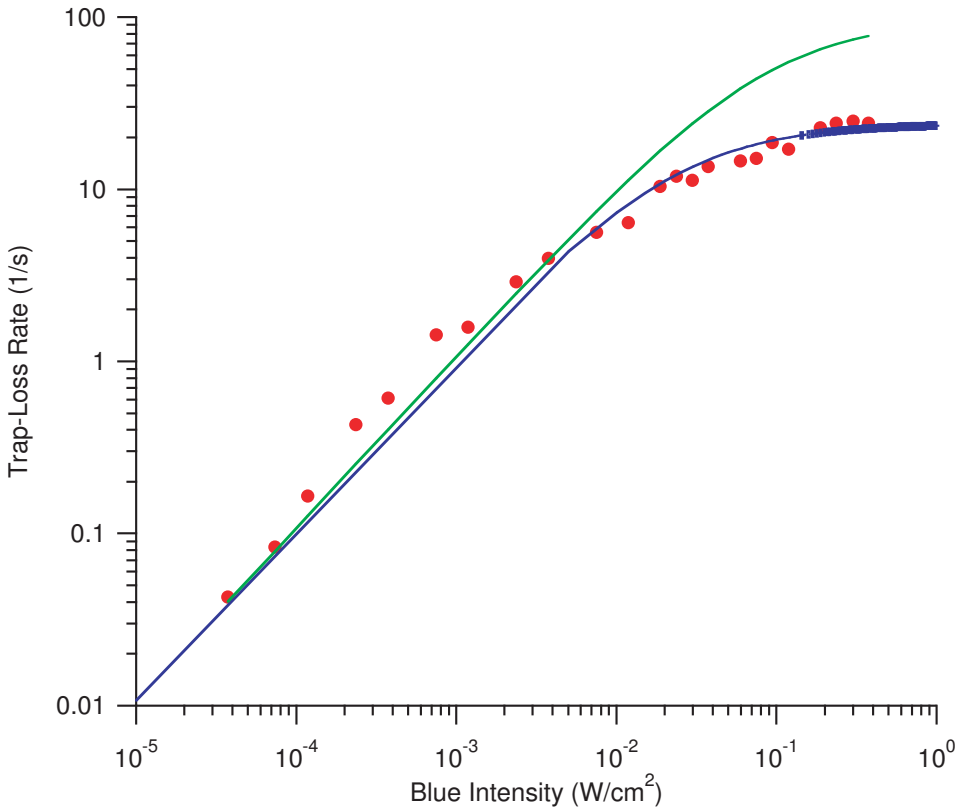

Fig. 7.14.— Model fit for γ_1 as a function of blue laser intensity for 46 d data.

are allowed to be excited. From this we can determine the effective range of influence (radius) of the excited Rydberg atom.

We have applied the fitting function to the graph shown in figure 7.6, the measured loss rate, γ_1, as a function of blue laser power for the one photon excitation to the 46 d state. The fit is shown in figure 7.14 and gives a value of $\eta = 23$. Also plotted is the case of $\eta = 0$, the case of no dipole suppression. At low blue laser powers, our data and the $\eta = 0$ curve are in good agreement. This is what we expect because at low blue laser powers there will be no effects from suppression because the density of excited Rydberg atoms is to small to cause suppression. It is encouraging that our data agrees with the $\eta = 0$ line of the model. At higher blue laser power, both curves begin

to saturate, but the data saturates at a lower blue power than the $\eta = 0$ curve. The $\eta = 0$ curve saturates because at high enough blue power we approach the classical limit that half of the MOT population is in the Rydberg state. The deviation of our data from the $\eta = 0$ line signifies that we are not transferring half the MOT population to the Rydberg state because a suppression mechanism is limiting the excitations into the Rydberg state.

7.5 Extracted Effective Rydberg Radius

Given the value of η from the fit function derived above, we can calculate the effective radius of our Rydberg atoms. The physical relevance of this radius is that atoms within this radius of influence are suppressed from being excited into the Rydberg state due to a Rydberg-Rydberg excitation (most likely van der Waals interaction). The parameter η is is given in equation (7.8),

$$\eta = 23 = \frac{n_{MOT}}{n_{MAX}}. \tag{7.13}$$

Using the fluorescence image of the MOT we have determined the density of the MOT to be $5 \times 10^{10}/\text{cm}^3$. From this we calculate n_{max} to be $2.2 \times 10^9/\text{cm}^3$. We then calculate the blockade volume of one Rydberg atom

$$\frac{1}{n_{max}} = 4/3\pi r_{eff}^3 \tag{7.14}$$

which gives $r_{eff} = 4.8\mu$m. The actual radius of the Rydberg atom is less than 0.1 μm. According to our model, the excited Rydberg atoms have a range of influence 50 times their actual size.

7.6 Discussion of Future Work

This work is being continued by my coworkers in the lab. Currently, they are measuring loss rates of n=30 Rydberg atoms in the MOT. At this principal quantum

number we expect 30 times less suppression, or in other words no suppression, since the van der Waals interaction scales as n^{11}. The plan is then to study a higher n state where the suppression should be substantial. The group is also experimenting with different methods of taking the above measurements, specifically, they are measuring γ_1 as a function of blue power and taking extra care to ensure that the density of the MOT is constant for all points. This is accomplished by altering the duty cycle of the blue laser to keep the number and size of the MOT constant.

After the conclusion of the studies of loss rates in the MOT, the group plans on producing Rydberg atoms in the HAT. Using the method of evaporation followed by recompression, the atomic densities discussed in this work will serve as an excellent foundation for the studies of lineshape broadening, pressure shifts, and the formation of trilobite molecules. Also, as we have discussed previously, the mesoscopic clouds attained through the evaporation and compression method will be excellent candidates for seeing a high fidelity complete blockade due to van der Waals interactions or with the addition of an electric field, dipole-dipole interaction.

Chapter 8

Conclusion

8.1 Conclusion

This section concludes the dissertation with a summary of the major results presented in this thesis and an outlook for the future of this experiment. The primary goal of this thesis was the development of high density, mesoscopic atomic samples for use in Rydberg experiments.

This dissertation began with a description of a novel far off resonant optical trap, the Holographic Atom Trap. The HAT is formed from the interference of 5 beams, forming clusters of small traps, microtraps, each with dimensions of 10 μm x 10 μm x 100 μm in size. The benefit of this trap geometry is that atoms in the HAT have high oscillation frequencies yet many atoms (36,000) can be stored in a single microtrap. The results is high initial atomic densities (10^{14} atoms/cm^3) and high phase space densities (1/200). The HAT has been characterized with two imaging systems: absorption imaging and spatial heterodyne imaging. Spatial Heterodyne is a novel interferometric nondestructive imaging system capable of imaging cold atoms with a signal to noise of 1/10 while only scattering 0.0004 photons per atom.

Forced evaporation has been preformed in the HAT to increase the phase space

density from an initial value of 1/200 to a final a phase space density of 1.1. The high initial densities attainable in the HAT are largely responsible for the success of forced evaporation. At initial densities of $2 \times 10^{14}/\text{cm}^3$, atom in the HAT rethermalize quickly allowing for rapid evaporation. We have developed a model to understand the dynamics of evaporation. By including the heating due to quantum diffraction collisions with background Rubidium atoms and secondary collisions occuring within the dense HAT microtraps, the model's predicted phase space density closely agrees with the measured phase space density.

A method for producing high density ($10^{15}/\text{cm}^3$) mesosopic samples (5 to 10 μm in radius) have been demonstrated in the HAT. Atoms in the HAT are evaporated to a phase space density of 1, then the cloud is recompressed by rapidly increasing the trap depth. The result is atomic clouds with densities of 2×10^{15} atoms/cm^3, the highest atomic densities achieved in incoherent matter, and cloud radii of 5.6 μm. The demonstration of these mesoscopic clouds represent significant progress towards the first observation of a complete dipole blockade because the radius of these clouds is less than the range of influence of an excited Rydberg atom. The estimated mean blockade shift over the entire cloud is approximately 30 MHz. This gives a probability that two Rdyberg atoms could be excited in a single microtrap to be less than 0.001. Discussion of using a static electric field to induce stronger interactions was discussed. In the presence of an electric field, mean dipole-dipole blockade shifts in excess of 400 MHz are possible.

Finally this dissertation described the production of Rydberg atoms in a Magneto Optical trap (MOT). Ryberg atoms were excited in two ways: single photon excitation from the $5P_{3/2}$ state or two photon excitation for the $5S_{1/2}$ state. This work is the first demonstration of two photon excitation of Rydberg atoms in the MOT and represents progress towards coherent manipulation of Rydberg atoms. This dissertation also dis-

cusses the first measurements of the absolute loss rates due to Rydberg atom excitation in the MOT. Our measurements are over a factor of 3 less than expected. We have developed a model to understand the loss rates and built into the model affects due to dipole suppression of Rydberg excitation. From the model we conclude that we see preliminary evidence of suppression of excitation due to interactions among Rydberg atoms. Efforts are underway to further validate this observations. Currently loss rates are being measured at different principle quantum numbers to study the dependence on the suppression of Rydberg atom excitation. The next step is to produce Rydberg atoms in the HAT with the goal for observing a complete dipole blockade.

Appendix A

Fitting Function for 3-Body Recombination

The change in number resulting from 3-body recombination is (for the time we will neglect losses due to background collisions)

$$\begin{aligned} \frac{dN}{dt} &= -K_3 \int n^3 \, d^3x & \text{(A.1)} \\ &= -K_3 n_0^3 \int \left(e^{-(x^2+y^2/\sigma_x^2)} e^{-z^2/\sigma_z^2} \right)^3 \, dxdydz & \text{(A.2)} \\ &= -K n_0^3 \sqrt{\frac{\pi\sigma_x^2}{3}\frac{\pi\sigma_y^2}{3}\frac{\pi\sigma_z^2}{3}}. & \text{(A.3)} \end{aligned}$$

Recall that $N = n_0\sqrt{\pi\sigma_x^2}\sqrt{\pi\sigma_y^2}\sqrt{\pi\sigma_z^2}$ so

$$\frac{dN}{dt} = \frac{-K n_0^2 N}{3^{3/2}} - \Gamma N \tag{A.4}$$

where now we include the losses due to background collisions, Γ.

Let $\beta = K/3^{3/2}$ and n = Nf making

$$\frac{dN}{dt} = -\beta f^2 N^3 - \Gamma N \tag{A.5}$$

.

To solve the differential equation we let U = 1/N and dN = -dU/U^2. We rewrite (A.5) in terms of U

$$\frac{-1}{U^2}\frac{dU}{dt} = \frac{-\beta f^2}{U^3} - \frac{\Gamma}{U} \tag{A.6}$$

$$U\frac{dU}{dt} = \beta f^2 + \Gamma U^2 \tag{A.7}$$

$$\frac{UdU}{\beta f^2 + \Gamma U^2} = dt. \tag{A.8}$$

The solution is $\beta f^2 + \Gamma u^2 = Ae^{2\Gamma t}$. To solve for A, we can use the boundary condition that at t = 0, u = u$_0$.

$$\beta f^2 + \Gamma u_0^2 = A \tag{A.9}$$

$$\beta f^2 + \Gamma u_0^2 = \beta f^2 e^{2\Gamma t} + \Gamma u_0^2 e^{2\Gamma t}. \tag{A.10}$$

Now, solve for u.

$$u = \sqrt{\left(\frac{\beta f^2}{\Gamma} + u_0^2\right)(e^{2\Gamma t} - 1) + u_0^2} \tag{A.11}$$

Recalling that u = 1/N

$$N(t) = \frac{N_0}{\sqrt{\left(\frac{\beta f^2 N_0^2}{\Gamma} + 1\right)(e^{2\Gamma t} - 1) + N_0}} \tag{A.12}$$

Equation (A.12) is the proper fitting function in the absence of heating mechanisms. In the presence of a heating mechanism there are two reasons the density decreases: three body loss and heating. The effects of heating need to be added. Recall that $f \sim n \sim 1/T^{3/2}$ so in equation (A.12) replace f^2 with

$$\left(\frac{f^2}{1 + \frac{1}{T_0}\frac{dT}{dt}\delta t}\right)^3 \tag{A.13}$$

where T_0 and is the temperature immediately after recompression and dT/dt is the measured increase in the temperature as a function of time.. After including the effects due to heating rates, the appropriate fit function is

$$N(t) = \frac{N_0}{\sqrt{\left(\frac{\beta f^2 N_0^2}{\Gamma\left(1+\frac{1}{T_0}\frac{dT}{dt}\delta t\right)^3}+1\right)(e^{2\Gamma t}-1)+N_0}}. \tag{A.14}$$

It is convenient to make the following substitutions in the fitting function (these will be used again in Appendix II), let

$$A = \beta f^2 \tag{A.15}$$

$$B = N_0 \tag{A.16}$$

$$C = \Gamma. \tag{A.17}$$

Note that the losses due to background collisions can also be determined with this fit. The three-body recombination rate can be calculated as

$$K_3 = 3^{3/2} A \left(\frac{N_0}{n_0}\right)^2 \tag{A.18}$$

where N_0 and n_0 are the number and density (repectively) in the center microtrap and t=0.

Appendix B

Calculation of the Probability of Double Excitation of Rydberg Atoms in the Compressed Microtrap

In this appendix, we will derive an equation to estimate the probability of producing two Rydberg atoms in the complicated geometry the HAT. We assume that it is impossible to produce three Rydberg atoms.

The Hamiltonian for the system is

$$H = \sum_i \frac{\epsilon_i}{2}|e_i\rangle\langle g| + \sum_{i,j} \frac{\epsilon_j}{2}|e_i e_j\rangle\langle e_j| + \sum_{i \ll j} \Omega_{ij}|e_i e_j\rangle\langle e_i e_j| \tag{B.1}$$

where the first term in the Hamiltonian is from the ground state, the second term is from the singely excited state, and the third term is from the doubly excited state. We let ϵ_i be the Rabi frequency for the ith atom and Ω_{ij} is the frequency shift caused by the Rydberg-Rydberg interaction. The wave function for the assembly is

$$|\psi\rangle = c_g|g\rangle + \sum_i c_i|r_i\rangle + \sum_{i<j} c_{ij}|r_i r_j\rangle. \tag{B.2}$$

The Schrodinger equations for the ith atom for the ground, singly excited, and doubly

excited state, respectively, are

$$i\dot{c}_g = \sum_i \frac{\epsilon_i}{2} c_i \tag{B.3}$$

$$i\dot{c}_i = \frac{\epsilon_i}{2} c_g + \sum_j \frac{\epsilon_j^*}{2}(c_{ij} + c_{ji}) \tag{B.4}$$

$$i\dot{c}_{ij} = \Omega_{ij} c_{ij} + \frac{\epsilon_j}{2} c_i + \frac{\epsilon_i}{2} c_j \tag{B.5}$$

First we assume perfect blockade, $c_{ij} = 0$ to solve the ground and singly excited equations. This leaves

$$i\dot{c}_g = \sum_i \frac{\epsilon_i}{2} c_i \tag{B.6}$$

$$i\dot{c}_i = \frac{\epsilon_i}{2} c_g. \tag{B.7}$$

Taking the second derivative of the ground state equation and substituting in $\dot{c}_i$,

$$i\ddot{c}_g = -ic_g \sum_i \frac{|\epsilon_i|^2}{4} \tag{B.8}$$

$$= -ic_g \frac{|\epsilon_N|^2}{4} \tag{B.9}$$

where

$$\sum_i \epsilon_i = \sqrt{N}\epsilon_0 \tag{B.10}$$

. We define ϵ_N as the effective Rabi frequency. The solution to (B.9 is the familiar equation for Rabi flopping

$$c_g(t) = \cos \epsilon_N t/2. \tag{B.11}$$

Using this solution we can solve the case where a single atom is excited to the Rydberg state

$$i\dot{c}_i = \frac{\epsilon_i}{2} c_g \tag{B.12}$$

$$ic_i = \frac{\epsilon_i}{2} \sin \frac{\epsilon t}{2} \left(\frac{2}{\epsilon}\right) \tag{B.13}$$

$$c_i = -i\frac{\epsilon_1}{\epsilon_N} \sin \frac{\epsilon_N t}{2}. \tag{B.14}$$

And finally we can solve for the case where two atoms have been excited to the Rydberg state, equation (B.5). Plugging in the solutions for c_i and c_j into (B.5)

$$i\frac{dc_{ij}}{dt} = \Omega_{ij}c_{ij} - i\frac{\epsilon_i\epsilon_j}{\epsilon_N}\sin\left(\frac{\epsilon_N t}{2}\right). \tag{B.15}$$

The solution to the differential equation is

$$c_{ij} = -\frac{\epsilon_i\epsilon_j}{2\epsilon_N}\left[\frac{2i\Omega_{ij}\sin\frac{\epsilon_N t}{2} - \epsilon_N\cos\frac{\epsilon_N t}{2}}{\Omega^2 - \epsilon_N^2/4}\right]. \tag{B.16}$$

Assuming that $\Omega_{ij} \gg \epsilon_N$ then we can approximate

$$c_{ij} \approx -i\frac{\epsilon_i\epsilon_j}{\epsilon_N\Omega_{ij}}\sin\frac{\epsilon_N t}{2}. \tag{B.17}$$

To make the Rydberg atoms, we will use a π-pulse, or ϵ_Nt=π

$$c_{ij} = -i\frac{\epsilon_j\epsilon_i}{\epsilon\Omega_{ij}}. \tag{B.18}$$

The probability of exciting two atoms is

$$P_2 = \sum_{i<j}|c_{ij}|^2 = \sum_{i<j}\left|\frac{\epsilon_i\epsilon_j}{\Omega_{ij}}\right|^2\frac{1}{|\epsilon_N|^2}. \tag{B.19}$$

We need now to determine ϵ_N. We assume that the Rydberg producing laser has a Gaussian distribution with a beam waist, w, $\epsilon_i = \epsilon_0 e^{-x^2/w^2}$ where ϵ_0 is the Rabi frequency at the center of the of the beam. Recall that $\epsilon_N^2 = \sum_i|\epsilon_i|^2$, we assume a Gaussian distribution of atoms in the microtrap with radius σ to describe N, $N(z) = Ne^{-z^2/\sigma^2}/\sqrt{\pi\sigma^2}$. We can describe the effective rabi frequency as the sum over both the Gaussian distribution of atoms and the Gaussian shaped laser beam,

$$\epsilon_N^2 = \int dx N\frac{e^{-x^2/\sigma^2}}{\sqrt{\pi}\sigma}\epsilon_0^2 e^{-2x^2/w^2} = \frac{N\epsilon_0^2}{\sqrt{1+2\sigma^2/w^2}}. \tag{B.20}$$

In the limit that $w \gg \sigma$ the "effective" number of atoms is $N_e = N/\sqrt{1+2\sigma^2/w^2}$, or in other words all the atoms in the microtrap are effected if the beam waist is larger

than the atomic cloud. On the other hand if $w \ll \sigma$ only the atoms in the beam waist are affected, $N_e \approx Nw/\sqrt{2}\sigma$.

Plugging (B.20 into (B.19) for the case of a π-pulse, $\epsilon_N \mathrm{T} = \pi$, the doubly excited probability is

$$P_2 = \frac{\epsilon^2 \left(1 + 2\sigma^2/w^2\right)}{N^2} \sum_{i<j} \frac{e^{-2(x_i^2+x_j^2)/w^2}}{\Omega_{ij}^2} \tag{B.21}$$

$$= \frac{\pi^2 \left(1 + 2\sigma^2/w^2\right)}{T^2 N^2} \sum_{i<j} \frac{e^{-2(x_i^2+x_j^2)/w^2}}{\Omega_{ij}^2}. \tag{B.22}$$

Of interest is that the probability is $\sim 1/\Omega^2$; atom pairs with the smallest dipole-dipole shifts are most heavily weighted in the sum. We therefore define a mean Rydberg-Rydberg blockade shift $\overline{\Omega}$ via

$$\frac{1}{\overline{\Omega}^2} = \frac{2(1 + 2\sigma^2/w^2)}{N^2} \sum_{i<j} \frac{e^{-2(x_i^2+x_j^2)/w^2}}{\Omega_{ij}^2}. \tag{B.23}$$

In terms of the blockade shift, the double excitation probability is

$$P_2 = \frac{\pi^2}{2T^2\overline{\Omega}^2} = \frac{\epsilon_N^2}{2\overline{\Omega}^2}. \tag{B.24}$$

For s-states the dipole-dipole shift is approximated by

$$\Omega(R) = \frac{\delta}{2} + \sqrt{\frac{4U_3(R)^2}{3} + \frac{\delta^2}{4}} \tag{B.25}$$

where δ is the energy for the $s + s \rightarrow np + (n-1)\,p$ defect and $U_3(R) = C_3/R^3 = e^2\langle ns||r||np\rangle\langle ns||r||(n-1)p\rangle/R^3$, C_3 van der Waals coefficient (Walker et al., 2004). Using (B.25) as the interaction term in equation (B.23) we can perform the sum over all positions between pairs of atoms to find $\overline{\Omega}^2$ and then P_2.

The results for the HAT with n=95 and T = 1 μs are summarized in Table B.1.

$\sigma(\mu m)$	w (μm)	$\Omega/2\pi$(MHz)	P_2
8.0	10	10.5	1.1×10^{-3}
8.0	20	2.09	0.029
8.0	∞	0.92	0.148
5.7	10	28	2×10^{-4}
5.7	20	8.8	1.6×10^{-3}
5.7	∞	5.1	4.9×10^{-3}

Table B.1: Summary of the dipole-diople shifts and probabilities of doubly excited states in the HAT for various σ and w values.

Appendix C

Feedback Circuits for Intensity Stabilizer

In this Appendix I will give the circuit diagram for two integral components of the YAG intensity stabilizer. The first circuit is the differential amplifier. We have found that the noise present on a single analog output is correlated with noise found on the other ananlog outputs. This noise can then be eliminated with the aid of a differential amplifier. The circuit shown here is updated from (Newell, 2003) in that a second filtering stage has been added. The new bandwith is 530 Hz.

The second circuit is the feedback circuit for the intensity stabilizer. In (Newell, 2003)] the feedback circuit had only integral gain. We have added an proportional gain to the circuit. With this circuit addition we made progress towards getting rid of the

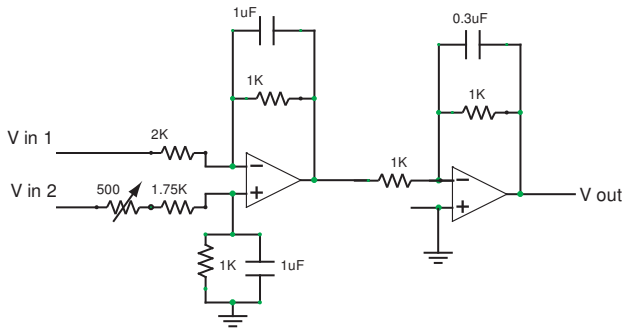

Fig. C.1.— Additional of filter stage to differential amplifier.

intentisy noise and increasing the bandwidth of the feedback loop. The current circuit has a bandwith of 22 kHz, almost an order of magnitude improvement to the former circuit.

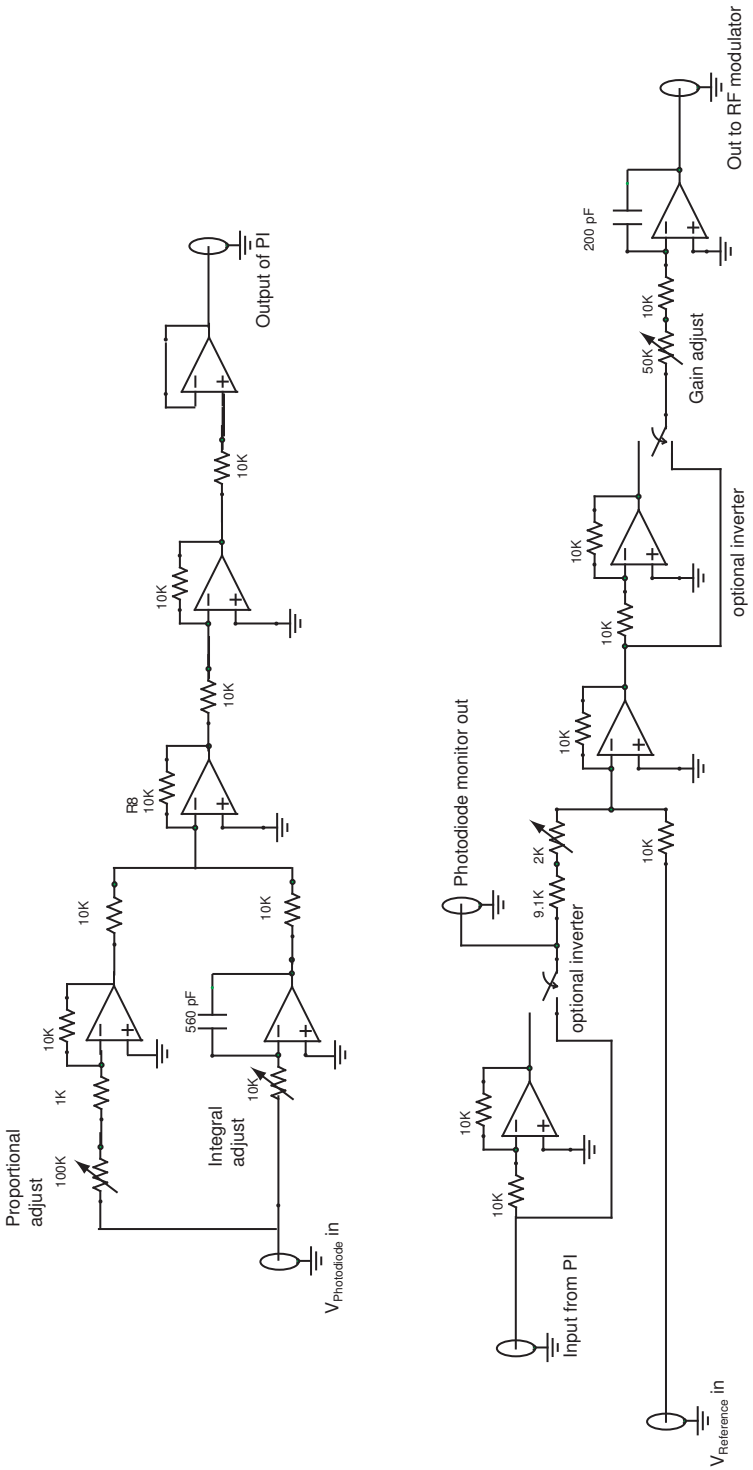

Fig. C.2.— Feedback circuit for intensity stabilizing the YAG.

Appendix D

Fit Function for Secondary collision

In this Appendix I will derive the fit function to describe heating due to secondary collisions. This fit function takes into account the temperature dependence in the $\langle nl \rangle$ term.

The temperature dependence in $\langle nl \rangle$ is

$$\langle nl \rangle \approx \frac{N\nu^3}{T} \approx \frac{1}{T}. \tag{D.1}$$

The change in energy due to heating can then be described as

$$\frac{dE}{dt} = \frac{\alpha}{T} \tag{D.2}$$

where α is a coefficient to be determined later. Relating the energy to the temperature for a 3-dimension harmonic oscillation, $E = 3NT$ and thus

$$\begin{aligned}
\frac{dT}{dt} &= \frac{1}{3}\frac{\alpha}{T} && \text{(D.3)}\\
3T\frac{dT}{dt} &= \alpha && \text{(D.4)}\\
\frac{3}{2}\frac{dT^2}{dt} &= \alpha && \text{(D.5)}\\
\frac{3}{2}\left(T^2 - T_0^2\right) &= \alpha t && \text{(D.6)}\\
T^2 - T_0^2 &= \frac{2}{3}\alpha t. && \text{(D.7)}
\end{aligned}$$

We will now determine the coefficient α. We can write the change in energy in terms of $\dot{Q}$, the heating rate, as

$$\frac{dE}{dt} = \dot{Q}\frac{nl(t)}{nl(t=0)}. \tag{D.8}$$

Substitution of the temperature dependence in the column density and the relationship between E and T,

$$3\frac{dT}{dt} = \dot{Q}\frac{T(0)}{T(t)} = \dot{Q}\frac{T_0}{T} \tag{D.9}$$

$$\frac{dT}{dt} = \frac{\dot{Q}}{3}\frac{dT}{dt} = \frac{1}{3}\frac{\alpha}{T} \tag{D.10}$$

therefore

$$\alpha = \dot{Q}T_0. \tag{D.11}$$

Substituting in for α, the fit function to describe the temperature as a function to time due to secondary collisions,

$$T(t) = \sqrt{T_0^2 + \frac{2}{3}\dot{Q}T_0 t}. \tag{D.12}$$

Appendix E

Torque Heating

In this appendix we will derive an equation for the heating rate caused by the rotation of the microtraps about their center. We call this torque heating. In our model for torque heating we consider a 2 dimensional harmonic oscillator.

$$m\ddot{r} = -k_x x'\hat{x} - k_z z'\hat{z} \tag{E.1}$$

The mictrotraps are allowed to rotate about their center by an angle θ. We apply the rotation matrix to transform to angular coordinates.

$$x' = x\cos\theta + z\sin\theta \tag{E.2}$$

$$z' = z\cos\theta - x\sin\theta \tag{E.3}$$

The force in the x direction is

$$m\ddot{x} = -k_x\left(x\cos\theta + z\sin\theta\right)\cos\theta - k_z\left(z\cos\theta - x\sin\theta\right)\left(-\sin\theta\right) \tag{E.4}$$

$$= -\left(k_x\cos^2\theta + k_z\sin^2\theta\right)x + \left(k_z - k_x\right)z\sin\theta\cos\theta. \tag{E.5}$$

Using a small angle approximation we can write the following equations of motion

$$m\ddot{x} \approx -k_x x + \theta\left(k_z - k_x\right)z \tag{E.6}$$

$$m\ddot{z} \approx -k_z z + \theta\left(k_z - k_x\right)x. \tag{E.7}$$

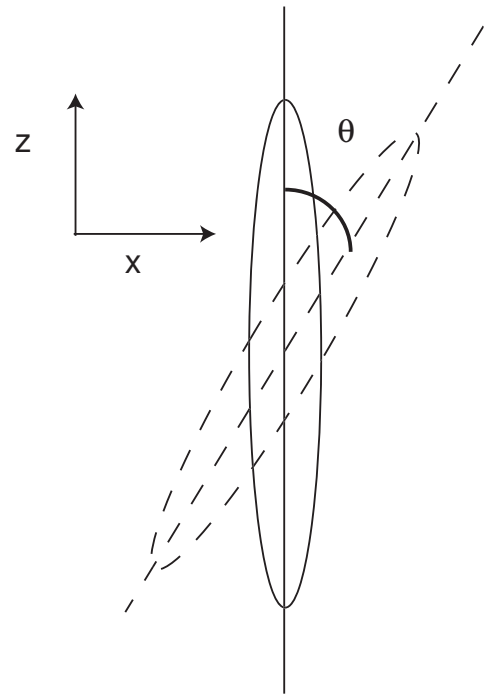

Fig. E.1.— Torque Heating

The change in energy is

$$\frac{dE}{dt} = \vec{F}\cdot\vec{v} = \theta\left(k_z - k_x\right)\begin{pmatrix} z \\ x \end{pmatrix}\cdot\begin{pmatrix} \dot{x} \\ \dot{z} \end{pmatrix} \tag{E.8}$$

$$= -\theta(\Delta k)\left(z\dot{x} + x\dot{z}\right). \tag{E.9}$$

Let $z = z_0 + z_1$ and $x = x_0 + x_1$ where subscripts 0 are the positions at $\theta = 0$. Substituting in these definitions, the nonzero terms are

$$\frac{dE}{dt} = -\theta\Delta k\left[z_0\dot{x_1} + z_1\dot{x_0} + x_0\dot{z_1} + x_1\dot{z_0}\right]. \tag{E.10}$$

We assume that the velocities and positions can be described as follows

$$x_1 = \int_0^t \frac{\sin\omega_x\left(t-t'\right)}{\omega_x}\left(\frac{-\theta\Delta k z_0}{m}\right)dt' \tag{E.11}$$

$$\dot{x_1} = \int_0^t \cos\omega_x\left(t-t'\right))\left(\frac{-\theta\Delta k z_0}{m}\right)dt'. \tag{E.12}$$

A similar set of equations can be written for the z terms. Let $x_0 = A_x \cos\omega_x t$ and $z_0 = A_z \cos\omega_z t$. We will now set out to solve for each of the terms in equation (E.10). The first term we will solve for is $\langle -\theta\Delta k z_0 \dot{x_1}\rangle$.

$$\langle -\theta\Delta k z_0 \dot{x_1}\rangle = \frac{1}{m}\int_0^T \frac{1}{T} A_z \cos\omega_z t(-\theta(t)\Delta k)\, dt \int_0^t \cos\omega_x\,(t-t')\,(-\theta(t-t')\Delta k A_z \cos\omega_z t')\; dt'. \tag{E.13}$$

Let $\tau = t - t'$, then the above equation can be written as

$$= \frac{(\Delta k A_z)^2}{m}\int_0^T \frac{1}{T}\cos(\omega_z t)\cos(w_z(t-\tau))\theta(t-\tau)\theta(t)\, d\tau \int_0^t \cos(\omega_x\tau)\, dt. \tag{E.14}$$

We can separate the average into two averages

$$\langle \cos(\omega_z t)\cos(w_z(t-\tau))\theta(t-\tau)\theta(t)\rangle = \langle \cos(\omega_z t)\cos(w_z(t-\tau))\rangle \langle \theta(t-\tau)\theta(t)\rangle . \tag{E.15}$$

The first term simplifies to

$$\langle \cos(\omega_z t)\cos(w_z(t-\tau))\rangle = \frac{1}{2}\cos\omega_z\tau \tag{E.16}$$

We introduce the first-order correlation function

$$\langle \theta(t)\theta(t-\tau)\rangle = \frac{1}{T}\int_0^T \theta(t)\theta(t-\tau)\, dt. \tag{E.17}$$

With these substitutions, this simplifies to

$$\langle -\theta\Delta k z_0 \dot{x_1}\rangle = \frac{(\Delta k A z)^2}{2m}\int_0^\infty \cos(\omega_x\tau)\cos(\omega_z\tau)\,\langle\theta(t)\theta(t-\tau)\rangle\; d\tau. \tag{E.18}$$

We will now solve for the $\langle -\theta\Delta k \dot{z_0} x_1\rangle$ term again using that $\tau = t - t'$ and the definition of the correlation function.

$$= \frac{(\Delta k A_z)^2}{m}\left(\frac{-\omega_z}{\omega_x}\right)\int_0^\infty \sin(\omega_x\tau)\sin(\omega_z t)\cos(\omega_z(t-\tau))\theta(t)\theta(t-\tau)\, d\tau. \tag{E.19}$$

This can be simplified to

$$\langle -\theta\Delta k \dot{z_0} x_1\rangle = \frac{(\Delta k A_z)^2}{2m}\left(\frac{-\omega_z}{\omega_x}\right)\int_0^\infty \sin(\omega_x\tau)\sin(\omega_z\tau)\,\langle\theta(t)\theta(t-\tau)\rangle\, , d\tau. \tag{E.20}$$

The other two terms follow in a similar manner. I will write their results.

$$\langle -\theta \Delta x_0 \dot{z_1} \rangle = \frac{(A_x \Delta k)^2}{2m} \int_0^\infty \cos(\omega_x \tau) \cos(\omega_z \tau) \langle \theta(t)\theta(t-\tau) \rangle \, d\tau \quad \text{(E.21)}$$

$$\langle -\theta \Delta k z_1 \dot{x_0} \rangle = \frac{(A_x \Delta k)^2}{m} \frac{\omega_x}{\omega_z} \int_0^\infty \sin(\omega_x \tau) \sin(\omega_z \tau) \theta(t) \langle \theta(t)\theta(t-\tau) \rangle \, d\tau \quad \text{(E.22)}$$

Substituting these results into equation (E.10) and collecting terms, we get

$$\begin{aligned} \left\langle \frac{dE}{dt} \right\rangle &= \frac{\Delta k^2}{2m} \left[\left(A_z^2 + A_x^2 \right) \int_0^\infty \cos(\omega_z \tau) \cos(\omega_x \tau) \langle \theta(t)\theta(t-\tau) \rangle \, d\tau \right] \\ &- \frac{\Delta k^2}{2m} \left[\left(\frac{\omega_z}{\omega_x} A_z^2 + \frac{\omega_x}{\omega_z} A_x^2 \right) \int_0^\infty \sin(\omega_z \tau) \sin(\omega_x \tau) \langle \theta(t)\theta(t-\tau) \rangle \, d\tau \right] \quad \text{(E.23)} \end{aligned}$$

From the equipartition of energy theorem we can write the total energy as

$$\langle E \rangle = \frac{1}{2} k_x \left\langle x^2 \right\rangle + \frac{1}{2} m \left\langle v_x^2 \right\rangle + \frac{1}{2} k_z \left\langle z^2 \right\rangle + \frac{1}{2} m \left\langle v_z^2 \right\rangle . \quad \text{(E.24)}$$

As we assumed before, let $x = A_x \cos(\omega_x t)$ and $z = A_z \cos(\omega_z t)$. Then $\langle x^2 \rangle = A_x^2/2$ and $\langle v_x^2 \rangle = A_x^2 \omega_x^2/2$ and likewise for the z terms. Substituting these in for the energy equation yields

$$\begin{aligned} \langle E \rangle &= \frac{1}{2} m \omega_x^2 \frac{A_x^2}{2} + \frac{1}{2} m \frac{A_x^2 \omega_x^2}{2} + \frac{1}{2} m \omega_z^2 \frac{A_z^2}{2} + \frac{1}{2} m \frac{A_z^2 \omega_z^2}{2} \\ &= \frac{1}{2} m \omega_x^2 A_x^2 + \frac{1}{2} \omega_z^2 A_z^2 \\ &= 2 k_b T \end{aligned}$$

where k_b is Boltzman's constant. We can now solve for the constants A_x and A_z.

$$A_x^2 = \frac{2 k_b T}{m \omega_x^2} = \frac{\langle E \rangle}{m \omega_x^2} \quad \text{(E.25)}$$

$$A_z^2 = \frac{2 k_b T}{m \omega_z^2} = \frac{\langle E \rangle}{m \omega_z^2} \quad \text{(E.26)}$$

To simplify the notation, let

$$I_c = \int_0^\infty \cos(\omega_z \tau) \cos(\omega_x \tau) \langle \theta(t)\theta(t-\tau) \rangle \, d\tau \quad \text{(E.27)}$$

and

$$I_s = \int_0^\infty \sin(\omega_z \tau) \sin(\omega_x \tau) \langle \theta(t)\theta(t-\tau) \rangle \, d\tau \tag{E.28}$$

so that we can write

$$\left\langle \frac{dE}{dt} \right\rangle = \frac{(\Delta k)^2}{2m} \left(\frac{\langle E \rangle}{m\omega_x^2} + \frac{\langle E \rangle}{m\omega_z^2} \right) I_c - \frac{(\Delta k)}{2m} \left(\frac{\langle E \rangle}{m\omega_z\omega_x} + \frac{\langle E \rangle}{m\omega_x\omega_z} \right) I_s. \tag{E.29}$$

Recall that $\Delta k = k_x - k_z$. In the HAT the atoms are much more tightly confined in the x direction so we can make the approximation that $\Delta k \approx k_x = m\omega_x^2$. Likewise, $\omega_z \ll \omega_x$ so the first term equation (E.29) is dominated by the $1/\omega_z^2$ term. Equation (E.29) can be simplified to

$$\left\langle \frac{dE}{dt} \right\rangle = \frac{m^2 w_x^4}{2m} \left[\frac{\langle E \rangle \, I_c}{m\omega_z^2} - \frac{2 \langle E \rangle \, I_s}{\omega_x\omega_z} \right]. \tag{E.30}$$

Again, the $1/\omega_z^2$ term will dominate leaving

$$\begin{aligned} \left\langle \frac{dE}{dt} \right\rangle &\approx \frac{\omega_x^4}{2\omega_z^2} \int_0^\infty \cos(\omega_z \tau) \cos(\omega_x \tau) \langle \theta(t)\theta(t-\tau) \rangle \, d\tau \, \langle E \rangle \\ &\approx \frac{\omega_x^4}{2\omega_z^2} \int_0^\infty \frac{1}{2} \left[\cos((\omega_z + \omega_x)\tau) + \cos((\omega_z - \omega_x)\tau) \right] \langle \theta(t)\theta(t-\tau) \rangle \, d\tau \, \langle E \rangle \\ &\approx \frac{\omega_x^4}{2\omega_z^2} \int_0^\infty \cos(\omega_x \tau) \langle \theta(t)\theta(t-\tau) \rangle \, d\tau \, \langle E \rangle \end{aligned} \tag{E.31}$$

where we have once again used the approximation that $\omega_x \gg \omega_z$. We will define the power spectrum (as done in [Gehm et al., 1998])

$$S_k(\omega) = \frac{2}{\pi} \int_0^\infty cos(\omega\tau) \langle \theta(t)\theta(t-\tau) \rangle \, d\tau. \tag{E.32}$$

Substituting this into equation (E.31) we get

$$\left\langle \frac{dE}{dt} \right\rangle = \frac{\omega_x^4}{2\omega_z^2} S_k(\omega_x) \langle E \rangle . \tag{E.33}$$

Equation (E.33) is the major result of this derivation. Analogous to heating from laser intensity noise, the heating due to rotation of the microtraps is proportional to the

energy. This is consistent with our physical picture of torque: the further the atoms are from the center of the trap, the more they will be effected by the fluctuations. Furthermore we can see that the heating is proportional to the frequency component at the sum of the x and z oscillation frequencies, but this can be approximated as just the x frequency. The time constant for the heating is defined by

$$\left\langle \frac{dE}{dt} \right\rangle = \Gamma \langle E \rangle \tag{E.34}$$

and thus

$$\Gamma = \left(\frac{\omega_x^4}{2\omega_z^2} \right) S_k(\omega_x). \tag{E.35}$$

Equation (E.35) is applied in chapter 7 to determine the heating rates in the HAT due to Torque heating.

Appendix F

Signal to Noise for Spatial Heterodyne Imaging

In this appendix I will derive the signal to noise ratio for spatial heterodyne imaging. I will also derive the figure of merit for a nondestructive imaging system which is really the signal to noise per absorbed photon.

The signal seen per pixel for spatial heterodyne is given by

$$N_r + N_p + 2\sqrt{N_r N_p}\cos\left(\chi - \phi(\mathbf{x})\right). \tag{F.1}$$

If we assume that $\chi = \frac{\pi}{2}$ and that $\phi(x)$ is small, then

$$N_r + N_p + 2\sqrt{N_r N_p}\sin\phi(\mathbf{x}) \approx N_r + N_p + 2\sqrt{N_r N_p}\phi \tag{F.2}$$

After substraction of the probe and reference beams the number of photons striking the camera per pixel (signal) is:

$$N_s = 2\eta\sqrt{N_r + N_p}\phi \tag{F.3}$$

where η is the quantum efficiency of the CCD camera. The noise contribution is given by

$$\sqrt{(N_r + N_p)\eta + b^2} \tag{F.4}$$

where b is the technical noise of the camera. S/N ratio is given by

$$\frac{S}{N} = \frac{2\eta\sqrt{N_p N_r}\phi}{\sqrt{(N_r + N_p)\eta + b^2}}. \tag{F.5}$$

Assuming that $N_r \gg N_p$ and $N_r \gg b^2/\eta$ the S/N is

$$\frac{S}{N} = \frac{2\phi\sqrt{N_p N_r \eta}}{N_r} = 2\phi\sqrt{N_p \eta}. \tag{F.6}$$

Herein lies the true power of spatial heterodyne: N_r can be made arbitrarily large so as to make the technical noises negligible. The result gives that in order to maintain a certain signal-to-noise, there is a minimum amount of probe photons that must be scattered. Nonetheless, too be completely nondestructive we want to minimize the number of probe photons scattered. The real figure of merit for spatial heterodyne is the signal-to-noise per absorbed probe photon which is given by:

$$\frac{S/N}{A} = \frac{2\phi\sqrt{\eta N_p}}{\alpha N_p}. \tag{F.7}$$

Using the relation that $\phi/\alpha \approx \Delta/\Gamma$ gives

$$\frac{S/N}{A} \approx 2\frac{\Delta}{\Gamma}\sqrt{\frac{\eta}{N_p}}. \tag{F.8}$$

By using a large detuning and a low fluence, the greatest signal to noise ratio per absorbed photon can be achieved.

References

J. A. Sauer, K. M. Fortier, M. S. Chang, C. D. Hamley, and M. S. Chapman, "Cavity QED with opitcally transported atoms", Phys. Rev. A **69**, 051804 (2004).

J. McKeever, J. R. Buck, A. D. Boozer, and H. J. Kimble, "Determination of the Number of Atoms Trapped in an Optical Cavity", Phys. Rev. Lett. **93**, 143601 (2004).

W. R. Anderson, J. R. Veale, and T. F. Gallagher, "Resonant Dipole-Dipole Energy Transfer in a Nearby Frozen Rydberg Gas", Phys. Rev. Lett **80**, 249 (1998).

J. L. Robers, C. D. Fertig, M. J. Lim, S. L. Rolston, "Electron Temperature of Ultracold Plasmas", Phys. Rev. Lett. **92**, 253003 (2004).

T. F. Gallagher, P. Pillet, M. P. Robinson, B. Laburthe-Tolra, M. Noel, "Back and forth between Rydberg atoms and ultracold plasmas", J. Opt. Sci. Amer. B **20**, 1091 (2003).

A Walz-Flannigan, J. R. Guest, J.-H. Choi, and G. Raithel, "Cold-Rydberg-gas dynamics", Phys. Rev. A **69**, 063405 (2004).

C. E. Simien, Y. C. Chen, P. Gupta, S. Laha, Y. N. Martinez, P. G. Mickelson, S. B. Nagel, and T. C. Kilian, "Using Absorption Imaging to Study Ion Dynamics in an Ultracold Neutral Plasma", Phys. Rev. Lett. **92**, 143001 (2004).

C. H. Greene, A. S. Dickinson, and H. R. Sadeghpour, "Creation of Polar and Nonpolar Ultra-Long-Range Rydberg Molecules", Phys. Rev. Lett **85**, 2458 (2000).

C. Boisseau, I. Simbotin, and R. Cote, "Macrodimers: Ultralong Range Rydberg Molecules", Phys. Rev. Lett. **88**, 133044 (2002).

S. M. Farooqi, D. Tong, S. Krishnan, J. Stanojevic, Y. P. Zhang, J. R. Enshwer, A. S. Estrin, C. Boisseau. R. Cote, E. E. Eyler, and P. L. Gould, "Long-Range Molecular Resonance in Cold Rydberg Gas", Phys. Rev. Lett. **91**, 183002 (2003).

M. D. Lukin, M. Fleischhauer, R. Cote, L. M. Duan, D. Jaksch, J. I. Cirac, and P. Zoller, "Dipole Blockade and Quantum Information Processing in Mesoscopic Atomic Ensembles", Phys. Rev. Lett. **87**, 037901 (2001).

K. Singer, M. Reetz-Lamour, T. Amthor, L. G. Marcassa, and M. Weidemuller, "Suppression of Excitation and Spectral Broadening Induced by Interaction in a Cold Gas of Rydberg Atoms," Phys. Rev. Lett. **93**, 163001 (2004).

D. Tong, S. M. Farooqui, J. Stanojevic, S. Krishnan, Y. P. Zhang, R. Cote, E. E. Eyler, and P. L. Gould, "Local Blockade of Rydberg Excitation in an Ultracold Gas", Phys. Rev. Lett. **93**, 016406 (2004).

R. Newell, J. Sebby, and T. G. Walker, "Dense atom clouds in a Holographic Atom Trap", Opt. Lett. Vol. 28, Iss. 14, P. 1266, 2003

J. Sebby-Strabley, R. T. R. Newell, J. O. Day, E. Breeke, and T. G. Walker, "High Density Mesoscopic Atom Clouds in a Holographic Atom Trap", physics/0408028 (2004).

S. Kadlecek, J. Sebby, R. Newell, and T. G. Walker, "Nondestructive spatial heterodyne imaging of cold atoms", Opt. Lett. Vol. 26, P. 137, 2001

R. T. R. Newell, "Cold and Dense Clouds of Atoms in a Holographic Atom Trap", Doctoral Thesis, University of Wisconsin-Madison, 2003.

E. A. Burt, R. W. Ghrist, C. J. Myatt, M. J. Holland, E. A. Cornell, and C. E. Wieman, "Coherence, Correlations, and Collisions: What one Learns about Bose-Einstein Condensates from Their Decay", Phys. Rev. Lett. **79**, 337 (1997).

M. D. Barrett, J. A. Sauer, and M. S. Chapman, "All-optical formation of an atomic Bose-Einstein condensate", Phys. Rev. Lett. Vol 70, No. 1, p. 010404, July 2001

K. M. O'Hara, S. R. Granade, M. E. Gehm, T. A. Savard, S. Bali, C. Freed, and J. E. Thomas, "Dynamics of noise-induced heating in atom traps", Phys. Rev. A **58**, 3914 (1998).

H. Metcalf and P. van der Straten, *Laser Cooling ad Trapping*, Springer-Verlag, 1999.

C. Gerz et al. "The temperature of optical molasses for two different atomic angular momenta", Europhysics Letters **21** Vol. 6, 661 (1993).

W. Ketterle, K. B. Davis, M. A. Joffee, A. Martin, and D. E. Pritchard, "High densities of cold atoms in a *dark* spontaneous-force optical trap", Phys. Rev. Lett. **70**, 2253 (1993).

J. D. Miller, R. A. Kline, and D. J. Heinzen, "Far-off-resonance optical trapping of atoms" Phys. Rev. A **6**, 4567 (1993)

M. H. Anderson, W. Petrich, J. R. Ensher, and E. A. Cornell, "Reduction of light assisted collisional loss rate from a low-pressure vapor-cell trap", Phys. Rev. A **50**, R3597 (1994).

M. A. Kadar-Kallen and K. D. Bonin, "Light force technique for measuing polarizabilities", Phys. Rev. Lett. **86**, 2015 (1992).

D. Boiron, A. Michaud. J. M. Fournier, L. Simard, M. Sprenger, G. Gyndberg, and C. Salomon, "Cold and dense cesium clouds in far-detuned diple traps," Phys. Rev. A **57**, R4106 (1998).

H. F. Talbot, Philos. Mag **9**, 401 (1836).

J. L. Roberts, N. R. Claussen, J. P. Burke, Jr. , C. H. Greene, E. A. Cornell, and C. E. Weiman, "Resonant Magnetic Field Control of Elastic Scattering of Cold ^{85}Rb", Phys. Rev. Lett **81**, 5109 (1998).

R. S. Williamson, "Magneto-optical trapping of patassium isotopes", Doctoral Thesis, University of Wisconsin-Madison, 1997.

T. Walker, D. Sesko, C. Weman, "Collective behavior of optically trapped neutral atoms", Phys. Rev. Lett. **64**, 408 (1990).

D. W. Sesko, T. G. Walker, and C. E. Wieman, "Behavior of Optically Trapped Neutral Atoms in a Spontaneous Force Trap", J. Opt. Soc. Am. B **8**, 946 (1991).

D. Sesko, T. Walker, C. Monroe, A. Gallagher, and C. Wieman, "Collisional losses for a light-force atom trap", Phys. Rev. Lett. **63**, 961 (1989).

M. R. Andrews, D. M. Kurn, H. J. Miesner, D. S. Durfee, C. G. Townsend, S. Inouye, and W. Ketterle, "Propagation of sound in a Bose-Einstein Condensate", Phys. Rev. Lett. **79**, 553 (1997)

M. R. Andrews, M.-O. Mewes, N. J. van Druten, D. S. Durfee, D. M. Kurn, and W. Ketterle, Science **273**, 84 (1996).

L. D. Turner, K. P. Weber, D. Paganin, and R. E. Scholten, "Off-resonant defocus-contrast imaging of cold aotms", Opt. Lett. **29**, 232 (2004).

W. Ketterle, D. S. Durfee, and D. M. Stamper-Kurn in *Bose-Einstein Condensation in Atomic Gases*, M. Inguscio, S. Stringari, and C. E. Wieman, eds., Vol. 140 of Proceeding of the Interntional School of Physics Enrico Fermi (IOS Press, Amsterdam, 1999), pp. 67 -176.

K. M. O'Hara, S. R. Granade, M. E. Gehm, and J. E. Thomas, "Loading Dynamics of CO_2 laser traps", Phys. Rev. A **63**, 043403 (2001).

S. J. M. Kuppens, K. L. Corwin, K. W. Miller, T. E. Chupp, and C. E. Weiman, "Loading an optical dipole trap," Phys. Rev A **62**, 013406 (2000).

W. Petrich, M. H. Anderson, J. R. Enscher, E. A. Cornell, "Behavior of atoms in a compressed magneto-optical trap", J. Opt. Soc. Am. B **11**, 1332 (1994).

M. H. Anderson, J. Ensher, M. Matthews, C. Wieman, and E. Cornell, "Observation of Bose-Einstein Condensation in a dilute atomic vapor", Science, Vol. **269**, 198 (1995).

K. Davis, M. Mewew, M. Andrews, N. van Druten, D. Durfee, D. Kurn, and W. Ketterle, "Bose-Einstein Condensation in a gas of sodium atoms", Phys. Rev. Lett. **75**, 3969 (1995).

T. Weber, J. Herbig, M. Mark, H.-C. Nagerl, R. Grim, "Bose-Einstein Condensation of Cesium," Science **299**, 232 (2003).

J. Kinast, S. L. Hemmer, M. E. Gehm, A. Turlapov, and J. E. Thomas, "Evidence for Superfluidity in a Resonantly Interacting Fermi Gas", Phys. Rev. Lett **92**, 150402 (2004).

K. B. Davis, M. O. Mewes, and W. Ketterle, "An analytical model for evaporative cooling of atoms", App. Phys. B., Vol. **60**, 155 (1995).

K. M. O'Hara, M. E. Gehm, S. R. Grande, and J. E. Thomas, "Scaling laws for evaporative cooling and time-dependent optical traps", Phys. Rev. A. **64**, 051403 (2001).

D. W. Snokes, J. P. Wolfe, "Population dynamics of a Bose gas near saturation", Phys. Rev. B **39**, 4030 (1989).

B. L. Tolra, K. M. O'Hara, J. H. Huckans, W. D. Phillips, S. L. Rolston, and J. V. Porto, "Observation of Reduced Three-Body Recombination in a Correlated 1D Degenerate Bose Gas", Phys. Rev. Lett. **92**, 190401 (2004).

S. Friebel, R. Scheunemann, J. Walz, T. W. Hansch, and T. W. Weitz, "Laser cooling in a $C0_2$ laser opitcal lattice", Appl. Phys. B, Vol. **67**, 699, (1998).

T. G. Walker and M. Saffman, "Zeros of Rydberg-Ryberg Föster Interactions", physics/0407048 (2004).

M. Saffman and T. G. Walker, "Engineering single atom and single photon sources from entangled atomic ensembles", Phys. Rev. A **66**, 065403 (2002).

T. A. Savard, K. M. O'Hara, and J. E. Thomas, "Laser noise induced heating in far-off resonant atom traps", Phys. Rev. A **58**, R1095 (1997).

M. E. Gehm, K. M. O'Hara, T. A. Savard, and J. E. Thomas, "Dynamics of noise-induced heating in atom traps", Phys. Rev. A **58**, 3914 (1998).

S. Bali, K. M. O'Hara, M. E. Gehm, S. R. Grande, and J. E. Thomas, "Quantum-diffraction background gas collisions in atom-trap heating and loss", Phys. Rev. A **60**, 29 (1999).

H. C. W. Beijerinck, "Heating rates in collisionally opaque alkali-matal atom traps: Role of secondary collisions", Phys. Rev. A **62**, 63614 (2000).

D. Jaksch, J. I. Cirac, P. Zoller, S. L. Rolston, R. Cote, M. D. Lukin, "Fast Quantum Gates for Neutral Atoms", Phys. Rev. Lett **85**, 2208 (2000).

.

B. K. Teo, D. Feldbaum, T. Cubel, J. R. Guest, P. R. Berman, and G. Raithel, "Autler-Townes spectroscopy of the $5S_{1/2} - 5P_{3/2} - 44D$ cascade of Cold ^{85}Rb atoms", Phys. Rev. A **68**, 053407 (2003).

T. F. Gallagher, *Rydberg Atoms*, (Cambridge University Press, Cambridge, 1994.)